THE PROPAGATION AND RUNUP OF SOLITARY WAVES ON STEEP SLOPES*

S. Grilli I.A. Svendsen

January 11, 1990

Ocean Engineering Program, Department of Civil Engineering
University of Delaware, Newark-DE 19716, USA

Abstract

The runup and reflection of a solitary wave are examined using a Boundary Element Method for the velocity potential using the full nonlinear boundary conditions. The computations are carried out in the physical space, and the waves are not assumed space periodic. Higher order elements are used in the computations to describe both geometry and flow variables and the time integration is explicit and of second order in Δt.

Exact solitary waves are generated by Tanaka's (1986) method and introduced on the free surface of the BEM model. Approximate solitary wave generation by a piston wavemaker moved according to Goring's (1978) *first-order* solution is numerically simulated for making a comparison with laboratory experiments. The transformations of the approximate waves are studied as they propagate down a numerical wave tank.

Reflection on a vertical wall of the waves generated both ways is studied and differences in runup and pressure force analyzed. Runup, rundown, reflected wave, celerity, phase shift, energy partition and pressure force of the *exact* solitary waves are compared with the Fourier Method of Fenton & Rienecker (1982) and with the analytical results of Su & Mirie (1980) and Byatt-Smith (1988). In particular, the predictions of the latter study for the change in amplitude and for the oscillatory tail of the reflected waves agree quite well with our results.

Comparisons are made with the detailed measurements of Losada, *et al.* (1986) for runup and reflection from steep slopes (45°, 70°) of solitary waves generated by a piston wavemaker. Free surface elevations are found to agree quite well with our computations and even small scale disturbances in the experiments from the nonlinear processes (like the oscillatory tail after reflection) are reproduced surprisingly accurately.

Finally is given a detailed analysis of the velocity and pressure variation in the wave motion during the runup and reflection process on a 45° slope, and the applicability of the nonlinear shallow water equations is discussed on the basis of the computational results. In particular, substantial deviation from uniformity over the depth of the horizontal velocity profile are observed (up to 30%) and, accordingly, non-hydrostatic pressures on the slope. Maximum runups, however, compare reasonably well with the results by Synolakis (1987), who uses the approximate equations.

*Paper submitted to *Journal of Fluid Mechanics.*

1 Introduction

Over the last decade numerical solution of the exact nonlinear equations for the inviscid water waves using a Boundary Integral Equation (BIE) description has become an extremely successful method for analyzing particularly the overturning of breaking waves. Practically all previous contributions, however, utilize space periodicity of the waves and most of them also are based on a conformal mapping of physical space onto a plane in which the equivalent of the free surface is the only part left of the boundary. The Boundary Integral Equation is then solved in the transformed plane. A few contributions use some other complex variable-dependent techniques.

There are many advantages of this method which has been explored extensively by many authors. Particularly noteworthy for significant steps to the development are contributions by Longuet-Higgins & Cokelet (1976), Vinje & Brevig (1981) and Dold & Peregrine (1986).

The procedure, however, also has some important limitations which are associated with the use of complex variables and with the assumption of waves that are periodic in space. The present paper aims at developing an equally efficient and accurate method without utilizing those two crucial assumptions and at demonstrating its application to a problem for which the above-mentioned version is not well suited, namely the generation (by a wavemaker motion or directly on the free surface) of a fully nonlinear solitary wave, and its subsequent propagation, runup on and reflection from a wall or a steep smooth slope.

For this purpose, we consider the wave motion in the physical space and describe the motion using a free space Green's function to transform the Laplace differential equation into an integral equation that involves only values of the velocity potential and its normal derivative along the physical boundary. An important difference from the above mentioned space periodic solutions is here that when imposing the boundary conditions in the physical space, the problem of surface piercing, fixed or moving, bodies has to be properly handled.

There are few examples in the literature of utilization of this direct approach for nonlinear water waves. Isaacson (1982) applied the method in a three-dimensional computation of wave forces on structures. The crudest possible numerical technique he used and his lack of a proper radiation condition put severe constraints on the accuracy of his computations and the length of time over which he could pursue them. Dommermuth & Yue (1987) used the BIE method in the 2D problem of axisymmetrical heaving of a floating body combined with Longuet-Higgins & Cokelet's time integration technique. Romate (1989) developed a 3D panel method (piecewise constant approximations of the potential) based on the BIE method and applied it to the generation of weakly nonlinear waves by a wavemaker. The boundary integral method has also been applied to the runup of a solitary wave on a slope by Kim, Liu & Liggett (1983) and on a vertical wall by Nakayama (1983), both using the equivalent of linear elements and an iterative implicit time integration procedure. The method of Kim, *et al.* was also used by Sugimoto, *et al.* (1987) for the runup on slopes of solitary waves of small amplitude to verify an approximate Boussinesq approach. Finally, Greenhow & Lin (1985) used the method of Vinje & Brevig (1981), based on the Cauchy integral theorem, in the physical space for solving the problems of the start of a wave paddle, and of a wedge entry in still water, and Klopman (1988) used the same method for computing the overturning of waves over steep slopes.

The procedure described in this paper is a Boundary Element Method (BEM) which is

developed for higher order elements. The time integration corresponds to the explicit scheme developed by Dold & Peregrine (1986). Grilli, *et al.* (1988) modified this method to using the shape functions of the BEM and applied it to the physical space. Application of the Dold & Peregrine method to the physical space has also been mentioned by Nakayama (1988). A version correct to second order in Δt has been developed for the computations presented here.

The problem analyzed is the development of a solitary wave as it runs up and is reflected from a vertical wall or from a steep slope, and the computations are compared with other numerical or analytical solutions (vertical wall) and with recent experimental results (steep slope).

Runup and reflection from slopes of non-breaking solitary waves have been studied quite extensively in the literature. As mentioned above, this was the topic of the boundary integral computations by Kim, *et al.* (1983) who, however, only used a few computation points (up to 38 along the entire boundary) and gave very few details about the results. In fact, the solitary wave runup problem using the exact Navier Stokes equations was studied numerically already by Camfield & Street (1969) by means of a marker and cell method.

More commonly, however, the runup of solitary waves has been analyzed using long wave theory or Boussinesq theory. The special case of reflection from a vertical wall is equivalent to the problem of collision between two opposing solitary waves of the same height and several studies have been published utilizing that analogy. A first order solution can be obtained by the Inverse Scattering Technique developed in the 1960's and 70's (Gardner,et al., 1967), a third order analysis was developed by Su & Gardner (1969) and Su & Mirie (1980) and solved numerically by Mirie & Su (1982), and a 5th order analysis was developed by Byatt-Smith (1988). Fenton & Rienecker (1982) used a Fourier Method to obtain very high order results for the same problem (somewhat limited, however, in the representation of high frequency oscillations by the periodicity condition they had to impose in their method).

The runup on a slope was analyzed numerically on the basis of the Boussinesq equations by Pedersen & Gjevik (1983), and Synolakis (1987) generalized the approach of Carrier (1966), based on the Nonlinear Shallow Water equation (NSW), to apply to the situation also considered in this paper with a constant depth region in front of the slope.

We will show that the method we use here is capable of quite accurately describing fully nonlinear free surface flows in great detail and over periods of time at least long enough to allow us to study wave runup problems without having to introduce any smoothing or modification of the solution. The method will be used for analyzing the higher order effects in terms of the ratio wave height over depth, which occur during reflection of high solitary waves from a vertical wall and from steep slopes.

The theoretical background is briefly outlined in Section 2 and 3. Since the computations are made in physical space, but only covering a limited region of a long wave tank, the waves to be studied have to be generated at one end of or inside the fluid domain. Two methods of generation are used. They are described in Section 4. We will analyze both *exact* solitary waves, as calculated by Tanaka's (1986) method, and *first-order* solitary waves, as generated by a piston wavemaker motion (Goring (1978)). The latter method will be used for making a comparison with the experimental results by Losada, *et al.* (1986) (hereinafter designated LVN). In Section 5, the results obtained with both generation methods are compared with those of Su & Mirie (1980) (S&M), Byatt-Smith (1988) (B-S) and Fenton & Rienecker (1982)

(F&R), for the special case of a vertical wall. Finally, Section 6 discusses the runup and reflection from steep slopes. The computations are compared with measurements by Losada, *et al.* (1986) (Section 6.2). Computational results are also given for detailed evolution of the internal velocity field (Section 6.3) and for the pressure along the slope (Section 6.4). Both are shown to deviate substantially from the basic assumption underlying the NSW solution of, e.g., Synolakis (1987). Some of these results, using an earlier, less accurate version of the method, were reported by Grilli & Svendsen (1989a) and Svendsen & Grilli (1989).

2 Mathematical formulation

2.1 *Governing equations and boundary conditions*

We consider an inviscid irrotational 2-D flow described by a velocity potential $\phi(\mathbf{x},t)$, and the velocity field is given by $\mathbf{u} = \nabla\phi = (u,w)$. Thus, the continuity equation in the fluid domain $\Omega(t)$ with the boundary $\Gamma(t)$ becomes a Laplace equation for ϕ (Figure 1),

$$\nabla^2\phi = 0 \qquad \text{in } \Omega(t) \tag{1}$$

Using the free space Green's function $G(\mathbf{x},\mathbf{x}_l) = -\frac{1}{2\pi}\log|\,\mathbf{x}-\mathbf{x}_l\,|$, this is solved as the boundary integral equation,

$$\alpha(\mathbf{x}_l)\phi(\mathbf{x}_l) = \int_\Gamma [\frac{\partial\phi}{\partial n}(\mathbf{x})G(\mathbf{x},\mathbf{x}_l) - \phi(\mathbf{x})\frac{\partial G(\mathbf{x},\mathbf{x}_l)}{\partial n}]\,d\Gamma \tag{2}$$

where $\mathbf{x} = (x,z)$ and $\mathbf{x}_l = (x_l,z_l)$ are position vectors for points on the boundary, and $\alpha(\mathbf{x}_l)$ is a geometric coefficient.

On the free surface $\Gamma_f(t)$, ϕ satisfies the kinematic boundary condition,

$$\frac{D\mathbf{r}}{Dt} = (\frac{\partial}{\partial t} + \mathbf{u}\cdot\nabla)\mathbf{r} = \mathbf{u} \qquad \text{on } \Gamma_f(t) \tag{3}$$

with $\mathbf{r}$, the position vector of a free surface fluid particle. Thus

$$\frac{D\mathbf{r}}{Dt} = \nabla\phi \qquad \text{on } \Gamma_f(t) \tag{4}$$

and the dynamic free surface boundary condition,

$$\frac{D\phi}{Dt} = -gz + \frac{1}{2}|\,\nabla\phi\,|^2 - \frac{p_a - p_o}{\rho} \qquad \text{on } \Gamma_f(t) \tag{5}$$

where g is the acceleration due to gravity, z is the vertical coordinate (positive upwards and $z = 0$ at the undisturbed free surface), p_a the pressure at the surface, p_o a reference pressure (e.g. at infinity) and ρ the fluid density.

The solitary waves are generated in two ways. In the first, the potential $\phi(x,t_o)$ and the elevation $\eta(x,t_o)$ of an *exact* solitary wave are prescribed on the free surface $\Gamma_f(t_o)$ at an initial time t_o. In this case, the normal velocity is zero over the leftward boundary Γ_{r1}, so that we have (see Figure 1),

$$\phi = \phi(x,t_o)\ ,\ z = \eta(x,t_o) \qquad \text{on } \Gamma_f(t_o)$$

$$\nabla\phi \cdot \mathbf{n} \equiv \frac{\partial \phi}{\partial n} = 0 \qquad \text{on } \Gamma_{r1} \tag{6}$$

where $\mathbf{n}$ is the unit outward normal vector. In the second method, *first-order* solitary waves are generated by simulating a piston-type wavemaker motion on the boundary $\Gamma_{r1}(t)$. In this second case, the normal velocity is specified over the surface of the paddle by,

$$\nabla\phi \cdot \mathbf{n} \equiv \frac{\partial \phi}{\partial n} = u_p(x_p(t), t)\, n_x \qquad \text{on } \Gamma_{r1}(t) \tag{7}$$

where n_x is the horizontal component of $\mathbf{n}$ and (x_p, u_p) are prescribed wavemaker motion and velocity respectively.

Along the stationary bottom Γ_b and the slope Γ_{r2} we have in both cases,

$$\nabla\phi \cdot \mathbf{n} \equiv \frac{\partial \phi}{\partial n} = 0 \qquad \text{on } \Gamma_b \text{ and } \Gamma_{r2} \tag{8}$$

2.2 *The time stepping method*

The time stepping consists of integrating the two nonlinear free surface conditions (4) and (5) to establish the new position of the free surface and the relevant boundary conditions of Laplace's problem at the next time step. Following the approach used by Dold & Peregrine (1986), the updating of $\Gamma_f(t)$ is based on a truncated Taylor expansion in a Lagrangian formulation which corresponds to following a fluid particle,

$$\mathbf{r}(t + \Delta t) = \mathbf{r}(t) + \sum_{k=1}^{m} \frac{(\Delta t)^k}{k!} \frac{D^k \mathbf{r}(t)}{Dt^k} + O[(\Delta t)^{m+1}] \tag{9}$$

and the analogous for ϕ.

All the partial derivatives of ϕ with respect to time satisfy equation (1) so the coefficients of Δt in equation (9) can be found from a sequence $\{\phi, \frac{\partial \phi}{\partial t}, \frac{\partial^2 \phi}{\partial t^2}, ...\}$ of solutions of a succession of Laplace's equations. The expansion coefficients are then expressed as function of $\{\phi, \frac{\partial \phi}{\partial n}, \frac{\partial \phi}{\partial t}, \frac{\partial^2 \phi}{\partial t \partial n}, ...\}$ and of their derivatives along the free surface (s-derivatives). The order of the latter derivatives increases as the order m of the Taylor series (9). Since the s-derivatives have to be computed by numerical differentiation, an operation which loses accuracy in the corners of a physical domain, we have so far limited the series and thus the s-derivatives to second order ($m = 2$). The procedure described can, however, in principle be extended to higher order and, in particular, for space periodic problems where the periodicity conditions can be used to avoid extrapolating the s-derivatives in the corners, higher order time series have been used by others (see Dold & Peregrine (1986) (m=3), Nam Seo (1988) (m=4)).

While the boundary conditions for all Laplace problems are readily obtained along the solid boundaries, the boundary values for $\frac{\partial \phi}{\partial t}$ at the free surface, are obtained from the Bernoulli equation. For $m > 2$, the $\{\frac{\partial^2 \phi}{\partial t^2}, ...\}$ would be obtained from the successive time derivatives of Bernoulli's equation.

In the computations, the terms in (9) are expressed in a local curvilinear coordinate system defined by (s,n), the tangential and normal unit vectors at a point of the free surface. For $m = 2$, the first two Lagrangian time derivatives are needed for evaluating the series. Defining,

$$\cos\beta = \frac{\partial x}{\partial s}\ ,\ \sin\beta = \frac{\partial z}{\partial s}\ ;\ \mathbf{s} = [\cos\beta\ ,\ \sin\beta]\ ,\ \mathbf{n} = [-\sin\beta\ ,\ \cos\beta]$$

we obtain by (4),

$$\frac{D\mathbf{r}}{Dt} = \frac{\partial\phi}{\partial s}\mathbf{s} + \frac{\partial\phi}{\partial n}\mathbf{n} \tag{10}$$

The continuity and irrotationality conditions yield,

$$\begin{aligned} \frac{\partial w}{\partial z} &= -\frac{\partial u}{\partial x} \quad \text{or} \quad \frac{\partial^2\phi}{\partial n^2} = -\frac{\partial^2\phi}{\partial s^2} + \frac{\partial\phi}{\partial n}\frac{\partial\beta}{\partial s} \\ \frac{\partial w}{\partial x} &= \frac{\partial u}{\partial z} \quad \text{or} \quad \frac{\partial^2\phi}{\partial n\partial s} = \frac{\partial^2\phi}{\partial s\partial n} \end{aligned} \tag{11}$$

where $\frac{\partial\beta}{\partial s}$ is the boundary curvature. After some calculations we get,

$$\begin{aligned} \frac{D^2\mathbf{r}}{Dt^2} &= (\frac{\partial^2\phi}{\partial t\partial s} + \frac{\partial\phi}{\partial s}\frac{\partial^2\phi}{\partial s^2} + \frac{\partial\phi}{\partial n}\frac{\partial^2\phi}{\partial n\partial s})\mathbf{s} + \\ &\quad (\frac{\partial^2\phi}{\partial t\partial n} - \frac{\partial\phi}{\partial n}\frac{\partial^2\phi}{\partial s^2} + \frac{\partial\phi}{\partial s}\frac{\partial^2\phi}{\partial n\partial s} + \frac{\partial\beta}{\partial s}\mid\nabla\phi\mid^2)\mathbf{n} \end{aligned} \tag{12}$$

In the same way, $\frac{D\phi}{Dt}$ is obtained from (5) and we then get,

$$\begin{aligned} \frac{D^2\phi}{Dt^2} &= \frac{\partial\phi}{\partial s}(\frac{\partial^2\phi}{\partial t\partial s} + \frac{\partial\phi}{\partial s}\frac{\partial^2\phi}{\partial s^2} + \frac{\partial\phi}{\partial n}\frac{\partial^2\phi}{\partial n\partial s}) + \\ &\quad \frac{\partial\phi}{\partial n}(\frac{\partial^2\phi}{\partial t\partial n} - \frac{\partial\phi}{\partial n}\frac{\partial^2\phi}{\partial s^2} + \frac{\partial\phi}{\partial s}\frac{\partial^2\phi}{\partial n\partial s} + \frac{\partial\beta}{\partial s}\mid\nabla\phi\mid^2) - \\ &\quad g(\frac{\partial\phi}{\partial n}\cos\beta + \frac{\partial\phi}{\partial s}\sin\beta) - \frac{1}{\rho}\frac{Dp_a}{Dt} \end{aligned} \tag{13}$$

where $\frac{Dp_a}{Dt}$ is the total rate of change of the surface pressure in time.

After solving the Laplace problem for (ϕ, $\frac{\partial\phi}{\partial n}$) at time t, we can determine the boundary conditions for the ($\frac{\partial\phi}{\partial t}$, $\frac{\partial^2\phi}{\partial t\partial n}$) problem. Along the free surface, the Bernoulli equation yields,

$$\frac{\partial\phi}{\partial t} = -gz - \frac{1}{2}\mid\nabla\phi\mid^2 - \frac{p_a - p_o}{\rho} \qquad \text{on } \Gamma_f(t) \tag{14}$$

and along the fixed boundaries, we get,

$$\frac{\partial^2\phi}{\partial t\partial n} = 0 \qquad \text{on } \Gamma_b \text{ and } \Gamma_{r2},\ (\Gamma_{r1}) \tag{15}$$

Finally, when $\Gamma_{r1}(t)$ represents a plane piston-wavemaker ($\frac{\partial\beta}{\partial s} = \frac{\partial^2\phi}{\partial n\partial s} = 0$), we have,

$$\frac{\partial^2\phi}{\partial t\partial n} = (\frac{d\,u_p(x_p(t),t)}{d\,t} + u_p(x_p(t),t)\frac{\partial^2\phi}{\partial s^2})\,n_x \qquad \text{on } \Gamma_{r1}(t) \tag{16}$$

3 Numerical implementation

Provided we know the initial conditions at a given time, i.e., the position of the boundary $\Gamma_f(t)$ and ϕ and $\frac{\partial\phi}{\partial n}$ along $\Gamma_f(t)$, we can update the free surface position and the free surface potential to the next time step. When required, the value of $\frac{\partial\phi}{\partial n}$ along the wave generator and its position can also be specified at the next time step (Section 4.2), and the value of $\frac{\partial\phi}{\partial n}$ along the solid boundaries are invariably zero. Hence, boundary values for ϕ or $\frac{\partial\phi}{\partial n}$ can be determined at $t + \Delta t$ and a "*first*" Laplace problem solved which determines ϕ or $\frac{\partial\phi}{\partial n}$ (whichever is unknown) along the entire boundary.

Then, with ϕ and $\frac{\partial\phi}{\partial n}$ known along the free surface, $\frac{\partial\phi}{\partial t}$ can be determined from the Bernoulli equation. Similarly, along the rest of the boundary we can specify $\frac{\partial^2\phi}{\partial t\partial n}$ and hence determine the necessary boundary values for solving Laplace's equation with respect to $\frac{\partial\phi}{\partial t}$ (and so forth for $\frac{\partial^2\phi}{\partial t^2}$,..., when m >2). Since the succession of Laplace problems is expressed for the same geometry of the boundary $\Gamma(t)$, the extra computational effort required to solve them is very small.

For the solution of the Laplace equation in the form (2), we use the Boundary Element method (BEM) (Brebbia, 1978). Collocation nodes are distributed along the entire boundary to describe the variation of boundary geometry as well as boundary conditions and the unknown functions of the problem. Between the collocation points, the variation of all quantities is described by means of shape functions, and for this purpose, the boundary is divided into elements each of which contains two or more nodes. In most of the computations reported here, quadratic isoparametric or quasi-spline elements have been used. The latter elements describe the geometry by regular cubic splines and the field functions ϕ, $\frac{\partial\phi}{\partial n}$, etc. by linear shape functions. The quasi-spline elements are used on the free surface in some of the applications; they require small extra computational effort for enforcing the inter-element continuity of the derivatives. As in finite element methods, mapping of the boundary elements onto reference elements is used and the Jacobian of the mapping function is determined analytically. The regular integrals in (2) are computed by Gaussian quadrature using eight to ten integration points per element (i.e. four or five per interval between the nodes of a quadratic element), and a kernel transformation is applied to the singular integrals which are then computed by a Gauss-like quadrature dealing with the logarithmic singularity. An adaptative numerical integration method is used for improving the accuracy of the regular integrations for the elements close to the corners of the fluid domain. It is based on a binary subdivision of the element to integrate, while keeping the number of integration points constant within each subdivision. Subdivision is performed until the angle from which subdivisions are seen from the source point falls under a pre-set value. The same technique is also used when the distance between two boundaries of the fluid domain tends to vanish (e.g. during wave rundown on a slope). Almost arbitrary accuracy can thus be achieved in the numerical integrations.

After being assembled according to the type of boundary conditions (Dirichlet or Neuman), the algebraic system matrix equivalent to (2), is solved by direct elimination (Kaletsky method) for the first Laplace problem. The geometry is identical for both the Laplace problems we need to solve when $m = 2$, so only the right hand side vector needs to be recomputed to solve the second system.

A sliding 4th order element, independant of the BEM interpolation, is used for the evaluation of the s-derivatives along the free surface. This provides local continuity on the boundary Γ_f of at least the 2nd derivatives.

A double node technique (Svendsen 1971, Brebbia, 1978) is used in combination with some compatibility relationships, to utilize all information given in the corner by the boundary conditions. These compatibility conditions express the uniqueness of the velocity vector at the corner, based on the values of $\frac{\partial \phi}{\partial s}$ and $\frac{\partial \phi}{\partial n}$ on both intersecting boundaries. More details about the method are given in Grilli, Skourup & Svendsen (1989). For details of the implementation of the quasi-spline elements see Grilli & Svendsen (1989b). See also Grilli & Svendsen (1989a) for a discussion about surface piercing bodies such as wavemakers.

4 Wave generation

4.1 *Exact solitary wave*

One main purpose of the computations has been to compare the method with other methods used to analyze the runup and reflection of a solitary wave on a vertical wall. For this purpose the method of Tanaka (1986) is used to generate the free surface elevation $\eta(x,t_o)$ and the potential $\phi(x,t_o)$ (as in (6)) for solitary waves which are exact constant shape solutions of the fully nonlinear constant depth potential flow equations. In the following, these solitary waves are termed *exact* solitary waves for short.

Tanaka's method is based on using Cauchy's integral theorem in a frame of reference moving at the celerity c of the wave, and the crest velocity q_c in that frame defines the wave. Cooker (1989) has modified the method so that the wave height H is prescribed and an approximate crest velocity $\tilde{q_c}$ is estimated by interpolation in a table of values of (H, q_c) predetermined within the interval ($\frac{H}{d}$=0.833197, q_c=0) for the highest wave, to ($\frac{H}{d}$=0,q_c=1) for a flat free surface. From this approximate crest velocity, Tanaka's method determines iteratively the free surface velocity distribution of the wave, an associated Froude number F^2 and a new amplitude $\tilde{H}$ with,

$$F^2 = \frac{c^2}{gd} \; , \; \tilde{H} = \frac{1}{2}(1 - \tilde{q_c}^2)F^2 \tag{17}$$

From this new amplitude, a new crest velocity is re-estimated and so on, until a constant value of H is reached. The convergence criterions selected here are 10^{-10} and 10^{-5} in relative values of F^2 and of the prescribed H, respectively.The method is quite computing time efficient since convergence on both F^2 and H is reached and all the wave data are calculated in less than 0.6s CPU time (IBM-3090/300), with 80 computation points on the free surface.

The resulting wave is finally truncated left and right to points where the free surface elevation $\eta = \varepsilon_z H$, with $\varepsilon_z \ll 1$ chosen in advance.

Dimensionless variables x', z', t' and c' will be used in the discussion of both *exact* and *first-order* solitary waves. They are defined by,

$$x' = \frac{x}{d} \; , \; z' = \frac{z}{d} \; , \; t' = t\sqrt{\frac{g}{d}} \; , \; c' = \frac{c}{\sqrt{gd}} \tag{18}$$

It will be shown in Section 5 that the numerical model can propagate the *exact* solitary waves over long distances of constant depth while conserving their shape and total energy constant within a very small margin.

4.2 *First order solitary wave*

A second main purpose of the computations reported in this paper has been to compare the numerical method to the measurements of Losada, *et al.* (1986) (LVN) (Section 6). They generated waves, in their laboratory wave tank, by moving a piston wavemaker to create a *first-order* solitary wave. We have reproduced that process as closely as possible in the numerical experiments made for comparing with their measurements.

In a wave of permanent form, we have at any instant (Svendsen & Justesen, 1984),

$$\int_{-d}^{\eta} u \ \mathrm{d}z = c_a \eta + Q_s + Ud \tag{19}$$

where c_a is the propagation speed of the wave in a fixed frame of reference, $\eta(x,t)$ is the wave elevation above the still water level, Q_s is the nonlinear mass flux averaged over a wave period, and U, the speed of the current defined as the averaged particle velocity below wave trough level.

In a solitary wave with an infinitely long wave period, the right hand side of (19) simply reduces to $c\eta$ where c is the speed of the wave relative to the water, so that (19) becomes the simpler expression used by Goring (1978) for determining the motion required by a piston wavemaker to generate a specified water surface elevation immediately in front of the wavemaker. Since the piston motion creates a depth uniform horizontal velocity $u_p(x_p(t),t)$ (19) reduces to,

$$u_p\,(d+\eta) = c\eta \tag{20}$$

which means that a required η can be generated by a piston velocity,

$$u_p = \frac{c\eta}{d+\eta} \tag{21}$$

This corresponds to a piston motion $x_p(t)$ given by,

$$x_p(t) = \int_0^t \frac{c\eta}{d+\eta} \ \mathrm{d}\tau \tag{22}$$

To generate a *first-order* solitary wave profile with,

$$\eta(x,t) = H\mathrm{sech}^2[\frac{\kappa}{d}(x-ct)] \tag{23}$$

$$c = \sqrt{g(d+H)} \tag{24}$$

$$\kappa = \sqrt{\frac{3H}{4d}} \tag{25}$$

(23)-(25) have to be substituted into (22) with $x = x_p(t)$ required throughout the integration in order to account for the finite amplitude of the piston [1].

Within the frame of Boussinesq approximation, the inverse scattering theory will predict that, unless it corresponds to an *exact* solitary wave, a distributed elevation of the free surface (as the one generated by the procedure described above) will disintegrate into one or more solitons and a tail of disturbances. Thus, since the procedure only represents the flow in a *first-order* solitary wave, it is expected that when waves of appreciable height are generated using this procedure, disturbances and modifications of the wave profile will occur as it propagates down the wave tank. This will be true in the laboratory experiments as well as in fully nonlinear numerical computations. In other words the deviations between the wave motion generated and an exact solitary wave are essentially associated with two aspects : the amplitudes of the wave considered are not small enough for the KdV type approximation of the flow (like (23)) to give an accurate prediction of the surface profile; and the piston generates a horizontal velocity constant over depth, which is not quite the case in a steep *exact* solitary wave. In fact Goring (1978) found that the limit for an accurate solitary wave reproduction by his method was $\frac{H}{d} = 0.2$. For higher amplitudes, the *first-order* profile (23) deviates more and more from an *exact* solitary wave. Figure 2a shows a comparison between an exact solitary wave of height $\frac{H}{d} = 0.83$ (almost the highest wave) and the corresponding *first-order* profile. One sees the exact wave has a more pronounced peak, but also is somewhat wider in the lowest 30 % of its profile. In fact, theoretical *first-order* profiles, as shown in Figure 2a, will never be obtained with the described wavemaker motion since the wave produced by the wavemaker starts adjusting its shape long before the piston motion is completed, and becomes a wave train consisting of a leading wave and an oscillatory tail.

In the numerical comparisons with LVN's experiments, we have closely duplicated the way they generated their waves. Since the computations solve the full nonlinear equations, the computed waves should be expected closely to follow what actually happens in the wave flume after the generation of the wave motion. Figure 2b shows profiles of waves with four different amplitudes H_i (Figure 1) at the (different) time when the crest of each of them passes a point I, $20d$ in front of the wave generator (see Section 5.1 for details about this choice of an incident wave). In accordance with the comments above, it is found that the higher the waves, the more pronounced is the amplitude A (Figure 1) of the tail of disturbances they are shedding. A closer inspection also shows that, although the highest parts of the crests are closely symmetric, there are non-negligeable differences between front and rear for the lowest 25-35 % of each leading wave profile.

As the waves propagate further away from the wave generator, the asymmetry of the leading wave decreases and the part of the tail closest to the wave turns into a long, shallow trough. Figure 3a shows this in a comparison between two waves of the same height ($\frac{H_i}{d}$=0.25 at x'=86.7), one having propagated only $20d$ since generated, the other after $86.7d$. Figure

[1] Most wave maker theories describe the solution to the problem : What is the wave motion generated by a specified paddle motion. It may be interesting to notice that the procedure described above is the only one (known to the authors) for solving the "inverse" wave generation problem : How do we move the wave maker to generate a wave of a specified (arbitrary) form. Recently Synolakis (1989a) has generalized Goring's wavemaker method to the generation of arbitrary finite-amplitude long waves, by solving an inverse evolution problem of the KdV equation.

3b shows a comparison between the leading wave after propagation over $86.7d$ (as in Figure 3a) and an *exact* solitary wave of the same height. One sees the differences between both profiles are quite reduced. The slow transformation of the wave profile as it propagates and adjusts itself to a stable form, also results in a moderate decrease in wave height. Figure 4 shows the amplitude reduction for the 2 waves of Figure 3a (initial amplitude close to 0.26 times the depth). Although the computations clearly have not been carried far enough, it seems likely that the wave will eventually stabilize at a height only marginally smaller than that found at $x' = 86.7$ where we stopped this computation.

Figure 4 also shows the amplitude variation for the second wave in Figure 3a, generated at $x' = 66.7$ by the piston wavemaker. In order to be of the same height at $x' = 86.7$, it is initially generated slightly smaller. As could be expected, we also find that the transformation of the highest waves occurs much faster than for the smaller waves.

5 Reflection from a vertical wall

5.1 *Wave generation and propagation, numerical data, checks on accuracy*

Before considering the reflection from a slope, we analyze the more simple reflection from a vertical wall and compare it with the results Fenton & Rienecker (1982) (F&R) obtained for that situation using a Fourier Method, with the 3rd order analytic solution of Su & Mirie (1980) (S&M) and with the 5th order analytic solution of Byatt-Smith (1988) (B-S). Reflection of both *exact* and *first-order* solitary waves of amplitude ranging from $\frac{H}{d}$=0.2 to 0.6 is computed. The *exact* waves will allow for a direct comparison with S&M, F&R and B-S results (Sections 5.2, 5.3, 5.4, 5.5, 5.6), whereas the *first-order* waves, which represent the waves generated in the laboratory experiments, will be used to show how close to the *exact* wave runup these waves can be expected to be.

Numerical data and results are presented in Table 1 and 2 for the *exact* waves and in Table 3 for the *first-order* waves. Computational considerations and checks on accuracy are discussed in the following.

Exact solitary waves :

The *exact* waves are generated, with $\varepsilon_z = 5.10^{-6}$ to 10^{-5}, at the mid-point of a tank of length L=$28d$ to $37.8d$, whose free surface is discretized by 85 to 113 equally spaced nodes (step $\Delta x'$ as in Table 1). The total number of nodes of the BEM discretizations is 184 to 242. Quasi-spline elements (2-node) are used on the free surface, linear elements (2-nodes) on the lateral boundaries and quadratic elements (3-node) on the bottom, corresponding to a total of 140 to 184 elements. The discretization step is twice as large on the bottom as on the free surface (i.e. half the number of nodes is used there). To improve the accuracy of the integrations close to the surface corners, the discretization on the vertical wall is stretched, as suggested by Klopman (1988), according to an exponential law which forces the upper element length on the wall (closest to the free surface) to be the same at all times as the one of the last element on the free surface. The other elements on the wall are, accordingly, becoming wider towards the bottom. The time step $\Delta t'$ varies between 0.04 and 0.09 for an horizontal propagation and from 0.01 to 0.045 during reflection on the wall (Table 1). The computation time varies between 1.44s to 2.34s CPU per time step (IBM-3090/300), of

$\frac{H}{d}$	c'	m	e_k	e_p	e_t	$\Delta x'$	$\frac{L}{d}$	$\Delta t'$
0.20	1.09434	1.097652	0.077477	0.072295	0.149772	0.45	37.80	0.09-0.450
0.30	1.13752	1.370744	0.148068	0.134314	0.282382	0.40	33.60	0.07-0.035
0.40	1.17808	1.600518	0.233938	0.206929	0.440867	0.33	28.67	0.06-0.030
0.50	1.21578	1.791479	0.330198	0.285514	0.615712	0.25	28.00	0.05-0.025
0.55	1.23339	1.871258	0.380025	0.325134	0.705158	0.25	28.00	0.04-0.010
0.60	1.24999	1.938826	0.429220	0.363516	0.792735	0.25	28.00	0.04-0.010

Table 1: *Exact* solitary wave data (dimensionless variables computed by Tanaka's (1986) method) : $\frac{H}{d}$is the wave height, c' the wave celerity, m the wave mass (area in 2D), e_k the wave kinetic energy, e_p the wave potential energy, $e_t = e_k + e_p$ the wave total energy. $\Delta x'$ is the spatial step of the initial BEM free surface discretization, $\Delta t'$ the time step and $\frac{L}{d}$ the length of the numerical wave tank. The unit for the energy results is $\rho g d^3$ and for the mass results ρd^2, both per unit of width.

which 2 to 9% are used for data postprocessing.

Two levels of checks on accuracy are made on the *exact* waves. The first compares the energy and mass of the wave computed at the first time step after initial time $t'_o = 0$, with the *exact* values e_t and m as predicted by Tanaka's method (Table 1). This gives $\Delta^T e_t$ and $\Delta^T m$ (Table 2). The Δ^T's reflect both the effects of wave truncation at $\varepsilon_x H$ and the small changes the *exact* wave shape $\eta(x', t'_o)$, potential $\phi(x', t'_o)$ and normal velocity $\frac{\partial \phi}{\partial n}(x', t'_o)$ have to undergo at the first time step to adjust from the discretization of Tanaka's method to the BEM discretization. Table 2 shows the Δ^T's generally are of the order of a few hundredths of a percent. The second level provides the maximum absolute deviation of the energy and mass during the whole BEM computation, relative to the first time step. This gives $\Delta^o e_t$ and $\Delta^o m$ (Table 2). The Δ^o's reflect the accuracy of the computations, over more than 1000 time steps. Though some values go up to 0.1%, it is worth noticing that during, horizontal propagation, they generally are of the order 0.01% and that the higher variations are observed during reflection on the wall. Both total energy and mass, however, are observed, after reflection, to get back close to their initial values by a few hundredths of a percent.

Figure 5 shows the variations in e_t and m during the computations with $\frac{H}{d}$=0.5. Comparing the variations of the curves in Figure 5a and 5b, it is apparent that, during the runup-rundown of the wave, the (somewhat larger) change in total energy is quite well matched by a similar change in volume. This suggests that the (fixed though reduced) time step used in the computations is too large to account for the rapid changes in surface position during the short interval of the process where the surface is moving really fast up and down along the wall.

First-order solitary waves :

The *first-order* waves are generated in a tank of length $L = 33.33d$. Since the amplitude of a *first-order* wave slightly decreases during propagation (Figure 4, Section 4.2), the initial amplitude imposed at the wavemaker is adjusted so that the desired value of the incident

$\frac{H}{d}$	$\frac{R_u}{d}$	$\frac{R_d}{d}$	F_x^{max}	M_b^{max}	$10^4\Delta^T m$	$10^4\Delta^T e_t$	$10^4\Delta^o m$	$10^4\Delta^o e_t$
0.20	0.42920	0.00058	1.8775	2.6486	1.29	0.49	7.9	6.3
0.30	0.66873	0.00179	2.3058	3.7220	2.03	0.54	9.0	4.2
0.40	0.93673	0.01758	2.6809	4.8077	3.03	1.75	13.8	10.1
0.50	1.25308	0.05250	3.0693	5.9454	3.62	2.21	4.8	10.9
0.55	1.47937	–	3.2808	6.6075	2.97	4.75	8.0	8.6
0.60	1.67100	–	3.5034	7.3471	3.58	6.88	6.9	10.2

Table 2: *Exact* solitary waves BEM results (dimensionless variables) : $\frac{R_u}{d}$ is the maximum runup value, $\frac{R_d}{d}$ the rundown, F_x^{max} the maximum horizontal pressure force and M_b^{max} the maximum moment with respect to the toe of the wall on the bottom, $\Delta^T m$ and $\Delta^T e_t$ the difference between computed and exact (Tanaka's) values of mass and total energy at the first time step and $\Delta^o m$ and $\Delta^o e_t$ the absolute maximum mass and energy change over the BEM computations (with respect to the first time step values).

wave amplitude $\frac{H_i}{d}$ is obtained at a given position x' (the slightly higher initial wave to be imposed to the wavemaker is determined by trial and error). As in the laboratory experiments we analyze later on, a location $13.3d$ in front of the vertical wall is selected for the incident wave (x'=20, Figure 1), where the effect of the wall is not yet too sensitive .

The *first-order* waves are generated, with $\varepsilon_z = 10^{-3}$ in a tank in which the free surface is discretized by 81 to 137 equally spaced nodes (step $\Delta x'$ as in Table 3). The number of nodes on the bottom is half this and the total number of nodes of the BEM discretizations is 138 to 222. The type of the elements on the various parts of the boundary is the same as in the computations of the *exact* waves, with a total of 118 to 186 elements. Exponential stretching of the nodes along the vertical wall is used as well. The time step $\Delta t'$ varies between 0.040 and 0.090 and is reduced to half that during reflection on the wall (Table 3). The computation time varies between 1.21s to 2.46s CPU per time step (IBM-3090/300).

The accuracy of the *first-order* wave computations is checked the same way as with the *exact* waves, by computing the maximum absolute changes in mass and total energy. Since waves are generated from rest by the wavemaker, however, both energy and mass gradually increase from zero up to a maximum value (termed "level" value at a time t'_l defined as the time where energy first stops increasing). Numerical errors are quite difficult to estimate before time t'_l is reached. For later times, both errors are defined relative to the values of the energy and mass at time t'_l and thus termed $\Delta^l e_t$ and $\Delta^l m$. It is found that, at t'_l, the maximum amplitude of the incident waves is located between $x'_l = 5.6$ and 20.9, depending on the wave height. Values of $\Delta^l e_t$ and $\Delta^l m$ are given in Table 3 for the computed waves. They show values of the same magnitude as for the *exact* waves the Δ^o's in Table 2 [2].

As for the *exact* waves, we find that for most of the propagation of a *first-order* wave of $\frac{H}{d}$=0.456 (the highest wave, we will use in the comparison with the experimental results in

[2] Notice the error on total energy, for both *exact* and *first-order* waves, is found to be proportional to $\Delta x'$, which shows the effect of the spatial discretization on the accuracy of the solution by the BEM, and to $\Delta t'^3$, which is consistent with the second order accuracy of the time integration.

Section 6), the total energy e_t remains constant to within 0.01%, except in the brief interval of the rapid surface movements at the wall where it increases by about 0.06%.

5.2 *Runup*

One might expect that, for a *first-order* wave, the oscillatory tail should not influence too much the runup but should have a more significant effect later on in the reflection process when the tail interacts with the reflected wave. Figure 6 shows the maximum surface elevation of a *first-order* wave as it approaches the wall and after it has been reflected. The wall is placed at $x' = 100$ and results are shown for the same two waves as in Figure 3a and 4 ($\frac{H_i}{d}$=0.25) to indicate the effect which the small differences between those two waves have on the maximum elevations and after reflection. The two waves have almost equal runup values and both come out of the reflection process with a somewhat smaller amplitude. Notice that only the maximum elevation is shown, not the envelope of the free surface positions. That results in the spike from the highest position A near the wall, to the runup position B at the wall. This is because the maximum elevation is at the wall throughout the time it takes the surface to move from A to B and back to A'. Immediately after reflection, the amplitude decrease is almost 10%, but at some distance from the wall it settles at 3-5 %. This is comparable to the approximately 3 % decrease found by F&R, though the results for the reflected wave show some variation (as expected) due to the interaction with the incoming tail. This transient decrease of the wave amplitude after reflection will be studied in detail, for an *exact* wave of $\frac{H}{d}$=0.5, in Section 5.3.

In Figure 7, the maximum elevation ("runup", R_u) at the wall, computed for different amplitudes of the *exact* and *first-order* waves is compared to the third order results by S&M and to the F&R's computations (the results are also in Table 2 and 3).

Up till amplitudes about $\frac{H}{d}$=0.4, the BEM results for the *exact* waves are almost identical with those of S&M and F&R. Above that value, the third order theory predicts slightly smaller runup which means that for high waves ($\frac{H}{d} > 0.4$), the runup contributions of order higher than 3rd in $\frac{H}{d}$are important. This ties well in with B-S's results that show that other effects occuring during wave reflection are of 5th order in $\frac{H}{d}$(Section 5.3). The Fourier method by F&R coincides very closely with the present results even for the highest wave of amplitude 0.5161 computed by that method (in spite of F&R's own comment about the reduced accuracy of their method for ampitudes above 0.4554). .

The runups of the *first-order* waves are slightly smaller that for the *exact* waves, above amplitudes $\frac{H}{d}$=0.3. This is likely due to the effect of the oscillatory tail the *first-order* waves shed behind them which, for sufficiently high waves, removes enough energy from the leading wave to reduce its runup significantly.

BEM results for the reflection of *first-order* waves from a steep slope will be compared in Section 6 with detailed experiments made by Losada, *et al.* (1986). Some of these experiments correspond to a vertical wall and their results are listed in Table 5 for $\theta = 90°$. The corresponding computations are also listed in Table 6. It appears that computed and measured runup values $\frac{R_u}{d}$ agree quite well (within 4.8% and 3.0% for waves of $\frac{H}{d}$=0.255 and 0.456 respectively).

$\frac{H_i}{d}$	$\frac{R_u}{d}$	$\frac{R_d}{d}$	F_x^{max}	M_b^{max}	c'	$\Delta x'$	$\Delta t'$	$10^4\Delta^l m$	$10^4\Delta^l e_t$
0.200	0.425	0.003	1.864	2.623	1.095	0.42	0.09-0.045	10.6	8.14
0.255	0.547	0.007	2.093	3.172	1.121	0.42	0.08-0.040	11.6	8.98
0.300	0.654	0.015	2.257	3.625	1.136	0.42	0.07-0.035	10.7	7.72
0.400	0.910	0.038	2.638	4.685	1.183	0.33	0.06-0.030	7.94	4.87
0.456	1.074	0.055	2.844	5.280	1.204	0.33	0.05-0.025	8.10	6.23
0.500	1.215	0.068	3.031	5.806	1.228	0.24	0.05-0.025	3.90	8.80
0.600	1.583	–	3.402	6.999	1.260	0.24	0.04-0.020	7.5	11.5

Table 3: *First order* solitary waves BEM results (dimensionless variables) : $\frac{H_i}{d}$ is the incident wave at $x' = 20$ (13.3d in front of the wall). The seven first columns are as in Table 1 or Table 2 and $\Delta^l m$ and $\Delta^l e_t$ are the absolute maximum change in wave mass and energy over the BEM computations (with respect to the "level" values).

5.3 *Rundown and reflected wave*

Figure 8a shows the maximum depression of the water surface as a function of the wave amplitude ("rundown" or "rush-down", R_d) for both *exact* and *first-order* waves (these results are also in Table 2 and 3). The rundown value is significantly higher for the *first-order* waves (in particular for $\frac{H}{d}$<0.3) probably due to superposition with the shallow trough following those waves (in their (incoming) oscillatory tail). Notice that the measured rundown, in the experiments refered to above (Section 5.2), for a *first-order* wave of $\frac{H}{d}$=0.456 agrees to within 5% with the computed value (see Tables 5 and 6).

The highest *exact* waves also develop negative surface elevation after reflection as a start of the (actual) oscillatory tail which is created for those waves by the reflection process. Figure 8b confirms this by showing computed profiles of *exact* waves of height 0.2 to 0.5 reflected from the wall at $x' = \frac{L}{d}$ (Table 1). One clearly sees oscillatory tails develop behind the reflected waves, and increasingly so for increasing $\frac{H}{d}$ (for $\frac{H}{d}$=0.5, the maximum depression in the tail is close to -10% of the wave height, a value similar to the corresponding R_d). Both S&M and B-S theoretically predicted that, to the 3rd order in $\frac{H}{d}$, an oscillatory tail should appear after reflection. F&R, however, could not produce oscillatory tails in their computational results, presumably due to their Fourier method which essentially assumes that their waves are periodic (see comments by B-S).

Figure 9a shows a comparison between an incident *exact* wave of $\frac{H}{d}$=0.5, at its initial location x'=14 (or 14d from the vertical wall positioned at $x' = \frac{L}{d} = 28$), and the corresponding reflected wave which propagates back through the same location. A decrease in wave height ($\Delta\frac{H}{d}$=0.0313 or 6.2% of $\frac{H}{d}$) after reflection is observed and a well developed oscillatory tail follows the leading wave. Before analyzing this further, notice the reflected wave height $\frac{H_r}{d}$ measured at 13.3d from the vertical wall in the experiments refered to above (Section 5.2), for a *first-order* wave of $\frac{H_i}{d}$=0.456, shows a decrease in height of 8.7% (see Tables 5 and 6). Though this wave is not quite an *exact* solitary wave and is slightly smaller in height, this experimental result somewhat (qualitatively) confirms our computational observations.

The variation in wave height after reflection is shown in Figure 9b (solid line) for the

same wave of initial amplitude $\frac{H}{d}$=0.5 [3]. We see that, after an initial reduction of about $\Delta\frac{H}{d}^{max} = 0.0556$, around the time of the rundown, the amplitude of the reflected main wave is continuously increasing. S&M obtained an oscillatory tail, to the 3rd order in $\frac{H}{d}$, but did not find any change in amplitude. Mirie & Su (1982) numerically found a change in amplitude of less than third order in $\frac{H}{d}$. F&R noticed a 3rd order reduction in the wave amplitude after reflection ($\Delta\frac{H}{d}^{max} \simeq 0.4(\frac{H}{d})^3$, curve fitted to their numerical results), but could not obtain an oscillatory tail. B-S, finally, predicted both a reduction in amplitude of the reflected wave and the creation of an oscillatory tail. He derived an analytic expression for the transient change in amplitude of the wave after reflection and showed that the oscillatory tail is responsible for this reduction(a simple energy balance demonstrated that the leading reflected wave gives energy to the oscillatory tail at the time of the reflection and that, accordingly, its amplitude decreases by $\Delta\frac{H}{d}^{max}$). B-S confirmed that the change in amplitude is proportional to $(\frac{H}{d})^3$, as found by F&R. In particular, the maximum amplitude reduction measured from his Figure 1 and scaled for our case by 0.125, gives a reduction of $\Delta\frac{H}{d}^{max} \simeq 0.0612$, to be compared with our value of 0.0556 mentioned at the beginning of this paragraph (notice, with the F&R's results, we would get a value of 0.05). The reflection considered by B-S is obtained by analyzing the situation when two opposing waves of the same height meet. He developed analytic expressions to 5th order for the tail, but had to introduce the additional approximation that the phase ξ_2 of the "reflected" wave is infinitely large, even at limited time τ_2 after the meeting of the crests.

To make a complete comparison with the expression derived by B-S for the transient loss in amplitude, we need to relate its time scale τ_2 to our dimensionless time scale t'. The relation is,

$$\tau_2 = \frac{1}{2}\epsilon^{\frac{3}{2}}\sqrt{3}(t' - t'_2) \tag{26}$$

where $\epsilon = \frac{H}{d}$ and t'_2 is the time when, in our computations, the reflected wave leaves the wall (with $\frac{H}{d}$=0.5 or $\Delta\frac{H}{d}$=0 in the Figure 9b). In our case, we find $\tau_2 = 0.3062(t' - 13.582)$. Measuring on the curve from B-S's Figure 1, we then obtain the dashed curve in Figure 9b. The agreement between the curves in this Figure is quite good for large $(t' - t'_2)$ but the discrepancies are larger when $(t' - t'_2)$ or τ_2 is small. We believe this is partly due to the effect of the limited order of B-S's analysis (5th order in ϵ) whereas we solve the exact equations, and partly due to the asymptotic hypothesis, B-S makes for deriving his analytical expressions ($\xi_2 \to \infty$ at a fixed time τ_2), which corresponds to the "reflected" wave being far from the "wall".

Although the amplitude of the reflected wave recovers somewhat as the wave moves away from the wall, it will not return to its initial value, however, because a certain amount of energy is lost to the tail. This is further illustrated in Figure 9c and d (solid line) which shows the difference between the incoming wave and the reflected wave at two different positions at distance x'_o=14 (for t'=23.525) and x'_o=6.185 (for t'=29.975), the first of which is equivalent

[3]The wave amplitude variation of this wave has been determined from the BEM results by getting the value of the elevation at the 8 to 10 integration points defined within each quasi-spline element of the free surface boundary, for a series of free surface profiles separated by 0.125 to 0.25 in time t' (according to the rate of variation of the amplitude). We thus get roughly 1000 points per free surface profile, and select the maximum amongst them for obtaining one point in the solid curve of Figure 9b.

to the location in Figure 9a. It is seen that the difference wave consists of a depression under the crest of the main wave, accounting for the transient reduction in amplitude $\Delta\frac{H}{d}$, and the actual tail. In Figure 9c and d are also shown B-S's 5th order expressions for the oscillatory tail (dashed line). From (26), B-S's τ_2 can be calculated and the two situations in Figure 9c and d have been chosen as time steps of our computations with $\tau_2 = 3.04$ and 5.02 respectively, which corresponds closely to the τ_2 values of 3 and 5 of B-S Figures 2d and f [4]. This also corresponds to situations where the reflected waves are $14d$ and $21.815d$ (i.e. $28 - x'_o$) from the wall respectively, which means that B-S assumption of large phase is reasonably well satisfied. The similarity between the results of the two methods is apparent although there also are some significant differences. In particular the agreement between both the curves in the Figures is quite good around the maximum of the main wave (wave of depression at $x'_o - x' = 0$). B-S theory predicts, however, a much less pronounced decay rate for the tail than does the numerical computations, perhaps because that part of the tail is closer to the reflection point and hence is like to invalidate the large phase assumption (when x' increases the tail gets closer to the wall).

Finally it is mentioned that the transient change in amplitude of the reflected wave has been studied experimentally by Seabra-Santos (1985) who confirmed both the approximate relationship computed by F&R for the maximum amplitude reduction $\Delta\frac{H}{d}^{max}$ and the slow increase in amplitude, when the reflected wave propagates backwards in the wave tank. Seabra-Santos (1985) also measured the maximum amplitude of the tail $\frac{A}{d}$ (Figure 1) after reflection for the wave of lowest height, i.e. $(\frac{H}{d} - \Delta\frac{H}{d}^{max})$, and found $\frac{A}{d} \simeq 0.5(\frac{H}{d})^{2.9}$ (curve fitted to his experimental results) whereas B-S finds $\frac{A}{d} \propto (\frac{H}{d})^2$. This relationship is thus of an order slightly higher than the 2nd order found by B-S. The measurements however took place in an area close to the vertical wall, whereas B-S's asymptotic hypothesis only makes his results valid far from the reflection point.

5.4 *Celerity and phase shift*

A phase diagram equivalent to F&R's Figure 10 has been developed for the *exact* wave of $\frac{H}{d}$=0.5 we consider in Figure 9. The solid line in Figure 10a represents the relationship between t' and x' for the point of maximum wave amplitude $\frac{H}{d}$ determined as in Figure 9b (its lower part corresponds to the wave before reflection, and its upper part to the wave after reflection), and its slope is a measure of the wave celerity.

The lower and upper dashed lines in the Figure are obtained by least square fitting to the results for $x' < 20$ before and after reflection, respectively. These lines give a measure of the average incident and reflected wave celerity $(\overline{c'_i}, \overline{c'_r})$ and one finds : $\overline{c'_i} = 1.2168$ and $\overline{c'_r} = 1.2226$. The celerity of an *exact* solitary wave of $\frac{H}{d}$=0.5 is c'=1.2158 (as computed in Table 2 with Tanaka's (1986) method) and our incident wave is thus slightly faster (0.085%) corresponding to an average incident wave height (over x'=14 to 20) $\frac{H_i}{d} = 0.5008$. This is likely to be due to the small changes the solution provided by Tanaka's method has to undergo to adjust to the BEM discretization and solution (see also Section 5.1), which cause the wave to slightly increase its height right after the first time step. The average reflected wave is

[4] By comparing B-S Figures 1 and 2 and considering his equation (6.11), there seems to be a factor two error in B-S's Figure 2. We believe, Figure 2 actually a plot of $2\tilde{u}_1(\xi_1, \tau_2)$ and should thus be scaled by a factor $\epsilon^3 = (\frac{H}{d})^3$ (like in B-S's Figure 1) rather than by $2\epsilon^3$ as indicated by B-S.

found to be $\frac{\Delta c'}{c'_r}$=0.47% faster than the incident wave, though it is of smaller amplitude as seen in Section 5.3. A similar observation has been made by F&R who interpreted it as being due to the unsteadiness of the wave after reflection as demonstrated above (Figure 9). F&R, however, computed a much larger increase in celerity than ours : they found $\Delta c' \simeq 0.64(\frac{H}{d})^3$ which would give $\frac{\Delta c'}{c'_r}$=6.56% for the case discussed here. A higher celerity after reflection has also been observed by Seabra-Santos (1985) in his experiments.

Based on the Figure 9b and 10a, however, we can see, the wave height and celerity substantially change after reflection and over an horizontal distance of several depths. Hence, the computations have to be carried out long enough before estimating $\overline{c'_r}$ (as done in the present study). B-S, further, points out that a solitary wave having reached its permanent form cannot be smaller and faster, since the wave celerity is a monotonic increasing function of $\frac{H}{d}$(when the waves are not close to the maximum). According to his asymptotic results, the reflected wave should recover its initial height, thus its speed, when time tends to infinity. However, since part of the leading wave energy has been transmitted to the oscillatory tail, we believe the wave cannot recover its initial height because energy is also a monotonic increasing function of $\frac{H}{d}$. Thus a permanent reduction in amplitude should be observed even after a very long time. The celerity should thus eventually be smaller for the leading reflected wave as it approaches permanent form.

Figure 10b is a closer view of the right part of the Figure 10a ($x' \geq 24$). It clearly shows how widely the wave celerity varies in the area close to the wall, before and after reflection. It also shows the phase shift of the wave, during reflection, which leads to a time phase lag $\Delta t'$=0.627, measured between B and C on the wall (identified by the intersection with the lines representing $\overline{c'_i}$ and $\overline{c'_r}$) or to an instantaneous spatial phase lag $\Delta x'$=0.763, measured between C on the wall and E on the line B-F representing a perfect reflection of the incident wave. As phrased by F&R : "the time phase lag expresses how much longer the wave remains against the wall than if it had been instantaneously reflected like in a perfect reflection". Since the celerities before and after reflection differ slightly, B-F and C-G will, in theory, eventually intersect as time increases, thus $\Delta t'$ and $\Delta x'$ will gradually vanish. Since, however, the celerity of the reflected wave should eventually decrease as the wave stabilize its shape, permanent but reduced time and space phase lags should be observed in the long term.

All these observations tie qualitatively well in with the phase lag at the time of maximum amplitude found by Maxworthy (1976), Oikawa & Yajima (1973), S&M, and F&R. S&M estimated to the 3rd order in $\frac{H}{d}$, immediate and long term time and space phase lags. From their analysis we get ($\frac{H}{d}$=0.5) values of $\Delta t'$={1.505 ,0.485} and $\Delta x'$={1.607,0.587} for the immediate and long term phase lags, respectively. Thus, their immediate values are more than twice our results. F&R did not compute lags for a wave of $\frac{H}{d}$=0.5 (they did not trust their results for $\frac{H}{d} \geq$0.45) but they got results increasing with $\frac{H}{d}$ and obtained $\Delta t'$=1.12 for $\frac{H}{d}$=0.4554. Hence, they also got much larger results than ours.

It is finally pointed out that the relative difference in celerity c' between the *first-order* waves (see Table 3) and the *exact* waves (Table 1) is positive and quite small up to amplitudes of $\frac{H}{d}$=0.2 (< +0.06%) where the differences in profile are small (Section 4.2). The difference remains small up to $\frac{H}{d}$=0.456 (< +0.40%) and grows near +1.00% for the highest waves considered. Hence in all cases it is found that the first order waves travel faster than

$\frac{H}{d}$	e_{ko}	$10^4\Delta^T e_k$	$\frac{e_k^{min}}{e_{ko}}(\%)$	$\Delta^{R_u}t'$	$\frac{\Delta e_k}{e_{ko}}(\%)$	$t'(R_u)$	$t'(R_d)$
0.20	0.077480	0.36	0.0259	0.045	0.068	17.82	29.34
0.30	0.147953	7.74	0.1167	0.070	0.159	15.02	25.90
0.40	0.233696	10.4	0.3520	0.120	0.301	12.54	17.10
0.50	0.329923	8.33	0.7859	0.200	0.543	12.05	16.18

Table 4: *Exact* solitary wave variation in kinetic energy in the computations (dimensionless variables) : e_{ko} is the wave kinetic energy at the first time step and $\Delta^T e_k$ its difference from exact (Tanaka's) result, $\frac{e_k^{min}}{e_{ko}}$ is the relative minimum of the kinetic energy during runup and $\Delta^{R_u}t'$ the (negative) time difference from the time of maximum runup $t'(R_u)$ at which this minimum occurs, $\frac{\Delta e_k}{e_{ko}}$ is the drop in kinetic energy : first relative minimum after the time of rundown $t'(R_d)$.

exact waves of the same height, likely so because they are bulkier and show less frequency dispersion.

5.5 *Energy partition*

Figure 11a shows the variation in time of both the kinetic energy e_k and the potential energy e_p during the BEM computations for an *exact* wave of $\frac{H}{d}$=0.5; e_{ko} represents the kinetic energy of the wave at the first time step after the start of the BEM computations and $\Delta^T e_k$ is the slight shift this represents from the initial Tanaka's value at time t'_o=0 (Table 1), caused by the shift to the BEM numerical scheme (e_{ko} and $\Delta^T e_k$ are given in Table 4 as function of $\frac{H}{d}$) . We see on the Figure that the kinetic energy reaches its minimum e_k^{min} a fraction of a time unit ($\Delta^{R_u}t'$) before the time of maximum runup ($t'(R_u)$) and that it never becomes quite zero. Also it is seen (Table 4) that both these variables increase with $\frac{H}{d}$. These observations seem to be related to the velocity patterns we show later (Section 6.3) of the runup of high waves on slopes where part of the flows starts moving down while the tip of the wave is still moving up along the slope; thus at $t'(R_u)$, part of the wave is in motion even though its tip is at rest.

F&R found that the changes in the wave caused by the reflection were associated with a slight decrease in the kinetic energy and a similar increase in the potential energy, while the total energy stayed constant (within their numerical accuracy). If we look closer at the energy partition after the runup, we see in Figure 11b, there is such a decrease in kinetic energy Δe_k, on a more or less permanent basis after the rundown at $t'(R_d)$. Table 4 shows this decrease in kinetic energy is an increasing function of $\frac{H}{d}$(the value Δe_k in Table 4 is the drop in kinetic energy corresponding to the first local minimum of e_k after the rundown, e.g. point A in Figure 11b). Notice, F&R's figure for a wave of height 0.2134 has $\frac{\Delta e_k}{e_{ko}}$=0.135% against $\sim$ 0.092% found here by linear interpolation between the values at $\frac{H}{d}$=0.20 and 0.30. Figure 11b also shows the kinetic energy is sligthly increasing on a longer term basis (and the potential energy is decreasing accordingly, within the accuracy of the total energy conservation). We find, e.g., a value of the relative energy reduction

at $t' = 29.975$, decreased to 0.384% in this case (against 0.543% around the time of the rundown). All these observations are in accordance with the analysis presented above of the changes in shape, amplitude and celerity of the reflected waves (Sections 5.3, 5.4).

5.6 *Horizontal forces and moments*

F&R computed total maximum horizontal forces and moments (with respect to the bottom) of waves acting on the wall, and S&M calculated them to the 3rd order in $\frac{H}{d}$. Figure 12a and b show a comparison of our BEM solution for both *exact* and *first-order* waves with these results (our results are also listed in Table 2 and 3). F_x represents the horizontal pressure force on the wall, calculated by the Bernoulli equation (14) integrated over the wall, made dimensionless by dividing it by the hydrostatic pressure force at still water level : $\frac{1}{2}\rho g d^2$ and, similarly, M_b represents the moment with respect to the bottom of the wall divided by $\frac{1}{6}\rho g d^3$. In view of the close agreement described above (Section 5.2) for the runup values, it is not surprising that our BEM computations for the *exact* waves give results that coincide very well with the earlier results by S&M and F&R up to a wave of $\frac{H}{d}$=0.5. For higher waves, slightly higher values are (again) obtained with the *exact* waves.

A somewhat surprising result is a double maximum found in the time variation of the total force (and moment) for high waves as shown in Figure 13a for the *exact* waves (similar results were also obtained for the *first-order* waves). A wave of $\frac{H}{d}$= 0.4 already shows signs of an extended maximum, and for $\frac{H}{d}$= 0.5 there are distinctively two extremes on the force curve. For higher waves ($\frac{H}{d}$=0.55 and 0.6), the computations broke down at the time of the second maximum in a situation with essentially zero pressure and a free falling water volume near the crest. No attempt was made to investigate this further.

Figure 13b shows details for the wave of $\frac{H}{d}$=0.5 and gives a simultaneous picture of the force F_x, moment M_b and the surface elevation at the wall η' as a function of time t'. One sees F_x first reaches its absolute maximum F_x^{max}=3.069 at t'=11.15, at which time the surface elevation η' is at 0.967. Then M_b reaches its absolute maximum M_b^{max}=5.945 at t'=11.33 and η'=1.058. Both F_x and M_b reach local minima, slightly after the maximum runup R_u=1.253 at $t'(R_u)$=12.05, and, finally, second maxima slightly smaller than the first.

It is interesting that Nagai (1969) experimentally observed similar double maxima in the horizontal force exerted on vertical walls by steep standing periodic waves in shallow water.

6 Reflection from a steep slope

6.1 *Description of Experiments by Losada, et al.*

Losada et al. (1986) (LVN) have reported detailed measurements of the runup and reflection of solitary waves from steep plane slopes. Their experimental facility was equivalent to the arrangement shown in Figure 1 except that the length of the flume was L = 160 to 165d, i.e. between 48.0m and 49.6m depending on the slope, with a water depth over the horizontal part of d=0.3m.

The experiments included (*first-order*) solitary waves with height to depth ratios $\frac{H}{d}$ of approximately 0.065, 0.267 and 0.457 on four different smooth slopes, θ = 17.9°, 45°, 70° and 90°. In our comparisons we will concentrate on the results for the two steepest waves.

θ	$\frac{H_i}{d}$	$\frac{H_r}{d}$	K_r	$\frac{\mathcal{R}_u}{d}$	$\frac{\mathcal{R}_d}{d}$
90°	0.255	0.224	0.882	0.521	0.003
90°	0.456	0.419	0.918	1.107	0.059
70°	0.259	0.232	0.893	0.568	0.004
70°	0.437	0.402	0.920	1.071	0.103
45°	0.269	0.214	0.796	0.672	0.129
45°	0.457	0.347	0.759	1.294	0.267

Table 5: Experimental results from Losada *et al.* (1986) : ***First-order*** solitary waves on a slope θ. $\frac{H_i}{d}$ is the height of the incident wave at $x = 20d$ and $\frac{H_r}{d}$ the height of the reflected wave at the same location. $\frac{\mathcal{R}_u}{d}$ and $\frac{\mathcal{R}_d}{d}$ are the runup and rundown of the wave. $K_r = \frac{H_r}{H_i}$ is the reflection coefficient.

θ	$\frac{H_i}{d}$	$\frac{H_r}{d}$	K_r	$\frac{\mathcal{R}_u}{d}$	$\frac{\mathcal{R}_d}{d}$
90°	0.255	0.247	0.964	0.547	0.007
90°	0.456	0.417	0.915	1.074	0.055
70°	0.259	0.243	0.937	0.580	0.013
70°	0.437	0.376	0.861	1.066	0.099
45°	0.269	0.224	0.833	0.673	0.134
45°	0.457	—	—	1.262	0.186

Table 6: BEM computations : Solitary wave on a slope θ. (see Table 5)

We shall also omit the 90° case (which was discussed in Section 5), and the results for 17.9° where all but the smallest waves break. Our computer program is capable of handling the breaking (see Grilli, *et al.* (1989), Grilli & Svendsen (1989a)), but no experimental details are available about that in LVN, and the computations have to be interrupted at least when the jet plunges into the surface below.

The results of LVN consist of time series of surface elevation recorded at 16 to 21 positions, primarily in the neighborhood of the slope. Also, the runup itself was recorded. The time series were obtained from three wave gauges which were placed at different positions in identical repetitions of each experiment. A high degree of repeatability was ensured by controlling the wave generator by a computer.

6.2 *Comparison with experimental results by Losada, et al.*

The computational region for our comparison with Losada's experiments has the dimensions shown in Figure 1. To reduce the amount of computations, our results are obtained for a flume with a length $L = 33.33d$, i.e. the distance from our wavemaker to the still water level intersection with the slope is 33.33 times the depth (or 10m with LVN's dimensions). This is only about one fifth the length of Losada's wave basin. The minor inaccuracies this leads to are almost entirely concentrated in the tail following the wave as was discussed in Section 4. Hence, the major effect of the reduced computational region is a limitation in the time over which we can meaningfully compare our results with those of Losada's : In our computations the tail meets the reflected wave somewhat before it does in the experiments. As will be seen in the following, however, this does not constitute a major problem since most of the action takes place before that time. It is also found that a new trailing system of high frequency oscillations, quite stronger than in the reflection from a vertical wall, is generated by the runup and reflection process from a slope. In spite of the above mentioned effects of the shortening of the computational wave flume we find that computations compare very favorably with the measurements even for those high frequency parts of the wave motion.

The comparison has been made for the cases of slope angle 45° and 70° for which even relatively steep waves do not break. The number of nodes was (again) considerably higher than required for computation of a plain solitary wave. The reason for this is the desire to obtain sufficient resolution to describe also the higher frequency oscillations in the tail created both by the wave generation, and after the wave reflection. Similarly, to achieve superior accuracy, $\Delta t'$ was chosen several times smaller than was actually found sufficient for the accurate propagation of a solitary wave by Grilli, *et al.* (1989) [5]. Hence, in the present computations, it takes as much as 10-15 time steps for the solitary wave to propagate horizontally one water depth (more exactly $\frac{1}{c'\Delta t'}$ time steps). As mentioned above, even so, at special instances of rapid development during the runup-rundown wave motion, we came close to the limit of accurate reproduction (even though the time step was reduced to half).

In all cases, the computed and measured results have been synchronized at the time of maximum runup which, in the experiments reported, is the only well-defined time available. That means that actual comparison of the temporal development is generally limited to the time after the maximum runup. The form of the wave, however, at that time follows entirely

[5] For waves of $\frac{H}{d}$={0.255,0.456}, the discretization spatial step was $\Delta x'$={0.42,0.33} and the time step $\Delta t'$={0.080-0.04,0.050-0.025} as shown in Table 3 and discussed in Section 5.1.

from the generation and propagation which preceeds the runup as described in the previous Section. And since the agreement with the experimental results is so good after that time, it is anticipated that it would be so also for the preceeding part of the process (this is actually checked in the comparison for θ=70° (Figure 15), where an extra experimental profile was available at a time somewhat before maximum runup).

As detailed in Section 4.2, in our computations we generate the *first-order* waves at $x' = 0$ (i.e., 33.3 water depths from the slope) by simulating a piston-type wavemaker motion, according to Goring's procedure. The amplitude of the wavemaker is adjusted so that when the wave passes $x' = 20$ (i.e., $13.3d$ from the slope), it has the height $\frac{H_i}{d}$={0.269,0.259} or {0.457,0.437}, for θ={45°, 70°} found in the experiments at that point.

Table 5 and 6 show experimental and computed results for both the wave heights and the slopes considered here. One sees the maximum runup figures $\frac{R_u}{d}$ agree well (within 2.5% for $\theta = 45°$ and 2.0% for $\theta = 70°$). The agreement for the rundown figures $\frac{R_d}{d}$ is somewhat less good but notice this was found by LVN to be a quantity quite difficult to measure.

Runup and rundown figures are, in fact, only values of the wave elevation at one point of the free surface. It is thus far stronger a test to compare complete computed free surface elevations with those measured in the experiments. This is first done in Figures 14a and 14b which show how the two considered waves reflect from a 45° slope. The computations are compared with the surface profiles measured by LVN at three different times, of which the first available is the instant of maximum runup (curves a) used for synchronization. The symbols mark data points that have been developed from the original experimental records with the kind assistance of Dr. Losada, and the dotted curve is a spline fit to these points. Notice that although the two sets of data have been synchronized at the instant of maximum runup, their shapes are the result of the wave generation process described above, followed by propagation from the generator to the wall. In general, the agreement is considered good. In the case of the lower wave (Figure 14a), the computed and measured surface elevations at the (same) time of lowest position of the water surface at the slope (curves c) do not quite coincide. The agreement is somewhat better with a profile computed at a time slightly before (0.48 time units or 0.084s in the experiments) the instant of rundown (curve b). This shows that, as pointed out by LVN, both rundown and instant of rundown are quite difficult to measure since the surface motion along the slope is quite significant over a very short period of time (the whole rundown process only lasts a small fraction of a second in the experiments). In the case of the higher wave (Figure 14b) an irregularity occured on the computed surface after the time of the lowest position of the surface (curve b). According to visual observation during the experiments, a backward breaking actually occured at this instant as the main crest moved away from the slope. In the computations, the small irregularity propagates away from the wall and, shortly after (b), this wave rapidly breaks backward while propagating away from the slope, thus terminating the computations. This is the reason why we do not show any computational results corresponding to (c) in Figure 14b. Although the results for this event are fairly consistent we have not shown them here since very few computation points are involved. It is in fact fairly evident that at this point we are close to the resolution possible with the number of nodes and the time step used. The rapid development of so small patterns stresses the computations to their limit.

Figure 15a and 15b show the results for a 70° slope. Here an extra profile (curves a) is available in the experiments before the wave reaches the slope. As in the first case,

the agreement between physical and numerical experiments is surprisingly good. Notice that even the oscillatory tail left after the main crest has cleared the slope is quite well represented. This both attests to the care exercised in the experiments and to the accuracy of the computational technique. In the case of the smaller wave (Figure 15a), we have shown curves corresponding to both the measured and the computed times of rundown (curves c and d). In the case of the higher wave, though the various times coincide quite well, the reflected wave is somewhat higher in the experiments (curves c and d). This could be due to the differences in the incident wave, which looks somewhat bulkier in the experiments (curves a) than the computed wave.

6.3 *The internal velocity field*

The examples in Section 6.2 show that it has been possible to reproduce the surface variations recorded in the experiments down to very small details and over quite extended periods of time relative to the time scale of the important events. This can only be possible if the computational solution actually represents the whole flow pattern to a high degree of accuracy. Thus it will be possible to use the computational solution to analyze other properties of the flow (like the internal velocity field) than those actually measured in the experiments and to have a reasonable confidence in the correctness of such predictions.

We have computed the internal velocity field at 80-90 points (the exact number depending on the water level elevation) in the neighborhood of a 45° slope during runup of a *first-order* wave of $\frac{H}{d}$=0.457. To measure velocities in that detail in the physical experiments would be a tremendous task, whereas it only requires a limited extra effort computationally. Hence this example illustrates the usefulness of combining experiments and numerical computations.

The numerical procedure that computes the development of the wave motion in space and time (Sections 2 and 3), leaves us with both ϕ and $\frac{\partial\phi}{\partial n}$, known at all time steps. Therefore, the computation of the velocity at an internal point is a theoretically straight-forward evaluation of an integral. At an internal point $\mathbf{x}_o = (x_o, z_o)$, the velocity potential is given by,

$$\phi(\mathbf{x}_o) = \int_\Gamma [\frac{\partial\phi}{\partial n} G(\mathbf{x}, \mathbf{x}_o) - \phi \frac{\partial G(\mathbf{x}, \mathbf{x}_o)}{\partial n}] \, d\Gamma \tag{27}$$

Differenciation of this expression with respect to x_o and z_o yields,

$$u(\mathbf{x}_o) = \int_\Gamma [\frac{\partial\phi}{\partial n} \frac{\partial G(\mathbf{x}, \mathbf{x}_o)}{\partial x_o} - \phi \frac{\partial^2 G(\mathbf{x}, \mathbf{x}_o)}{\partial n \partial x_o}] \, d\Gamma \tag{28}$$

$$w(\mathbf{x}_o) = \int_\Gamma [\frac{\partial\phi}{\partial n} \frac{\partial G(\mathbf{x}, \mathbf{x}_o)}{\partial z_o} - \phi \frac{\partial^2 G(\mathbf{x}, \mathbf{x}_o)}{\partial n \partial z_o}] \, d\Gamma \tag{29}$$

The integration is again performed by Gaussian quadrature using eight to ten integration points per element, and all integrals are regular as long as the observation point $\mathbf{x}_o$, stays inside the domain. However if $\mathbf{x}_o$ is to close to the boundary, the integrand will vary so rapidly over the one or two elements closest to $\mathbf{x}_o$, that the accuracy even when using ten Gauss-points per element is insufficient. Therefore the computation points for the internal velocity field have been kept at a distance of about half an element length from the boundary (distance found sufficient for ensuring a good accuracy). This constraint can, of course, be

removed by a more accurate integration over the critical elements (like the so-called distance-adaptative integration).

In the computations described here, the number of nodes has been increased from 222 to 232 (of which 137 are on the surface and 19 are on the slope), in order to obtain a better resolution of the internal velocity field close to the slope. This measure also gives a slight improvement of the integration over the elements closest to the wedge at the tip of the runup where a similar problem occurs.

Figure 16a-f shows the velocity field at six different stages of the runup and reflection. Throughout the Figure, the same scale has been used for the velocities, as indicated by the arrow of length $\sqrt{gd}$ shown on part a.

When the first part of the wave reaches the slope, the motion gradually builds up. During this phase the flow pattern very much looks like that shown in part a of the Figure. The combination of the rising water level in the solitary wave and the upward twist of the flow along the slope makes the flow field look almost like the flow in a corner bounding a semi-infinite space.

Over the 1.68 time units between part a and b in Figure 16, the picture changes as the wave crest approaches the slope. The upward movement becomes more and more concentrated to the region closest to the shoreline and almost looks like a jet rushing up along the slope. This is even more pronounced in part c where the crest has almost reached the shoreline. Yet, immediately under the crest, which is still a clearly visible maximum of elevation, the velocities are horizontal and large as in a progressive wave. Similarly, behind the crest, the velocities are facing downward and decreasing in size.

Part d of Figure 16 shows the instant where the crest of the wave technically has reached the instantaneous intersection between surface and slope. There is still a jet-like up-rush of the tip of the wave here 0.83 time units later though more isolated and with smaller velocities than in part c. A stagnation point has developed near the toe of the slope as an indication of the reflection taking effect. In the next 0.90 time units from d to e, this stagnation point moves up along the slope so that more and more of the flow turns direction to downwards along the slope. However, even part e of Figure 16 does not yet represents the instant of maximum runup. That does not occur until at $t'(R_u) = 35.38$ (f). Clearly at this stage, the flow kinetic energy does not quite reach zero (like we observed on a vertical wall in Section 5.5). From this time on, however, the flow is outward going at all points until the lowest point in the down rush is reached. Hence, the tip of the wave is the very last point at which the velocity changes direction.

Figure 17a-d similarly shows the velocity field at 4 stages of the flow between the instant of maximum runup and that of the lowest computed position of the surface. A remarkably interesting feature is the combination of high velocities and large accelerations at the time of the lowest position (Fig. 17-d). The steep shoreward slope of the free surface in this non-distorted figure suggests horizontal accelerations close to one g.

The rapid retraction of the free surface has another implication, however. Had the slope been porous like a rubble mound structure, it is unlikely the water table inside the structure would have been able to follow the fast drop of the outside water surface. Consequently, onwards from the time of part c in Figure 17, there would be a strong outward directed pressure gradient on the armor units in the structure caused by the difference in water level inside and outside the slope. This would result in a high risk of units being pulled out of the

slope. The damage to rubble mound structures observed during experiments actually often occurs at this stage of the process.

6.4 *Comparison with the shallow water wave equations*

One of the questions that can be asked when looking at these results for highly nonlinear wave runup is: How well will the nonlinear shallow water (NSW) equations be able to describe this flow.

Those equations are the basis for Carrier & Greenspan (1958) solution for periodic waves on a steep slope and were used for a solitary wave by Synolakis (1987) (SY). It is of interest to know to which extent this simpler formulation describes the actual flow situation as computed here.

It is well known that the nonlinear Shallow water equations represent situations where the Ursell parameter $U = \frac{HL^2}{d^3}$ is much larger than unity. This means waves of large amplitude which are so long relative to the depth that the vertical accelerations can be neglected. Hence, the pressure is hydrostatic and, on a horizontal bottom, it follows implicitly that horizontal velocities are uniform over the entire depth.

In the present context, it is important to recall that if it is assumed that the pressure is hydrostatic and the horizontal velocities are uniform over depth, then the nonlinear shallow water equations can be shown to apply even on a steep slope. Therefore, the extent to which the solution to the exact equations computed here deviates from those ideal assumptions may indicate the degree of accuracy one can expect from the much simpler NSW approximation (when it comes to a Boussinesq approximation, a steep bottom slope changes the equations more significantly).

Velocities above the slope :

It is rather evident from the outset that on a steep slope the large horizontal velocities are closely associated with vertical velocities of the same order of magnitude. Therefore, vertical accelerations cannot be neglected. That implies nonhydrostatic pressure which will feed back and create horizontal velocities that are not uniform over depth. The horizontal velocity profiles along verticals can be inferred from Figures 16 and 17. Horizontal velocity profiles show variations almost invariably close to being linear with a nearly constant absolute shear. Thus, at places and times with high velocities, the relative difference between surface and bottom velocity may be seen to be only, at most, 70-75 % of the mean velocities which are the velocities that would be predicted by the NSW equations. Using a quadratic resistance law this means the forces on e.g. armor units on the slope would only be about half the forces predicted by the NSW equations if no other changes were effective.

Pressure on the slope :

The pressure variation along the slope is shown in Figure 18a and b. The abscissa is the vertical dimensionless coordinate along the slope. The ordinate $\frac{p_T}{p_H}$ is given by,

$$\frac{p_T}{p_H} = \frac{-\rho(\frac{\partial \phi}{\partial t} + \frac{1}{2}\mid \nabla \phi \mid^2 + gz)}{\rho g \zeta} \tag{30}$$

where p_T is the total pressure computed from the Bernoulli equation and ζ is the vertical distance between the free surface and the point on the slope. Hence, the ordinate +1 corre-

θ	$\frac{H_i}{d}$	BEM	SY(appr.)	SY(intg.)	Exper.	by
70°	0.259	0.580	(0.316)	0.524	0.568	LVN
70°	0.437	1.062	(0.607)	1.142	1.071	LVN
45°	0.269	0.674	(0.546)	0.644	0.672	LVN
45°	0.457	1.257	(1.064)	1.194	1.294	LVN
2.88°	0.019	0.081	0.089		0.077	SY
2.88°	0.040	—	0.226		0.156	SY

Table 7: Results from Svendsen & Grilli (1989) : Maximum runup of *first-order* solitary waves on a slope θ. $\frac{H_i}{d}$ is the height of the incident wave (at $x = 20d$ in the BEM computations) and BEM are the computed maximum runup $\frac{R_u}{d}$ (equivalent to those in Table 6). SY(appr.) and SY(intg.) are the runups from Synolakis (1987) approximate and integral formula respectively, and "Exper." are the experimental runups by Losada, *et al.* (1986) (LVN) and Synolakis (1987) (SY). The parenthesis mean that, for such slopes, the approximate formula is not quite applicable.

sponds to the actual pressure being equal to the weight of the water column above the point ("hydrostatic pressure" p_H).

While the pressure in the runup phase (part a) differs somewhat from the hydrostatic, it generally stays within 1.1 and 0.7 times that value, the lowest values occuring near the surface almost at the time of runup. Part b shows the pressure during down-rush. During the first part of that phase the pattern at the time of runup essentially propagates down the slope. This might be expected because at that point, the tip of the runup is rather isolated from the rest of the water body and just moving under the action of gravity so that the pressure reflects the gravity component $\frac{g}{\sqrt{2}}$ normal to the surface (curve a and next in Figure 18b). When the surface slope changes sign (Figure 17b-c), the flow in the down-rush starts decelerating which creates pressures above hydrostatic, as seen from curves b and c. This is even more pronounced in curve d where the pressure is above hydrostatic all along the slope.

Thus, as could be expected from the outline above of the nature of the flow on a steep slope, also the pressure deviates quite appreciably from the hydrostatic pressure assumed in the NSW equations.

One issue, important for a complete comparison of the two methods, has not been investigated here. That is the effect the deviations from assumed velocity and pressure conditions have on the actual development of the wave motion on the slope. The velocities and pressures have only been related to the values the NSW equations would have predicted had the surface variation and mean velocity been as computed here.

Runup :

Synolakis (1987) developed an analytic solution for the NSW equations analogous to the solution by Carrier & Greenspan (1958), but for a slope rising from finite constant depth d and a (*first-order*) solitary incident wave. He also gave two different expressions for the runup height $\frac{R_u}{d}$ on the slope : one an explicit approximate formula only valid for gentle

slopes, the other an integral equation. A comparison of his results with the BEM method has been reported by Svendsen & Grilli (1989) (S&G) (using an earlier, less accurate version of the model) and some of the results are reproduced in Table 7. For the steeper slopes (45° and 70°), Synolakis (1989b) has supplied the figures for the runup calculated by the integral formula. Runups from the two methods are seen to compare quite well with the LVN experiments for the waves considered. Table 7 also confirms that SY's approximate formula does give less accurate runup results for the steeper slopes. The BEM method may also be used for the situations of runup on more gentle slopes, as studied by SY. For a 2.88° slope, S&G find that the two methods give runup heights of the same order of magnitude. For a wave of initial height $\frac{H}{d}$=0.019, the approximate method of SY yields $\frac{R_u}{d}$=0.089 against 0.081 found by the BEM. SY's experiments showed $\frac{R_u}{d}$=0.077. A second wave initially twice as high (0.040) was studied by SY on the same slope, but turned out to break before maximum runup in the BEM computations.

6.5 *Remark on the friction*

It may also be worthwhile briefly to comment on the fact that the method is unable to include frictional effects in its present form. Friction will occur along the solid boundary at the bottom and the slope where a boundary layer will develop. This will clearly dissipate some of the wave energy, and if longer distances of propagation are considered, the cumulative effect may be quite important for which wave height actually reaches the slope [6]. As usual, however, locally friction has only a negligible effect on the wave motion. In particular, on a smooth slope as considered here, the influence of friction on the highly inertia dominated runup and reflection process must be expected to be of virtually no consequence. Only at the uppermost tip of the runup, would some frictional effect be expected. The problem was studied by Packwood & Peregrine (1981).

7 Conclusions

The computations described here have been made with a version of the Boundary Integral Equation Method which does not apply complex variables and does not assume the waves are periodic in space. It turns out that sawtooth instability does not occur, and that both energy and volume inside the computational region are controled sufficiently well to not making it necessary to carry out artificial adjustments during the computations as has been necessary in, e.g., one of the computations reported by Dold & Peregrine (1986).

Solitary waves have been generated by two independent methods. *Exact* solitary waves by Tanaka's (1986) method and *first-order* waves by a piston wavemaker using Goring's (1978) approach. Both wave types are used for examining the runup and reflection from a vertical wall and the *first-order* waves reproduce as closely as possible the conditions in the experiments by Losada, *et al.* (1986).

[6] The way the comparisons with experiments are set up here, the effect is virtually nil, since the initial wave height $\frac{H_i}{d}$ used as reference for the computations is measured at quite a short distance from the slope ($13.3d$), which eliminates the effect friction has during most of the propagation in the much longer physical wave tank ($L \simeq 160d$).

The BEM computations have been compared with a 3rd order analytic solution by Su & Mirie (1980) (S&M) and a Fourier solution by Fenton & Rienecker (1982) (F&R) for the reflection from a vertical wall. The results show that up to $\frac{H}{d}$=0.4, all three methods give similar predictions for the runup and for the pressure force on the wall (with slightly lower results for the *first-order* waves, because of the energy transmitted to their oscillatory tail). For higher waves, higher order contributions are becoming important and our results predict somewhat larger runup and force than did the previous investigations. For large values of $\frac{H}{d}$it is also found that the variation of the pressure force on the wall with respect to time exhibits double maxima.

Results for the rundown, reflected wave, celerity, phase shift and energy partition of an *exact* solitary wave of incident height $\frac{H}{d}$=0.5 have been compared with a 5th order analytic solution by Byatt-Smith (1988) (B-S). Most of the findings of the latter study are quite well reproduced quantitatively. An oscillatory tail is created by the reflection process and, due to the energy transmitted to the tail, the wave amplitude decreases slightly after reflection (9.3%). Rundown values (negative elevations) of the same order are observed at the wall. The celerity of the (transient) reflected wave is found to increase slightly (0.5%), as also computed by F&R (who , however, got a much larger increase of 6.6%, and also did not obtain an oscillatory tail after reflection) and observed experimentally by Seabra-Santos (1985). Instantaneous time and space phase lags during the reflection process are also found somewhat smaller than predicted by S&M and F&R. Although the amplitude recovers partly, it will not return to its initial value because of the energy transfered to the tail (against B-S statement) and, accordingly, the celerity of the reflected wave will eventually become slightly smaller, as it approaches permanent form. The kinetic energy is found to be minimum (but not quite zero) slightly before the time of the runup. Kinetic energy also drops after reflection (0.54%), with respect to its initial value, and only part of this decrease is recovered on a longer term basis.

Reflection from steep slopes (45° and 70°) has also been examined for solitary waves generated by a piston wavemaker the same way as in laboratory experiments by Losada, *et al.* (1986). Comparison with the measurements shows that phenomena such as generation, propagation and runup on a steep slope of large amplitude waves can be accurately predicted by this method. Even small scale oscillations in the experiments (like the oscillatory tail after reflection) are reproduced quite accurately. Motivated by the accuracy of the computations the method has been used to analyze flow properties such as velocity and pressure fields that have not been measured during the experiments. Analysis of the water particle velocities above a 45° slope during runup-rundown shows that horizontal velocities are significantly non-uniform over the depth (variation of 25-30%) and that, accordingly, important non-hydrostatic pressures are generated. This invalidates the assumptions underlying the Nonlinear Shallow Water equations and makes their use questionable in these situations. The maximum runup, however, is found to compare reasonably well with the results obtained by Synolakis (1987) using those approximate equations.

Aknowledgments

The authors greatfully acknowledge the assitance from M.A. Losada in extracting the experimental results from the original data. The authors would also like to thank D.H.

Peregrine and M. Cooker for having provided them with software which generates exact solitary wave profiles according to Tanaka (1986), and C.E. Synolakis for helpful comments and numerical results.

8 Bibliography

BREBBIA, C.A. 1978 *The Boundary Element Method for Engineers.* John Wiley & Sons, U.K..

BYATT-SMITH, J.G.B. 1988 The Reflection of a Solitary Wave by a Vertical Wall. *J. Fluid Mech.* **197**, 503-521.

CAMFIELD, F.E. & STREET, R.L. 1969 Shoaling of Solitary Waves on Small Slopes. *J. Waterways and Harbor Div.* **95** (WW1), 1-22.

CARRIER, G.F. 1966 Gravity Waves on Water of Variable Depth. *J. Fluid Mech.* **24** (4), 641-659.

CARRIER, G.F. & GREENSPAN, H.P. 1958 Water Waves of Finite Amplitude on a Sloping Beach. *J. Fluid Mech.* **4** (1), 97-110.

COOKER, M. 1989 Personal communication.

DOLD, J.W. & PEREGRINE, D.H. 1986 An Efficient Boundary Integral Method for Steep Unsteady water Waves. *Numerical methods for Fluid Dynamics II* (ed. K.W. Morton & M.J. Baines), pp. 671-679. Clarendon Press, Oxford.

DOMMERMUTH, D.G. & YUE, D.K.P. 1987 Numerical Simulation of Nonlinear Axisymmetric Flows with a Free Surface. *J. Fluid Mech.* **178**, 195-219.

FENTON, J.D. & RIENECKER, M.M. 1982 A Fourier Method for Solving Nonlinear Water-Wave Problems : Application to Solitary-Wave Interactions. *J. Fluid Mech.* **118**, 411-443.

GARDNER, C.S., GREENE, J.M., KRUSKAL, M.D. & MIURA, R.M. 1967 Method for Solving the Korteweg-de Vries Equation. *Physical Revue Letters* **19**, (19), 1095-1097.

GORING D.G. 1978 Tsunamis - The Propagation of Long Waves onto a Shelf. *W.M. Keck Laboratory of Hydraulics and Water Ressources, California Institute of Technology, Report No.* **KH-R-38.**

GREENHOW, M. & LIN, W.M. 1985 Numerical Simulation of Nonlinear Free Surface Flows Generated by Wedge Entry and Wave-maker Motions. In *Proc. 4th Intl. Conf. on Num. Ship Hydro., Washington D.C., September 1985.*

GRILLI, S., SKOURUP, J. & SVENDSEN, I.A. 1988 The Modelling of Highly Nonlinear Waves : A Step Toward the Numerical Wave Tank. Invited paper in *Proc. 10th Intl. Conf. on Boundary Elements, Southampton, England, September 1988,* Vol. 1 (ed. C.A. Brebbia), pp. 549-564. Computational Mechanics Publication. Springer-Verlag, Berlin.

GRILLI, S., SKOURUP, J. & SVENDSEN, I.A. 1989 An Efficient Boundary Element Method for Nonlinear Water Waves. *Engineering Analysis with Boundary Elements,* **6** (2), 97-107.

GRILLI, S. & SVENDSEN, I.A. 1989a Computation of Nonlinear Wave Kinematics during Propagation and Runup on a Slope. In *Water Wave Kinematics (Proc. NATO-ARW, Molde, Norway, May 89),* 26pps. Klüwer Academic Publishers.

GRILLI, S. & SVENDSEN, I.A. 1989b The Modelling of Highly Nonlinear Waves : Some Improvements to the Numerical Wave Tank. In *Advances in Boundary Elements (Proc. 11th Intl. Conf. on Boundary Elements, Cambridge-Massachusetts, USA, August 89),* Vol. 2 (ed. C.A. Brebbia & J.J. Connor), pp. 269-281. Computational Mechanics Publication. Springer-Verlag, Berlin.

HAMMACK, J.L. & SEGUR, H. 1974 The Korteweg-de Vries Equation and Water Waves. Part 2. Comparison with Experiments. *J. Fluid Mech.* **65** (2), 289-314.

ISAACSON, M. de St. Q. 1982 Nonlinear Effects on Fixed and Floating Bodies. *J. Fluid Mech.* **120**, 267-281.

KIM, S.K., LIU, P.L.-F. & LIGGETT, J.A. 1983 Boundary integral Equation Solutions for Solitary Wave Generation Propagation and Run-up. *Coastal Engineering* **7**, 299-317.

KLOPMAN, G. 1988 Numerical Simulation of Gravity Wave Motion on Steep slopes. *Delft Hydraulics Report No.* **H195.**

LONGUET-HIGGINS, M.S. & COKELET, E.D. 1976 The Deformation of Steep Surface Waves on Water - I. A Numerical Method of Computation. *Proc. R. Soc. Lond.* **A350**, 1-26.

LOSADA, M.A., VIDAL, C. & NUNEZ, J. 1986 Sobre El Comportamiento de Ondas Propagádose por Perfiles de Playa en Barra y Diques Sumergidos. *Dirección General de Puertos y Costas Programa de Clima Maritimo. Universidad de Cantábria. Publicación No.* **16.**

MAXWORTHY, T. 1976 Experiments on Collisions Between Solitary Waves. *J. Fluid Mech.* 76 (1), 177-185.

MIRIE R.M. & SU C.H. 1982 Collisions Between Two Solitary Waves. Part 2. A Numerical Study. *J. Fluid Mech.* **115**, 475-492.

NAGAI, S. 1969 Pressures of Standing Waves on Vertical Wall. *J. Waterways and Harbor Div.* 95 (WW1), 53-76.

NAKAYAMA, T. 1983 Boundary Element Analysis of Nonlinear Water Wave Problems. *Intl. J. Numer. Meth. Engng.* **19**, 953-970.

NAKAYAMA, T. 1988 A Stable and Fast Method for the Numerical Analysis of Unsteady Free Surface Motions. In *Proc. Intl. Conf. on Comp. Meth. in Flow Analysis, Okayama, Japan, September 1988.*

NAM SEO, S. 1988 Time-Dependent Highly Nonlinear Waves (Ph.D. Dissertation). *Civil Engineering Department, University of Delaware, U.S.A.* .

OIKAWA, M. & YAJIMA, N. 1973 Interaction of Solitary Waves - A Perturbation Approach to Nonlinear Systems. *J. Phys. Soc. Japan* **34**, 1093-1099.

PACKWOOD, A.R. & PEREGRINE, D.H. 1981 Surf and Runup on Beaches : Models of Viscous Effects. *School of Mathematics, University of Bristol, Report No.* **AM-81-07.**

PEDERSEN, G. & GJEVIK, B. 1983 Run-up of Solitary Waves *J. Fluid Mech.* **135**, 283-299.

ROMATE, J.E. 1989 The Numerical Simulation of Nonlinear Gravity Waves in Three Dimensions using a Higher Order Panel Method. *Ph.D. Dissertation. Department of Applied Mathematics, University of Twente, The Netherland.*

SEABRA-SANTOS, F.J. 1985 Contribution à l'étude des ondes de gravité bidimensionnelles en eau peu profonde (Thèse de Doctorat d'Etat). *Université scientifique et Médicale et Institut Polytechnique de Grenoble.*

SU, C.H. & MIRIE, R.M. 1980 On Head-on Collisions between two Solitary Waves. *J. Fluid Mech.* 98 509-525.

SU, C.H. & GARDNER, C.S. 1969 Korteweg-de Vries Equation and Generalizations. III. Derivation of the Korteweg-de Vries Equation and Burgers Equation. *J. Math. Phys.* 10 536-539.

SUGIMOTO, N., KUSAKA, Y. & KAKUTANI, T. 1987 Reflection of a Shallow-water Soliton. Part 2. Numerical Evaluation. *J. Fluid Mech.* **178**, 99-117.

SVENDSEN, I.A. 1971 Mixed Boundary Value Problem for Laplace's Equation in Domain of Arbitrary Shape. *Technical University of Denmark report No.* **23** 33-38.

SVENDSEN, I.A. & GRILLI, S. 1989 Nonlinear Waves on Steep Slopes. To appear in *J. Coastal Res.* (Spring 1990).

SVENDSEN, I.A. & JUSTESEN, P. 1984 Forces on Slender Cylinders from Very High and Spilling Breakers. In *Proc. Symp. on Description and Modelling of Directional Seas,* paper No. D-7, 16 pps. Technical University of Denmark.

SYNOLAKIS, C.E. 1987 The Runup of Solitary Waves. *J. Fluid Mech.* **185,** 523-545.

SYNOLAKIS, C.E. 1989a On the Generation of Long Waves in the Laboratory. Submitted to *J. Waterways, Harbors and Coastal Engng.*

SYNOLAKIS, C.E. 1989b Personal communication.

TANAKA, M. 1986 The Stability of Solitary Waves. *Phys. Fluids* **29** (3), 650-655.

VINJE, T. & BREVIG, P. 1981 Numerical Simulation of Breaking Waves. *Adv. Water Resources* **4,** 77-82.

List of Figure captions

Fig. 1: Sketch of the region used in the numerical computations in Section 6. Definition of geometrical parameters.

Fig. 2a: Comparison between *exact* (——) (as in Tanaka 1986) and *first-order* (- - -) (Boussinesq (23)) solitary wave profiles for $\frac{H}{d}$=0.8.

Fig. 2b: Surface profile $\eta(x)$ for *first-order* solitary waves of height $\frac{H_i}{d} = 0.2$ through 0.5. Each wave is shown at the moment the crest passes $x' = 20$ (20 water depth d from the wave generator). The propagation times t' are : $\frac{H_i}{d} = 0.2 : 27.27$, $0.3 : 24.64$, $0.4 : 22.92$, $0.5 : 21.65$.

Fig. 3a: Comparison between two *first-order* solitary wave surface profiles generated at $x' = 66.7$ (- - -) and $x' = 0$ (——) respectively (i.e. after propagating $20d$ and $86.7d$). To be of the same height $\frac{H_i}{d} = 0.25$ at $x' = 86.7$, the two waves were generated with slightly different amplitude.

Fig. 3b: Comparison between the second wave of Fig. 3a and an *exact* solitary wave of same height, at the same position (the wall is at $x' = 100$).

Fig. 4: Development of crest elevation for the two *first-order* waves compared in Fig. 3a.

Fig. 5a: Development of the total energy e_t in the computations during reflection from a vertical wall, of an *exact* wave of incident wave height $\frac{H}{d}$= 0.5. The Figure shows only small changes during horizontal propagation and more important changes during runup at time of very rapid motions. The $\frac{\Delta e_t}{e_t}$ is proportional to $(\Delta t)^3$ for a given spatial BEM discretization. The initial total energy is e_{to}=0.615490.

Fig. 5b: Change in water volume of the wave m for the same wave and over the same period of time as in Fig. 5a. The initial wave volume is m_o=1.791117.

Fig. 6: Envelope for maximum amplitude $\frac{H}{d}$during reflection from a vertical wall of the two *first-order* waves shown in Fig. 3a and 4. The wall is at $x' = 100$ and the vertical line A-B shows the height of the runup. The lowest of the two sets of curves represents the crest elevations after runup.

Fig. 7: Maximum runup $\frac{R_u}{d}$ for reflection from a vertical wall versus the value of the incident wave height $\frac{H}{d}$(the incident *first-order* wave amplitude is defined at $x' = 20$ ($13.3d$) in front of the wall as in Fig. 2b). (——) Su & Mirie (1980) 3rd order analytical results, (□) Fenton & Rienecker (1982) Fourier Method results, (o) present BEM results for the *first-order* waves, (◇) present BEM results for the *exact* waves, (- - -) cubic spline fitting to these last results and (– – –) linear relationship $\frac{R_u}{d} = 2\frac{H}{d}$.

Fig. 8a: Lowest point of water surface $\frac{R_d}{d}$ (rundown) for reflection from a vertical wall versus the incident wave height $\frac{H}{d}$defined as in Fig. 7. (o) Present BEM results for the *first-order* waves and (——) cubic spline fitting to the results; (◇) present BEM results for the *exact* waves and (- - -) cubic spline fitting to the results. Notice that all elevations are negative, and the scale is very different from that in Fig. 7.

Fig. 8b: Reflected wave profiles after reflection of *exact* solitary waves from a vertical wall. Incident wave height $\frac{H}{d}$= (a) : 0.2, (b) : 0.3, (c) : 0.4, (d) : 0.5. Notice the increasingly more developed oscillatory tail from (a) to (d). One has the corresponding time t' = (a) : 32.31, (b) : 27.58, (c) : 26.40, (d) : 29.98.

Fig. 9a: (——) Reflected solitary wave (*exact* wave, at $t' = 23.53$ or $\tau_2 \simeq 3$) for an incident wave amplitude of $\frac{H}{d}$=0.5, compared with the incident wave (- - -) at the same location x'_o=14.

Fig. 9b: (——) Amplitude $\frac{H}{d}$ of the reflected *exact* solitary wave of Fig. 9a (incident wave $\frac{H}{d}$=0.5), as a function of time t' from time t'_2=13.58, compared with the 5th order analytic solution of Byatt-Smith (1988) (- - -). The time of rundown $t'(R_d)$=16.18 is also marked on the Figure.

Fig. 9c: (——) Deviation of the reflected wave η' of Fig. 9a from the incident wave $\eta'_o = \eta'(x', t'_o)$ (oscillatory tail), compared with the 5th order analytic solution of Byatt-Smith (1988) (- - -).

Fig. 9d: Same as in Fig. 9c but for a later time $t' = 29.98$ or $\tau_2 \simeq 5$, at x'_o=6.19. Notice this also corresponds to the curve (d) of Fig. 8b.

Fig. 10a: (——) Phase diagram for the same wave as in Fig. 9, i.e. the relationship (x', t') for the point of maximum amplitude on the free surface. Notice the reflection occurs at $x' = 28$ (vertical wall location) and the maximum runup is at $t'(R_u) = 12.05$. (- - -) are straight lines fitted (LSM) to the data for $x' < 20$ whose slope $\frac{dx'}{dt'}$ gives the average incident and reflected wave celerities $(\overline{c'_i}, \overline{c'_r})$, one finds : $\overline{c'_i} = 1.2168$ and $\overline{c'_r} = 1.2226$.

Fig. 10b: Closer view on Fig. 10a. One gets a temporal phase lag $\Delta t' = 0.627$ (B-C) and a spatial phase lag $\Delta x' = 0.763$ (E-C). Notice B-F is a line symmetric to $\overline{c'_i}$.

Fig. 11a: Change in kinetic energy e_k and in potential energy e_p during reflection from a vertical wall, for the same wave as in Fig. 8-10. Notice the kinetic energy never quite reaches zero (e_k^{min}=0.00259, or 0.786% e_{ko}), and the minimum occurs slightly before the instant of maximum runup ($\Delta^{Ru}t'$=0.200). The initial kinetic energy is e_{ko}=0.329923 and the initial potential energy is e_{po}=0.285567.

Fig. 11b: Closer view on Fig. 11a. The decrease in kinetic energy after rundown Δe_k at $t'(R_d)$ is calculated at A, equal to 0.00179 (0.543% e_{ko}). It eventually decreases down to 0.384% e_{ko} at t'=29.98.

Fig. 12: (a) Maximum dimensionless pressure force F_x^{max} and : (b) moment with respect to the bottom M_b^{max}, for the same results as in Fig. 6.

Fig. 13a: Development in time of total dimensionless pressure force F_x on a vertical wall during reflection of an *exact* solitary wave. $\frac{H}{d}$ = (a) : 0.2, (b) : 0.3, (c) : 0.4, (d) : 0.5, (e) : 0.55, (f) : 0.6. Notice the double maximum for $\frac{H}{d}$ greater than 0.4.

Fig. 13b: Surface elevation at the wall η', pressure force F_x and moment M_b as a function of time for the same wave as in Fig. 9-11.

Fig. 14a: Comparison between computations (——) and measurements (- - -) by Losada, *et al.* (1986) for reflection from a 45° slope, $\frac{H_i}{d}$= 0.269.

(a) Instant of maximum runup ($t' = 38.44$ in computations)

(b) $t' = 41.76$

(c) Instant of lowest position of water surface ($t' = 42.20$, computations and experiments)

(d) $t' = 51.92$ (computations and experiments)

Fig. 14b: Same as Fig. 14a : 45° slope, $\frac{H_i}{d}$= 0.457.

(a) Instant of maximum runup ($t' = 35.38$ in computations)

(b) Instant of last computed position of the water surface ($t' = 37.93$)(backward breaking occured after that time)

(c) Instant of lowest position of water surface in experiments ($t' = 38.90$) (backward breaking

was observed around that time)
(d) $t' = 52.50$
Fig. 15a: Same as Fig. 14a : 70° slope, $\frac{H_i}{d} = 0.259$.
(a) Wave profile somewhat before maximum runup ($t' = 31.60$, computations and experiments)
(b) Instant of maximum runup ($t' = 38.20$ in computations)
(c) Instant of lowest position of water surface in computations ($t' = 42.56$)
(d) Instant of lowest position of water surface in the experiments ($t' = 42.83$)
(e) Reflected wave $\frac{H_r}{d} = 0.244$ at $x' = 20$ ($t' = 50.00$ in the computations, $t' = 49.85$ in the experiments).
Fig. 15b: Same as Fig. 14a : 70° slope, $\frac{H_i}{d} = 0.437$.
(a) Wave profile somewhat before maximum runup ($t' = 27.90$, computations and experiments)
(b) Instant of maximum runup ($t' = 34.58$ in computations)
(c) Instant of lowest position of water surface ($t' = 38.10$, computations and experiments)
(d) Reflected wave $\frac{H_r}{d} = 0.376$ at $x' = 20$ ($t' = 45.50$ in the computations, $t' = 45.24$ in the experiments).
Fig. 16a-f: The internal velocity field during runup of a *first-order* solitary wave with $\frac{H_i}{d} = 0.457$ on a 45° slope, at time t' = (a) : 30.38, (b) : 32.05, (c) : 33.15, (d) : 33.98, (e) : 34.88, (f) : 35.38. The bar in Fig 16a indicates length of arrow representing a velocity of $\sqrt{gd}$. The details of the figures are discussed in the text.
Fig. 17a-f: Same as Fig. 16 but for the rush-down phase, at time t' = (a) : 36.13, (b) : 37.25, (c) : 37.79, (d) : 37.93.
Fig. 18a: Pressure distribution along the slope during runup of the same wave and for the same times (for curves (a) to (f)) as in Fig. 16. The total pressure p_T is made dimensionless by division by the hydrostatic pressure p_H of the instantaneous water surface vertically above the considered point.
Fig. 18b: Same as Fig. 18a but for the rush-down phase (as in Fig. 17 plus one extra curve between (a) and (b) at $t' = 36.73$).

Figure 1

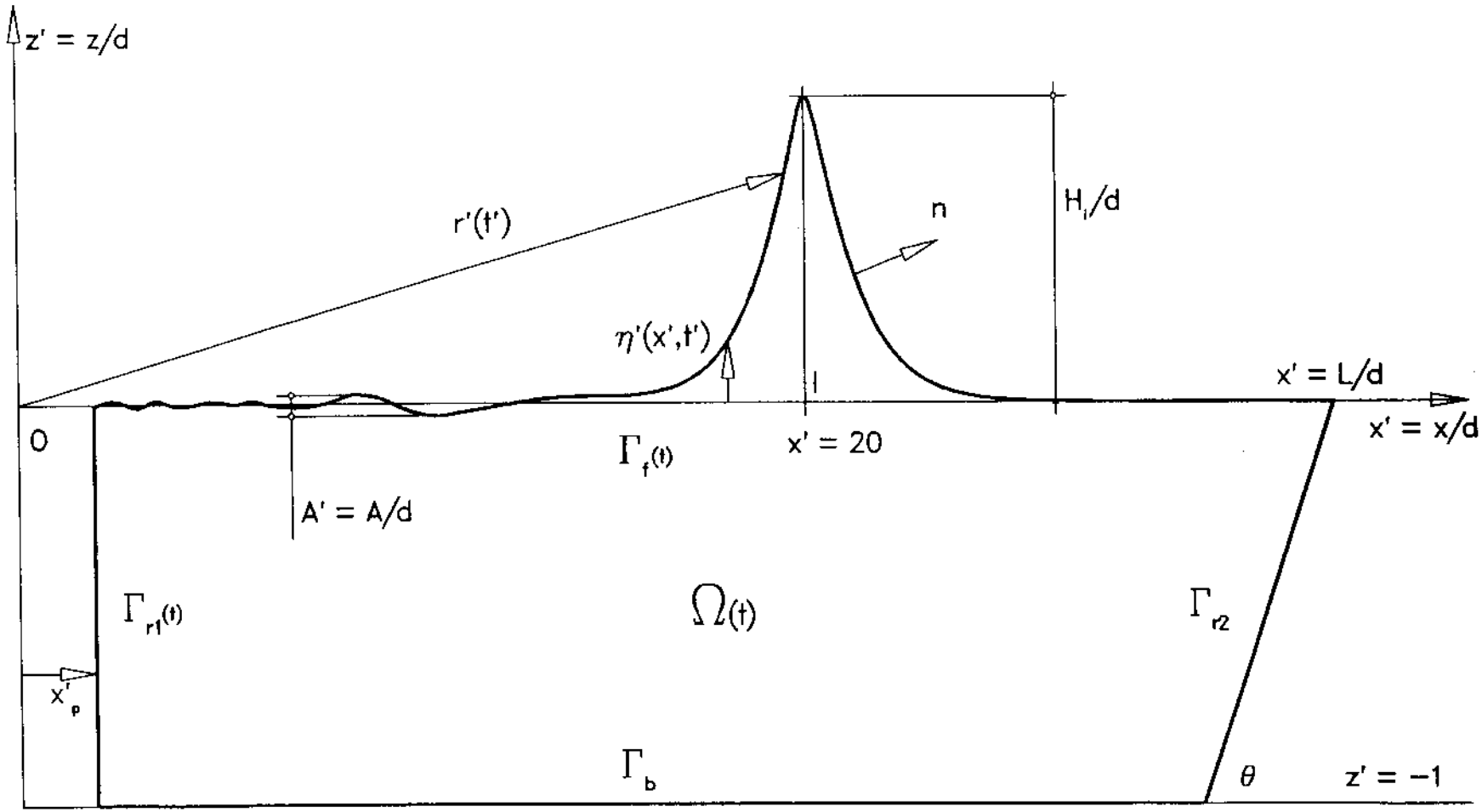

Fig. 2a: 1st Order Solitary Wave Generation

Comparison with an exact wave : H/d=0.83

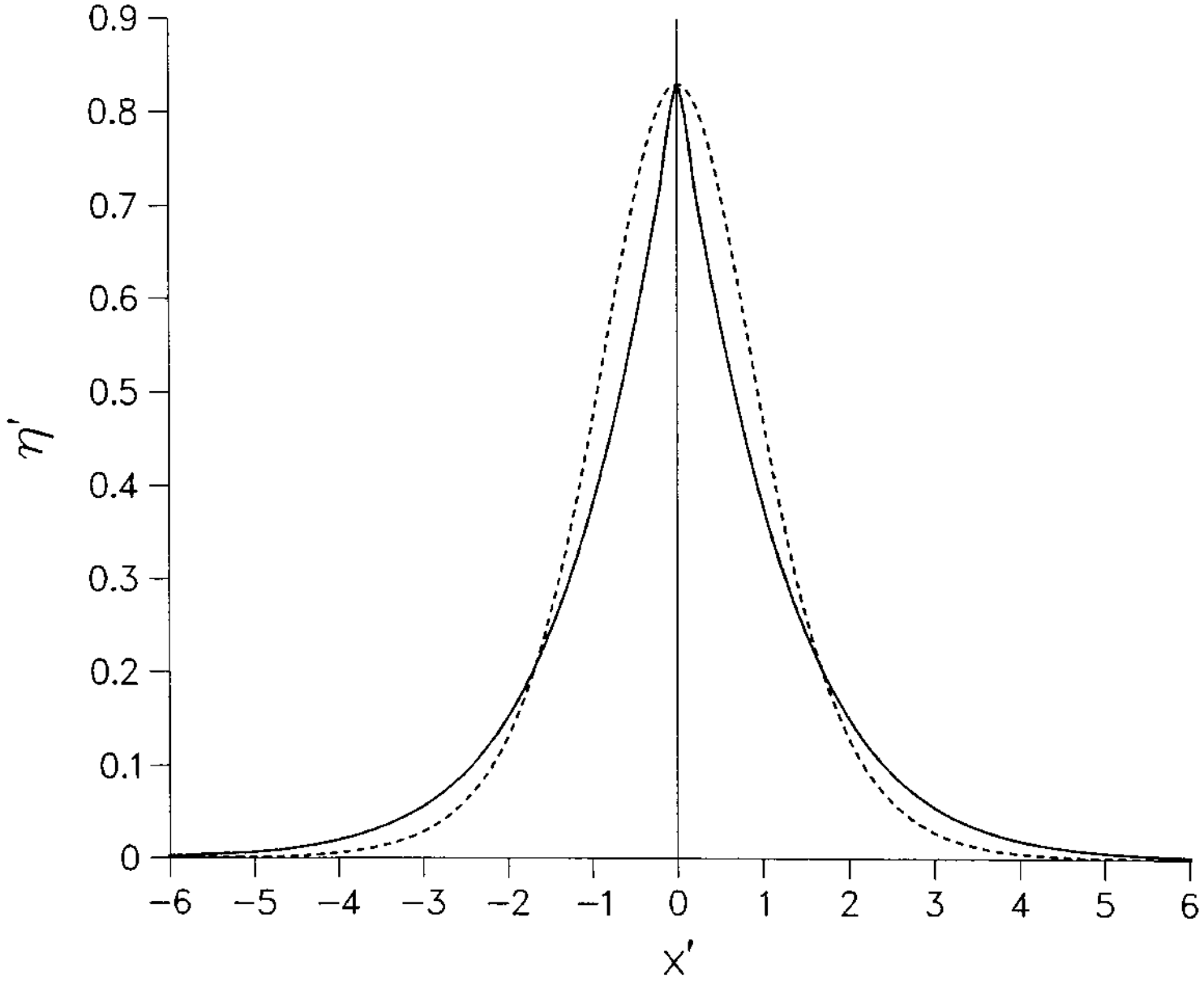

Fig. 2b: 1st Order Solitary Wave Generation

Incident Wave, Hi/d = 0.2 to 0.5

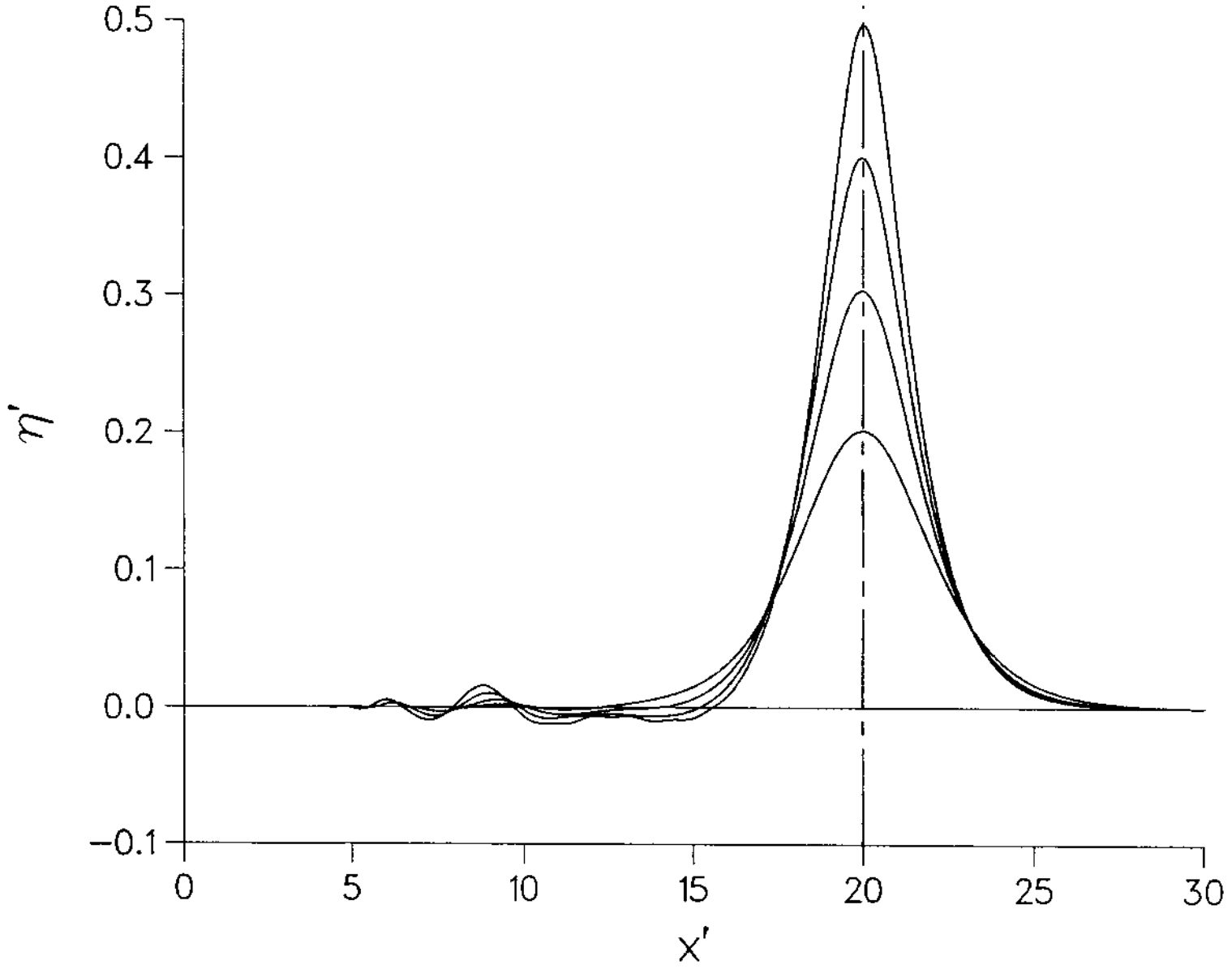

Fig. 3a: 1st Order Solitary Wave Generation

Comparison Of Wave Elevation For H/d=0.25 at x′=86.7

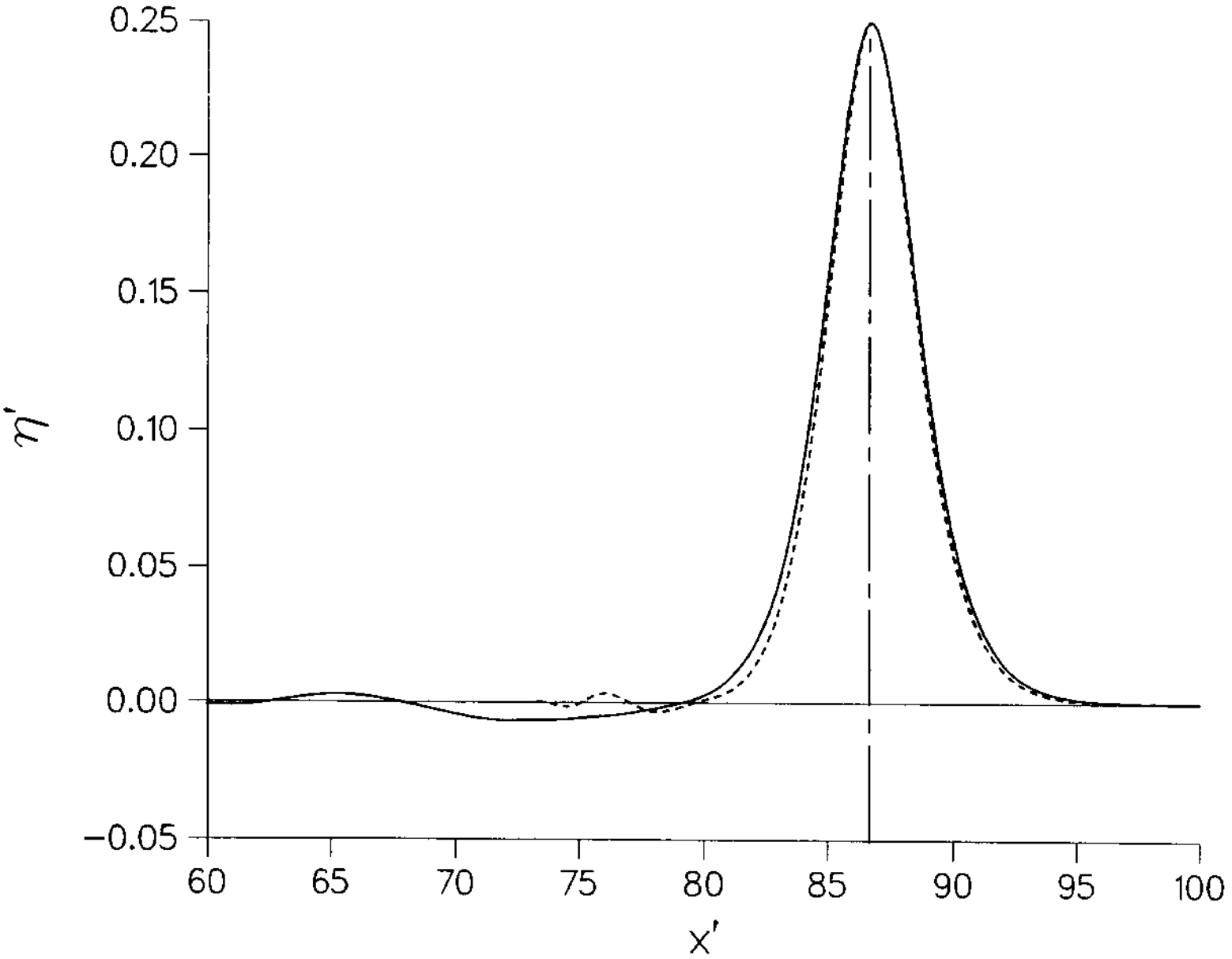

Fig. 3b: 1st Order Solitary Wave Generation

Comparison With an exact wave : H/d=0.25 at x′=86.7

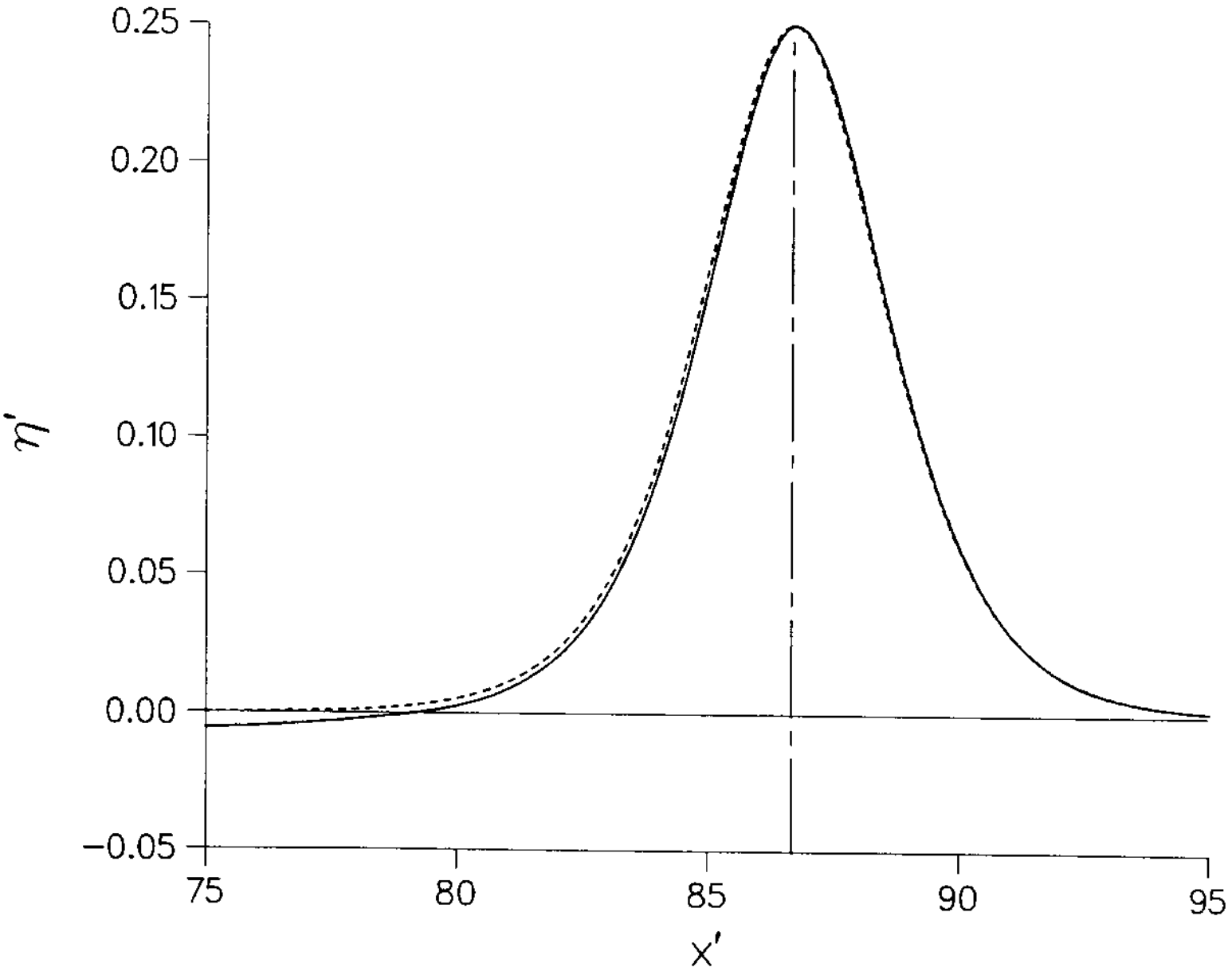

Fig 4: 1st Order Solitary Wave Generation

Amplitude Decrease : Hi/d = 0.25

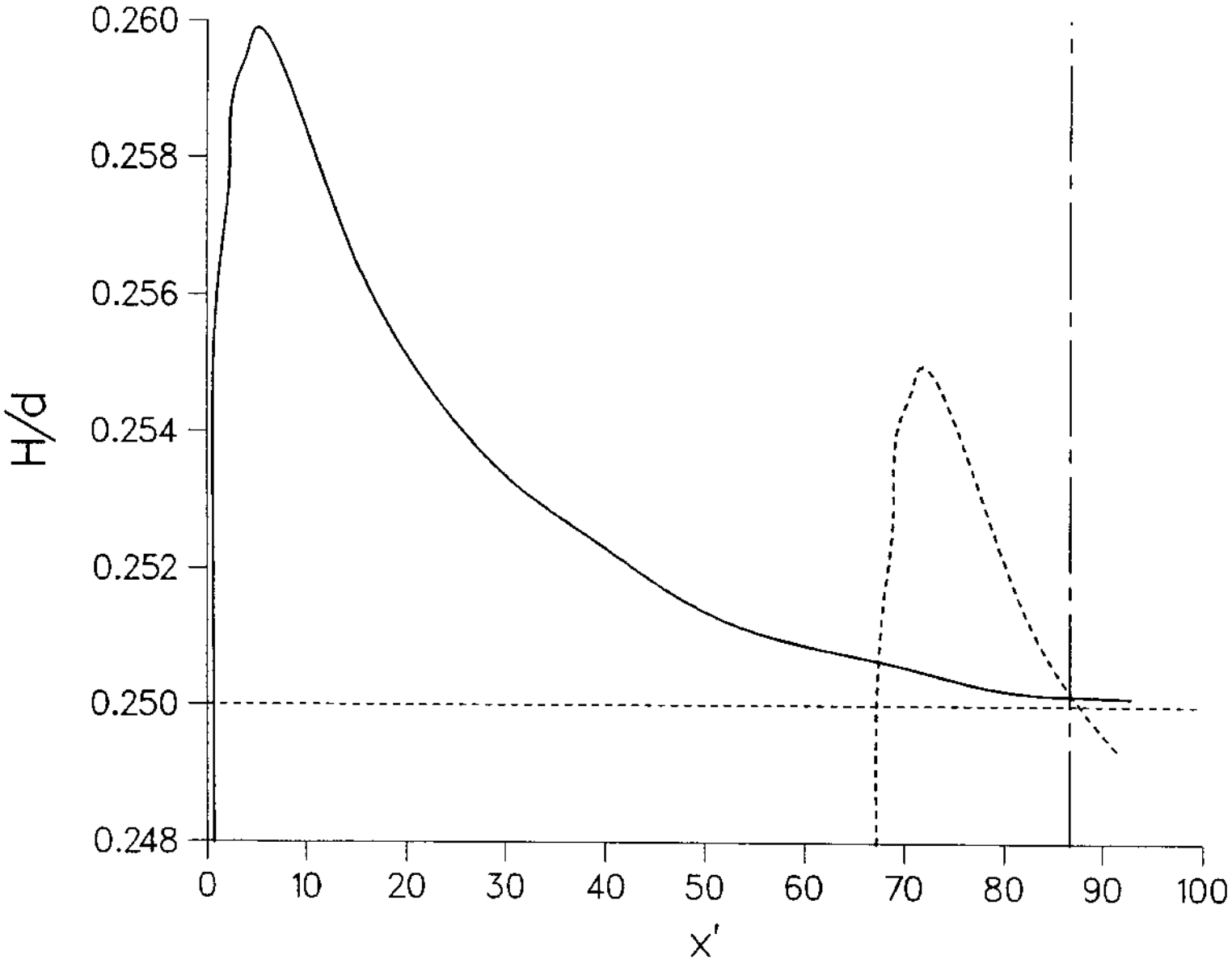

Fig. 5a: Reflection On A Vertical Wall

Total Energy, H/d=0.50, dt=0.04-0.01, dx/d=0.25

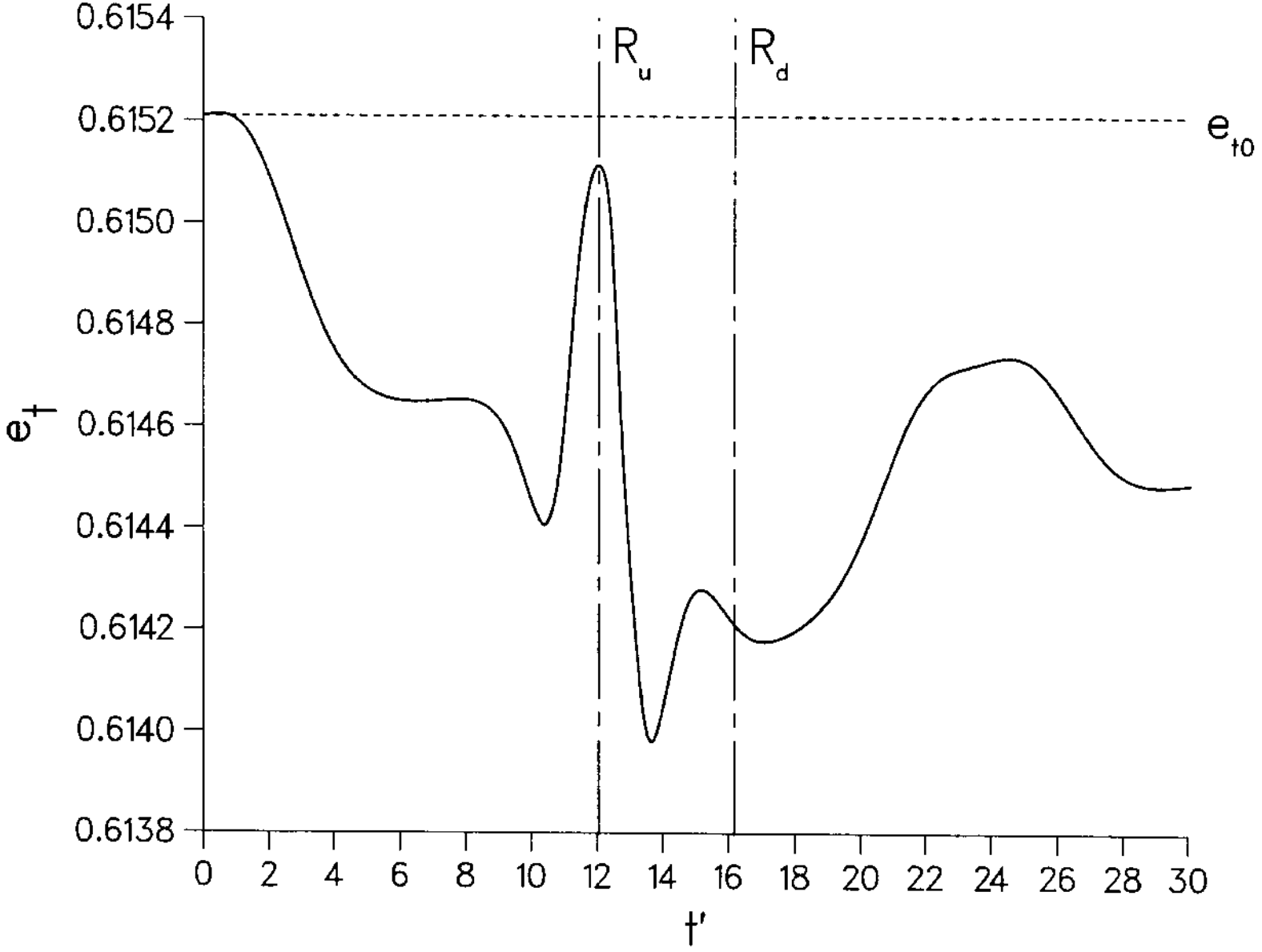

Fig. 5b: Reflection On A Vertical Wall

Volume Change, H/d=0.50, dt=0.04-0.01, dx/d=0.25

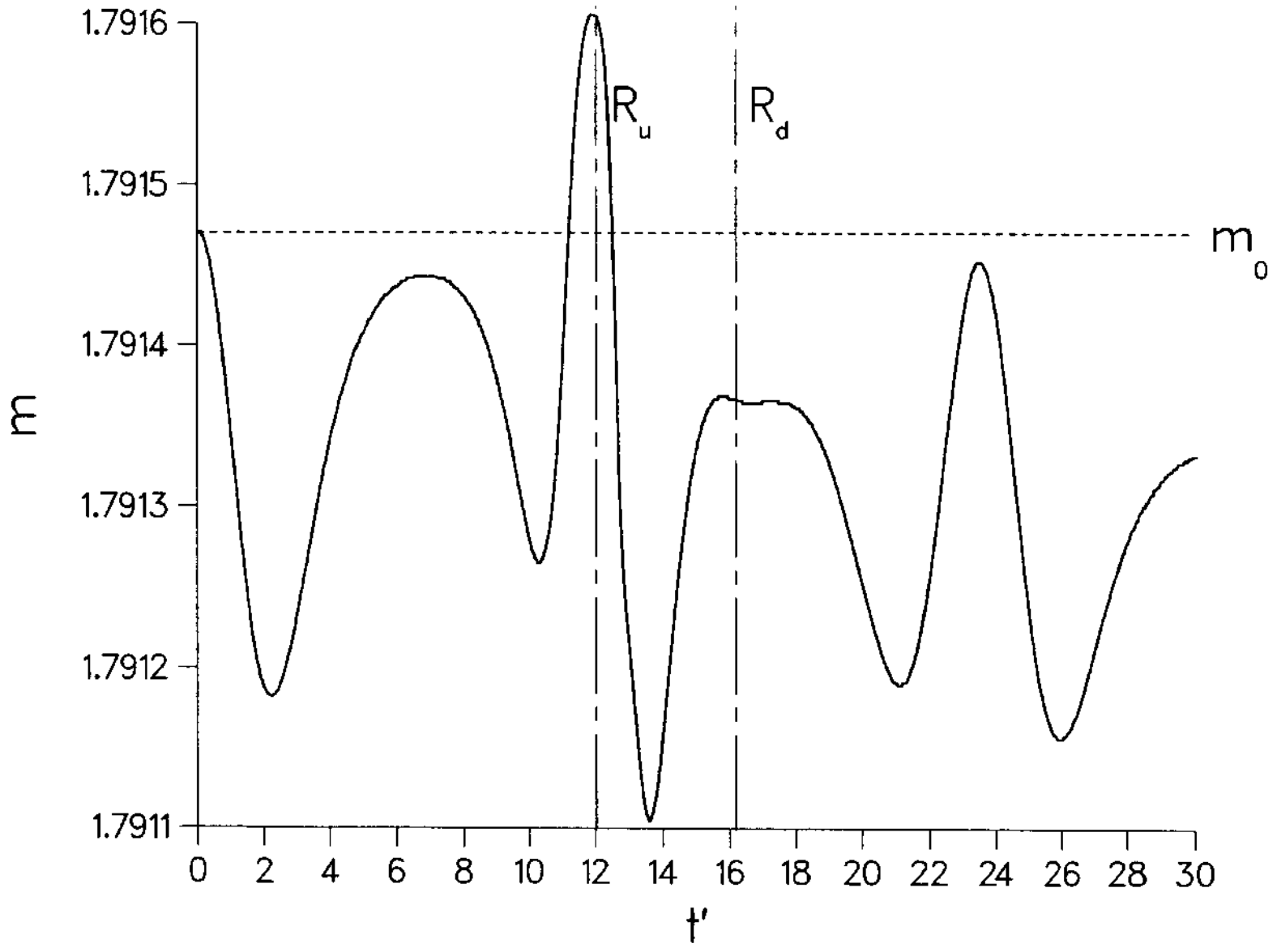

Fig. 6: 1st Order Solitary Waves Generation

Reflection On A Vertical Wall For Hi/d=0.25

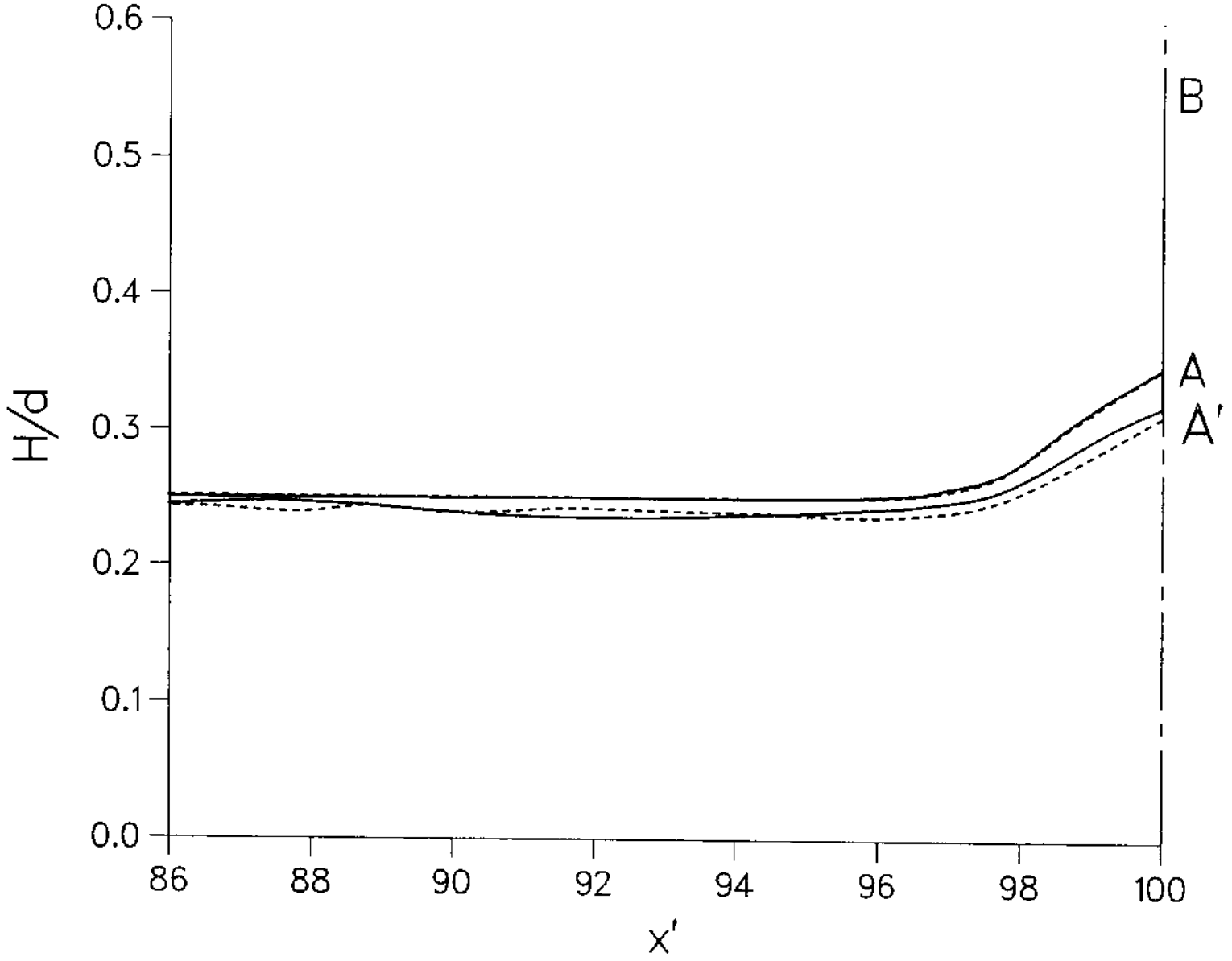

Fig. 7: Reflection On a Vertical Wall

Maximum Runup

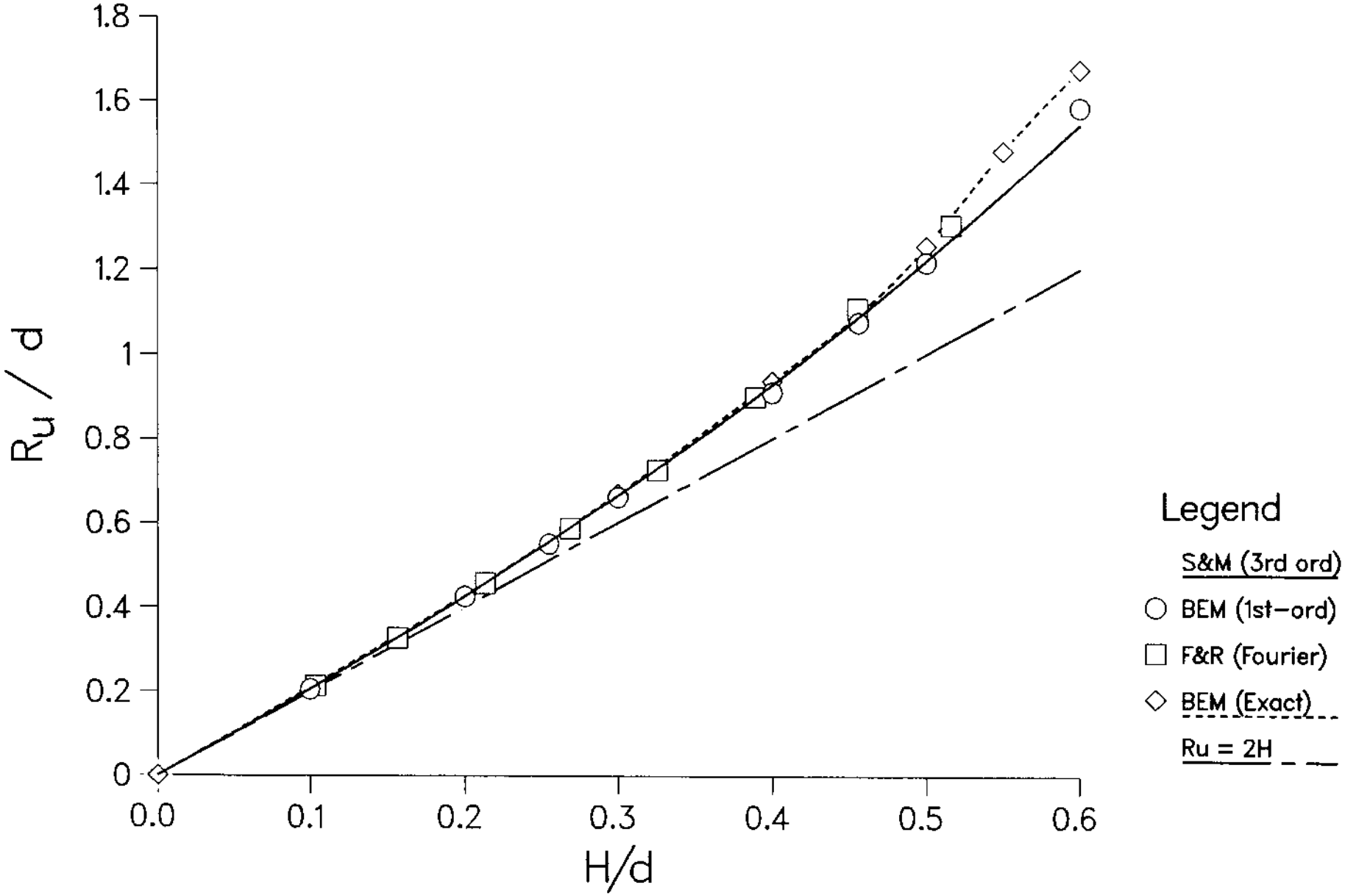

Fig. 8a: Reflection On a Vertical Wall

Maximum Rundown

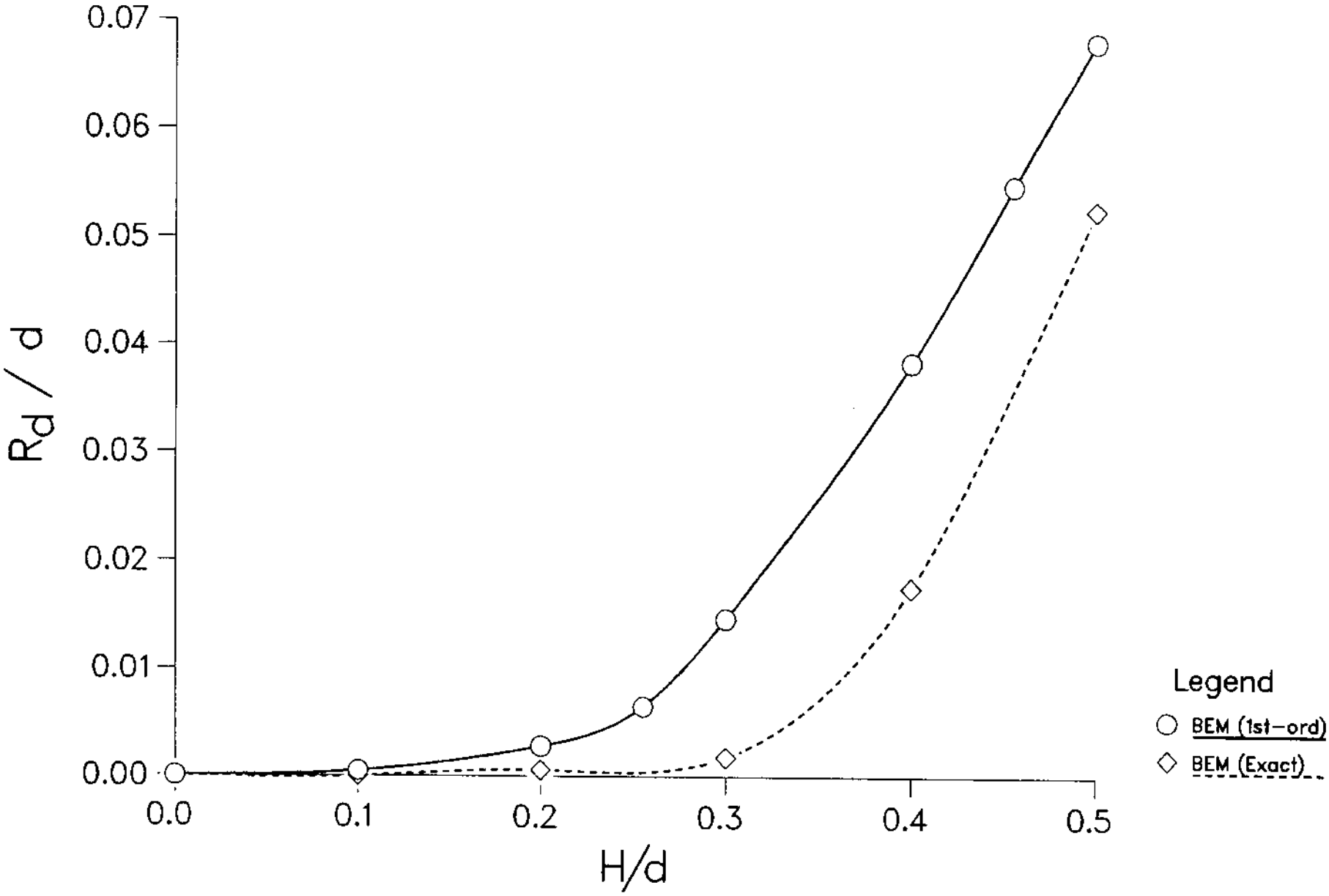

Fig. 8b: Reflection On A Vertical Wall

Reflected Exact Waves

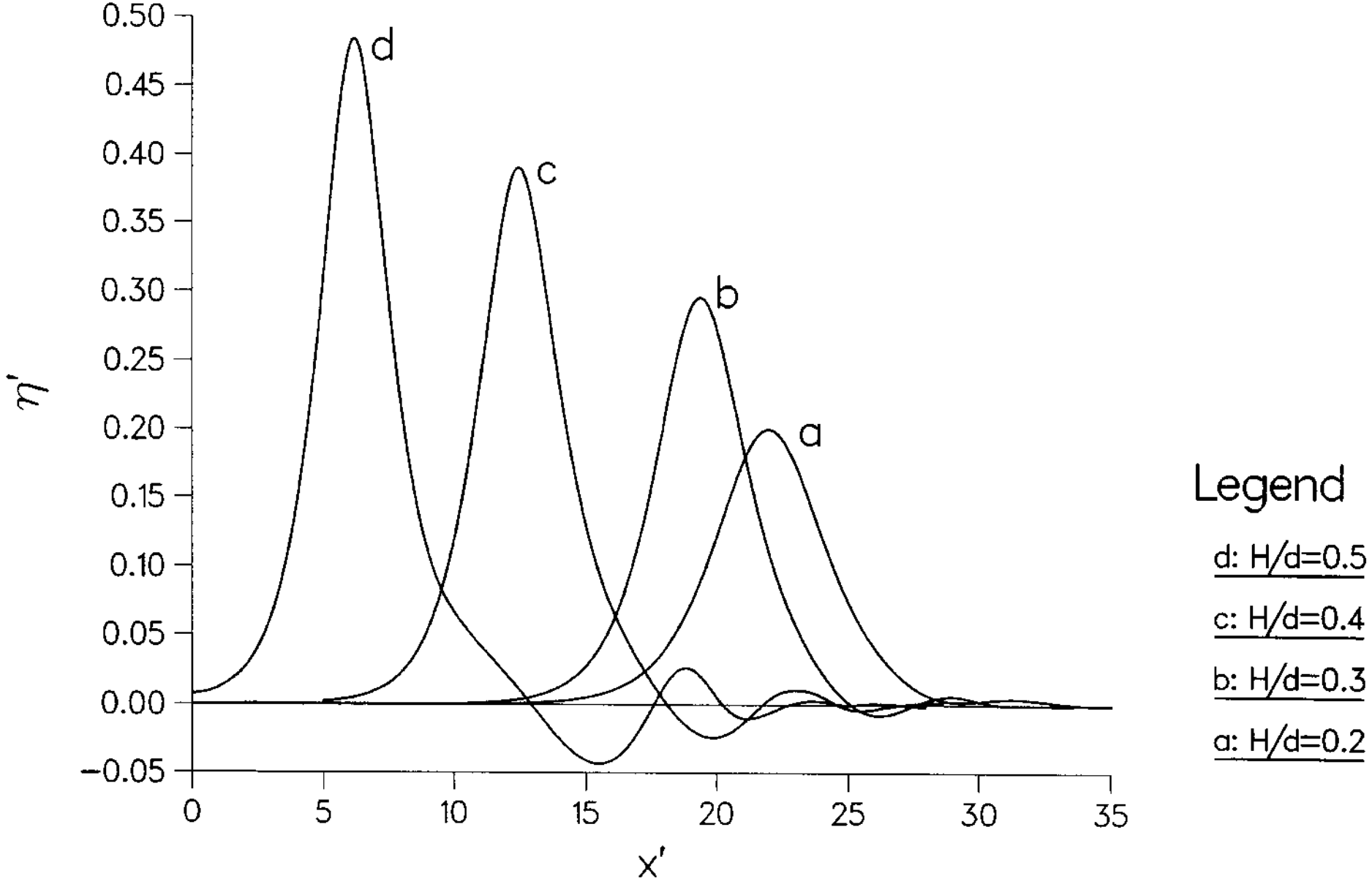

Fig. 9a: Reflection On A Vertical Wall

H/d=0.5 : I/R Waves for t'=23.525, tau2=3

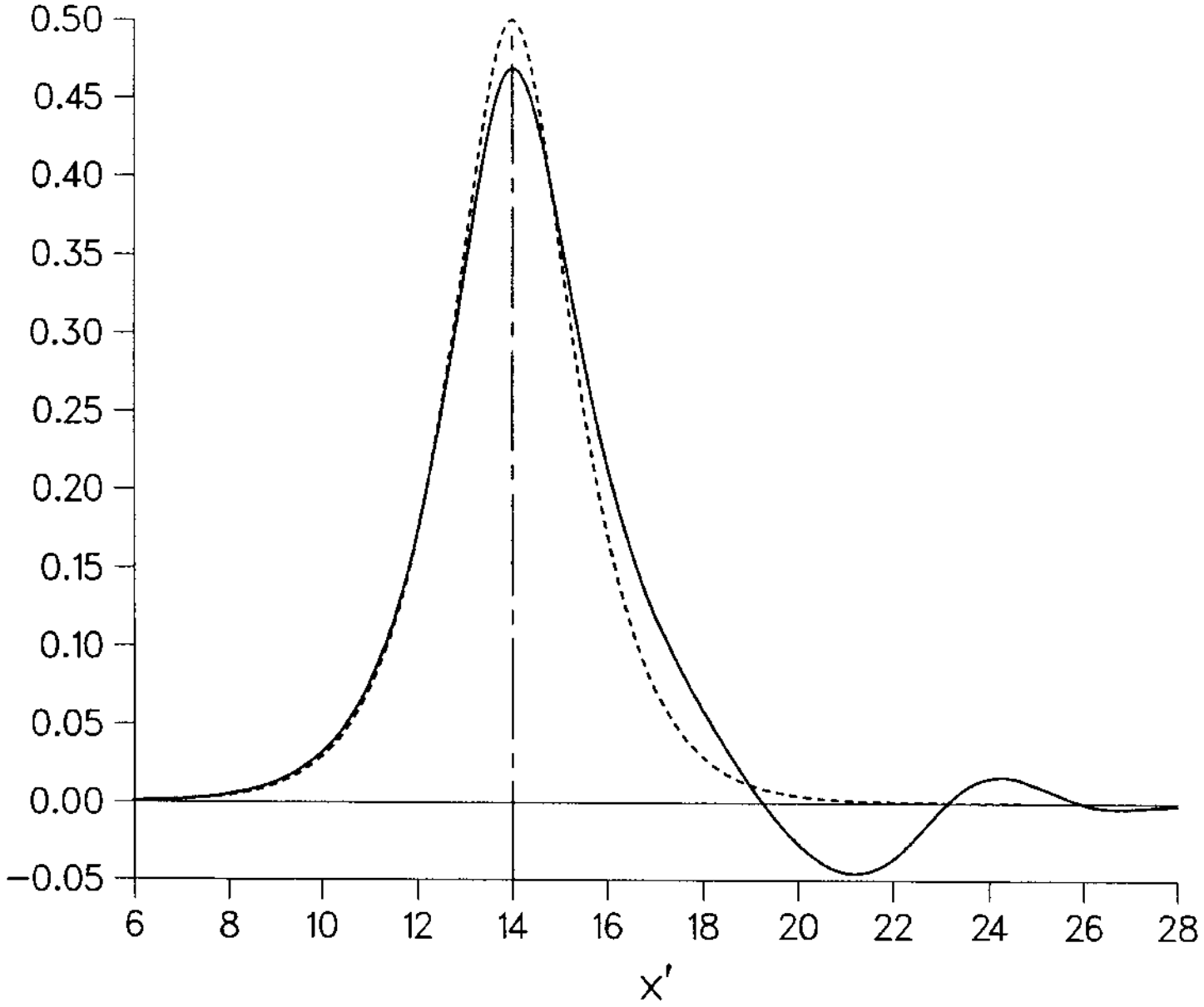

Fig. 9b: Reflection On A Vertical Wall

Amplitude Drop for H/d=0.5

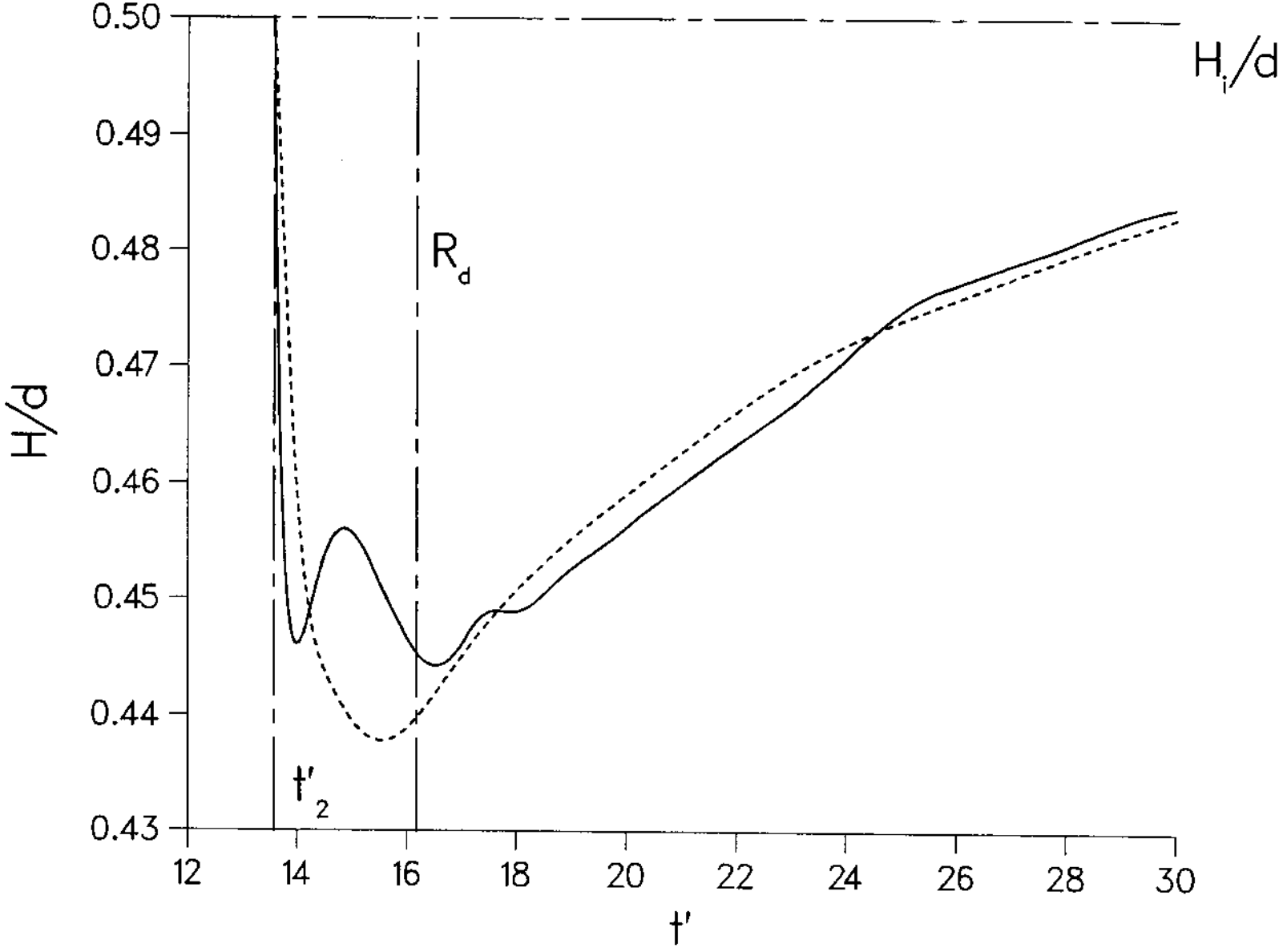

Fig. 9c: Reflection On A Vertical Wall

H/d=0.5 : Oscillatory Tail : x'_o=14.00, tau2=3

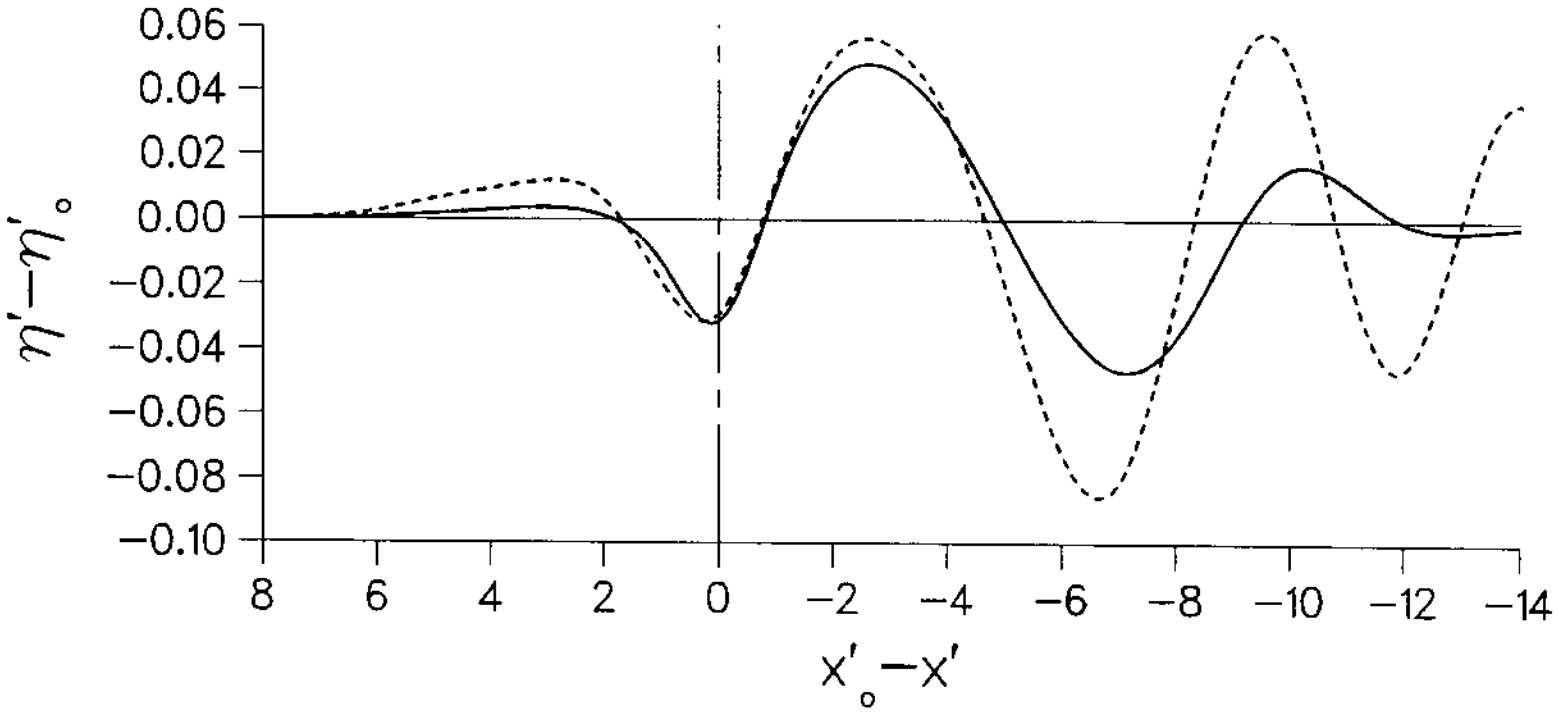

Fig. 10a: Reflection On A Vertical Wall

Phase diagram H/d=0.5, dt=0.05-0.025, dx/d=0.25

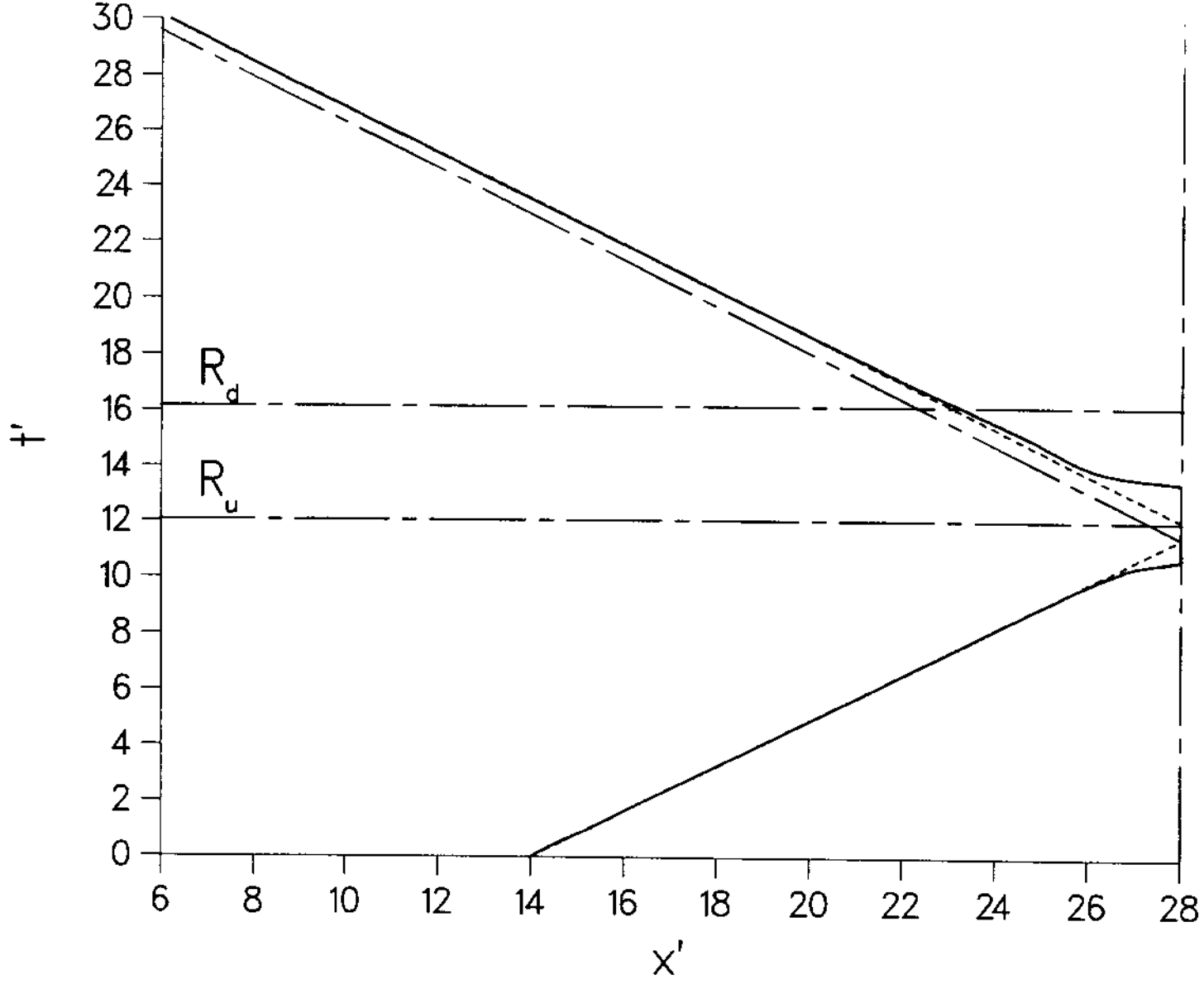

Fig. 9d: Reflection On A Vertical Wall

H/d=0.5 : Oscillatory Tail : x'_o =6.185,tau2=5

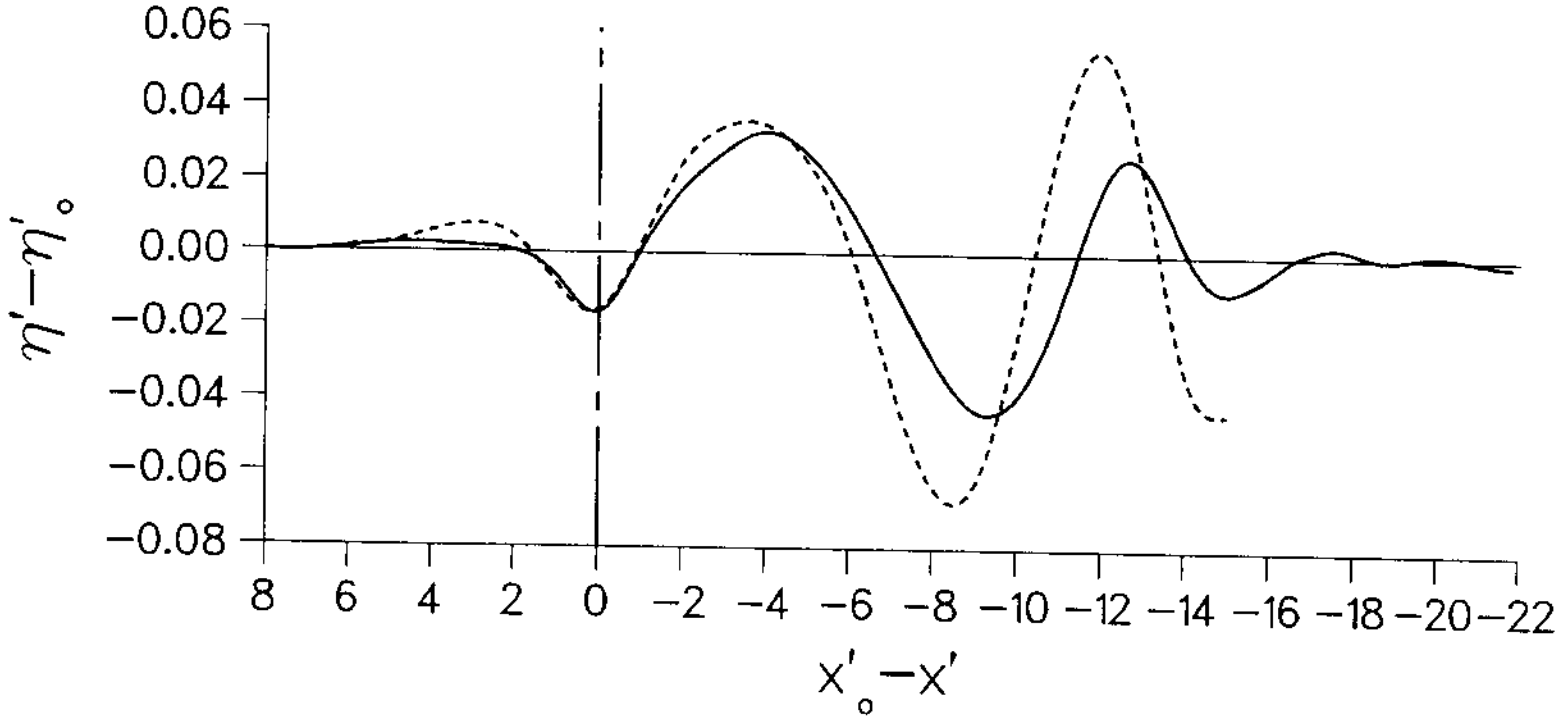

Fig. 10b: Reflection On A Vertical Wall

Phase shift H/d=0.5, dt=0.05-0.025, dx/d=0.25

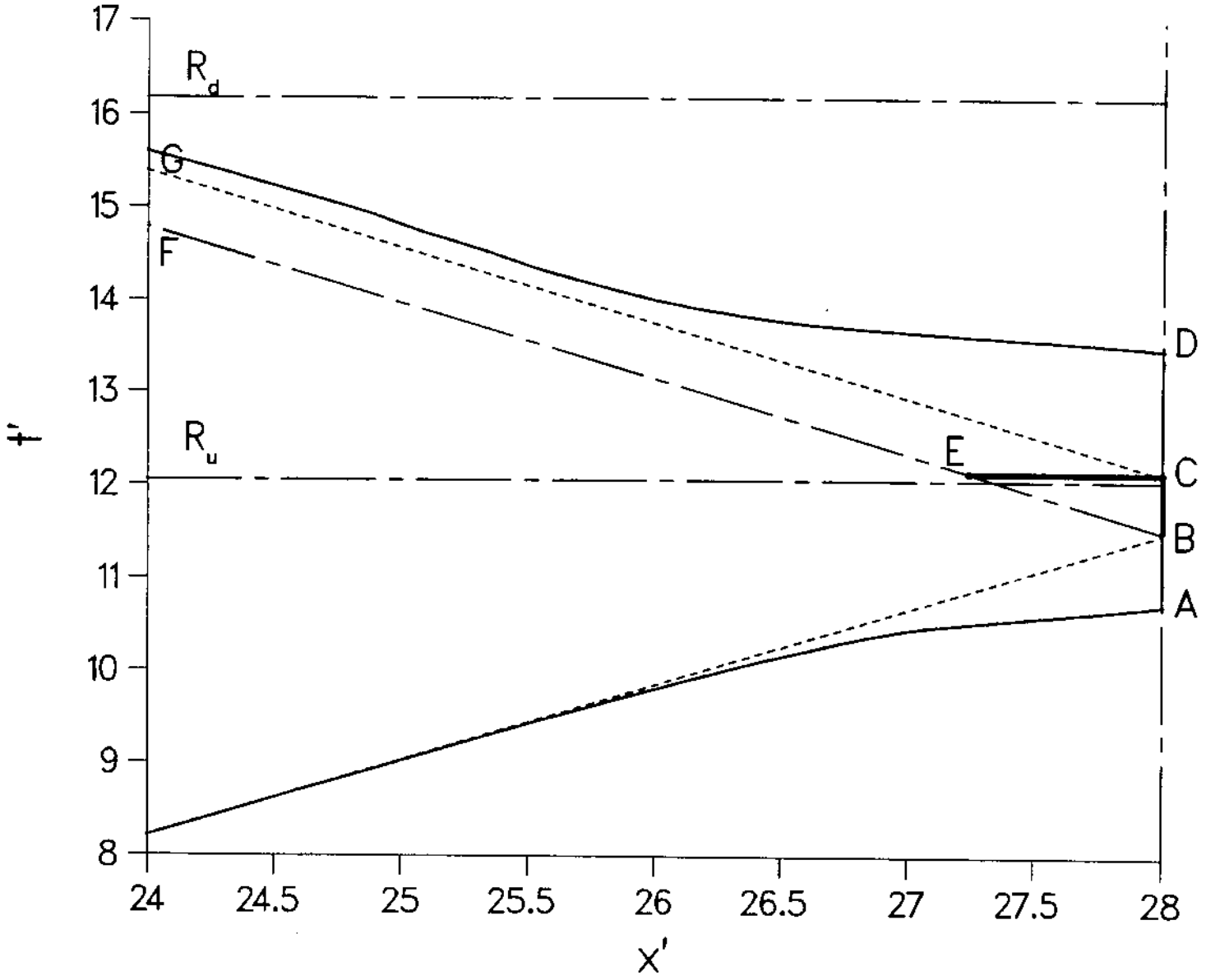

Fig. 11a: Reflection On A Vertical Wall

Energy, H/d=0.5, dt=0.05-0.025, dx/d=0.25

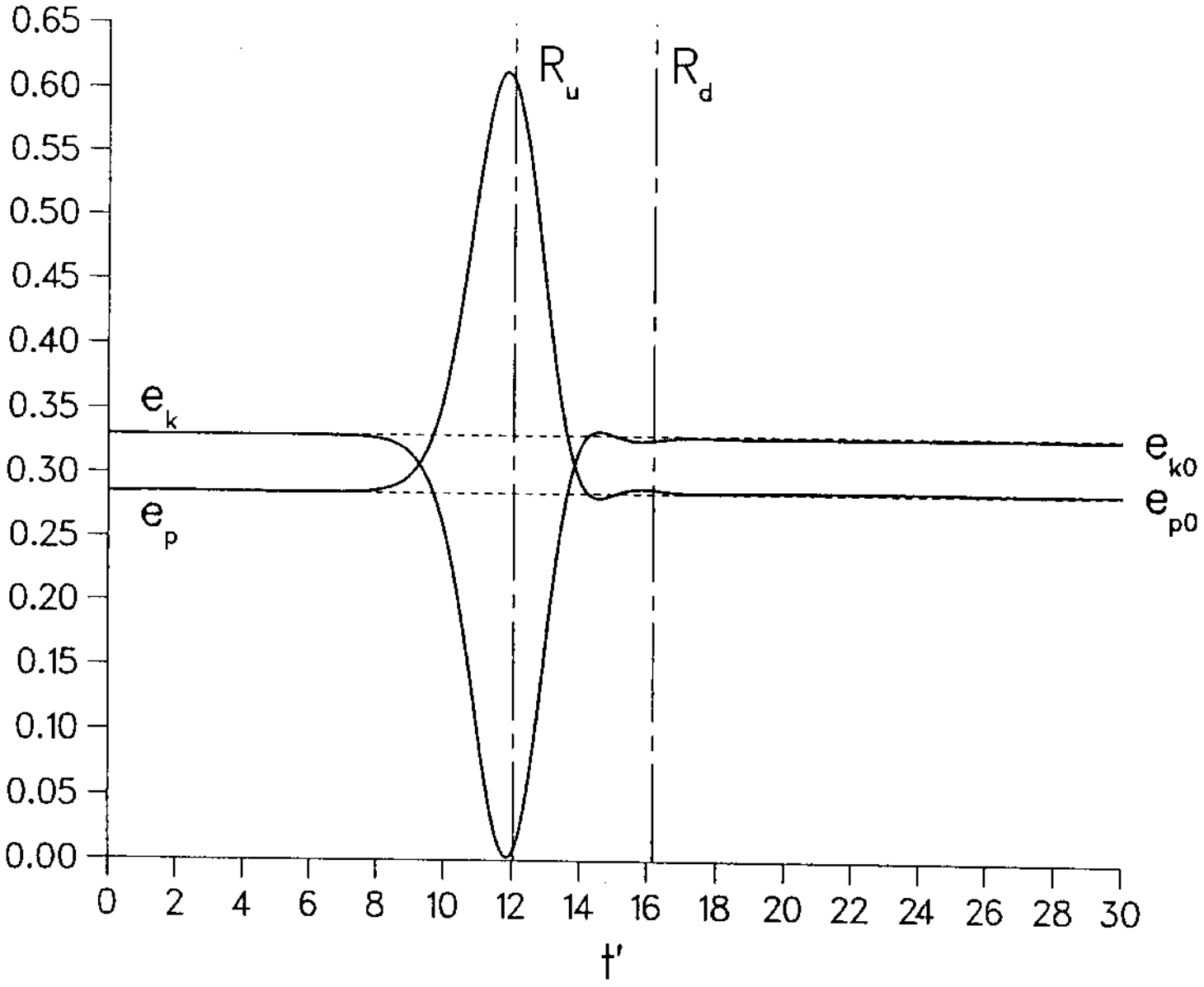

Fig. 11b: Reflection On A Vertical Wall

Energy, H/d=0.5, dt=0.05-0.025, dx/d=0.25

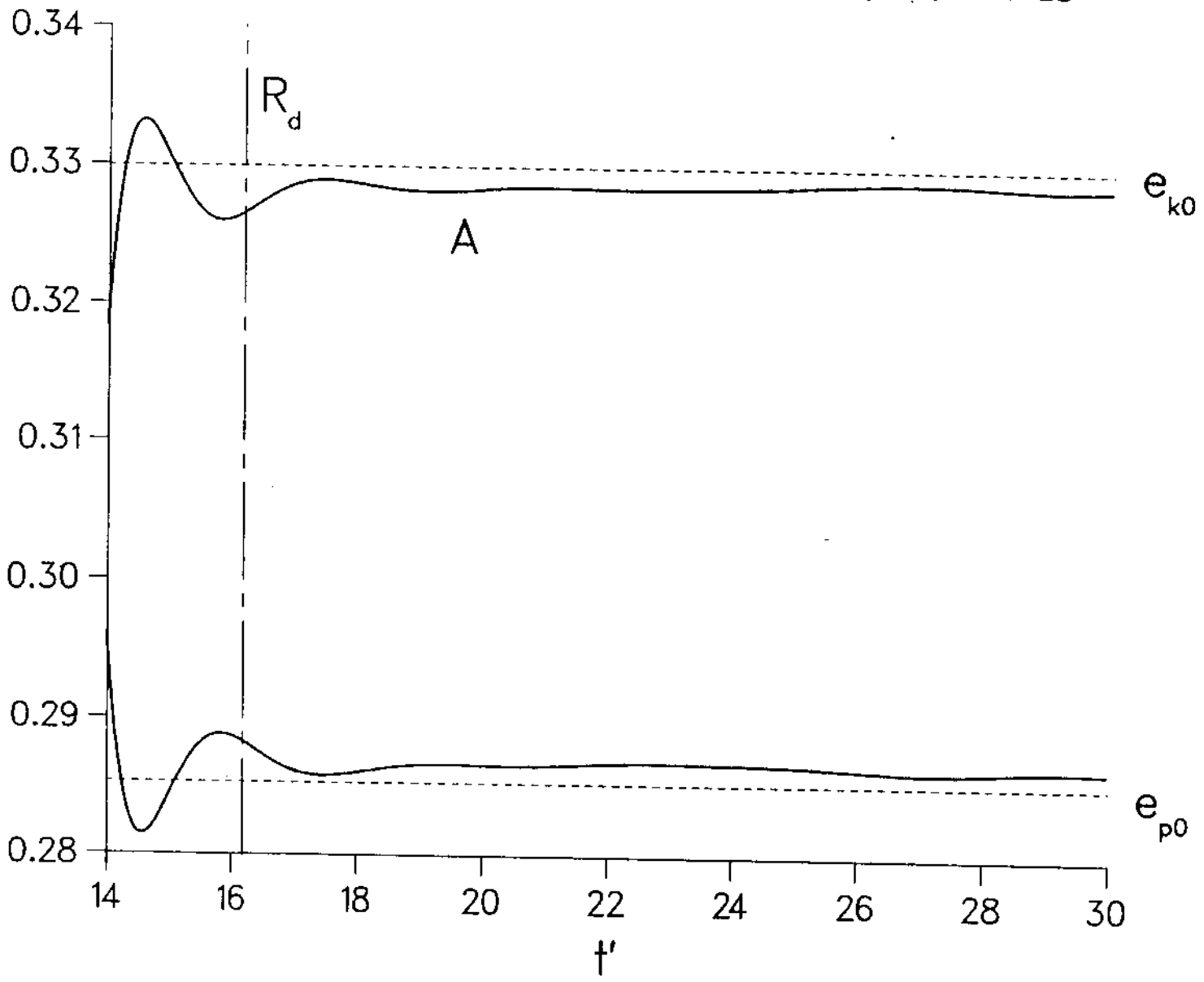

Fig. 12a: Reflection On a Vertical Wall

Maximum Horizontal Force

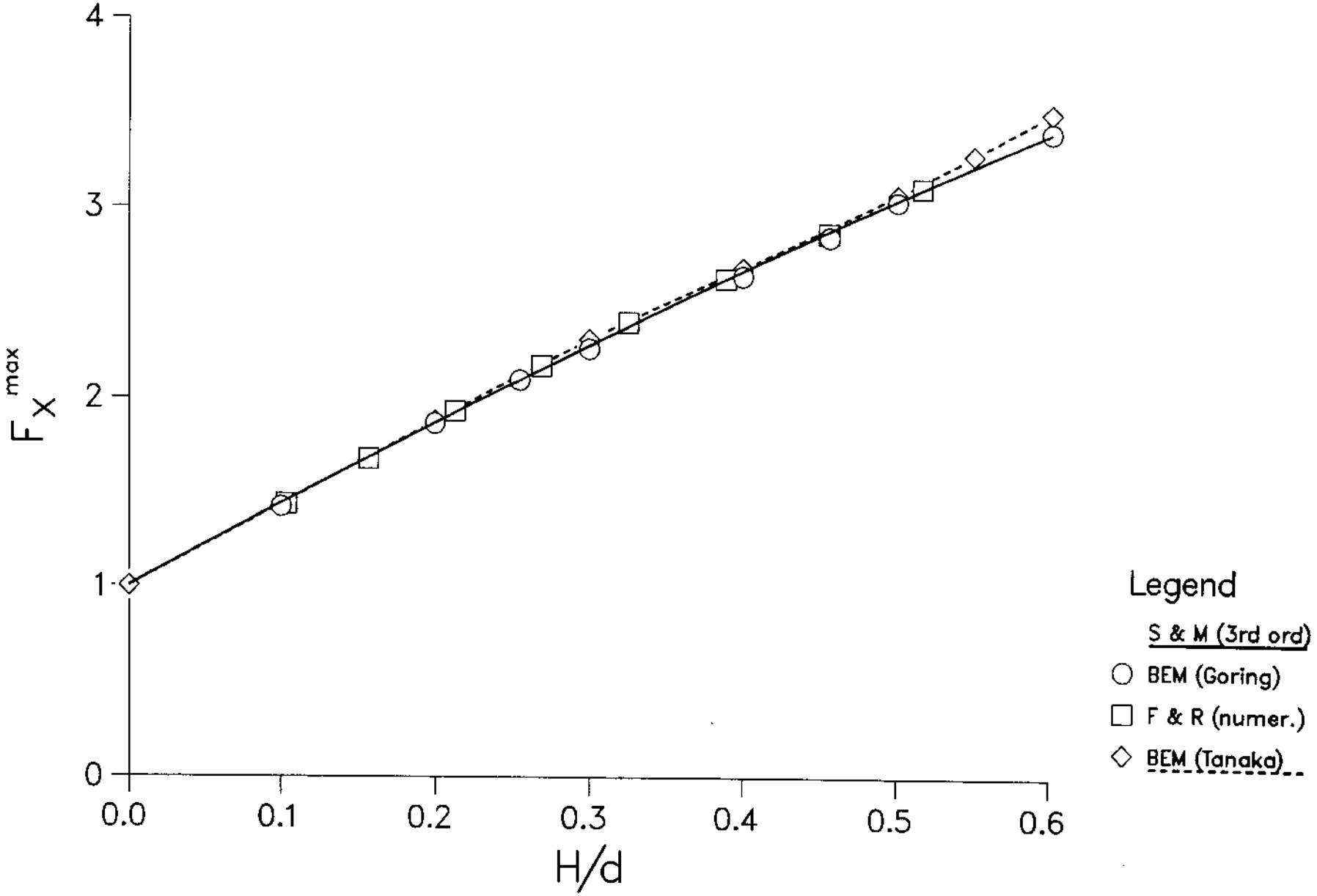

Fig. 12b: Reflection On a Vertical Wall

Maximum Moment With Respect To The Bottom Of The Wall

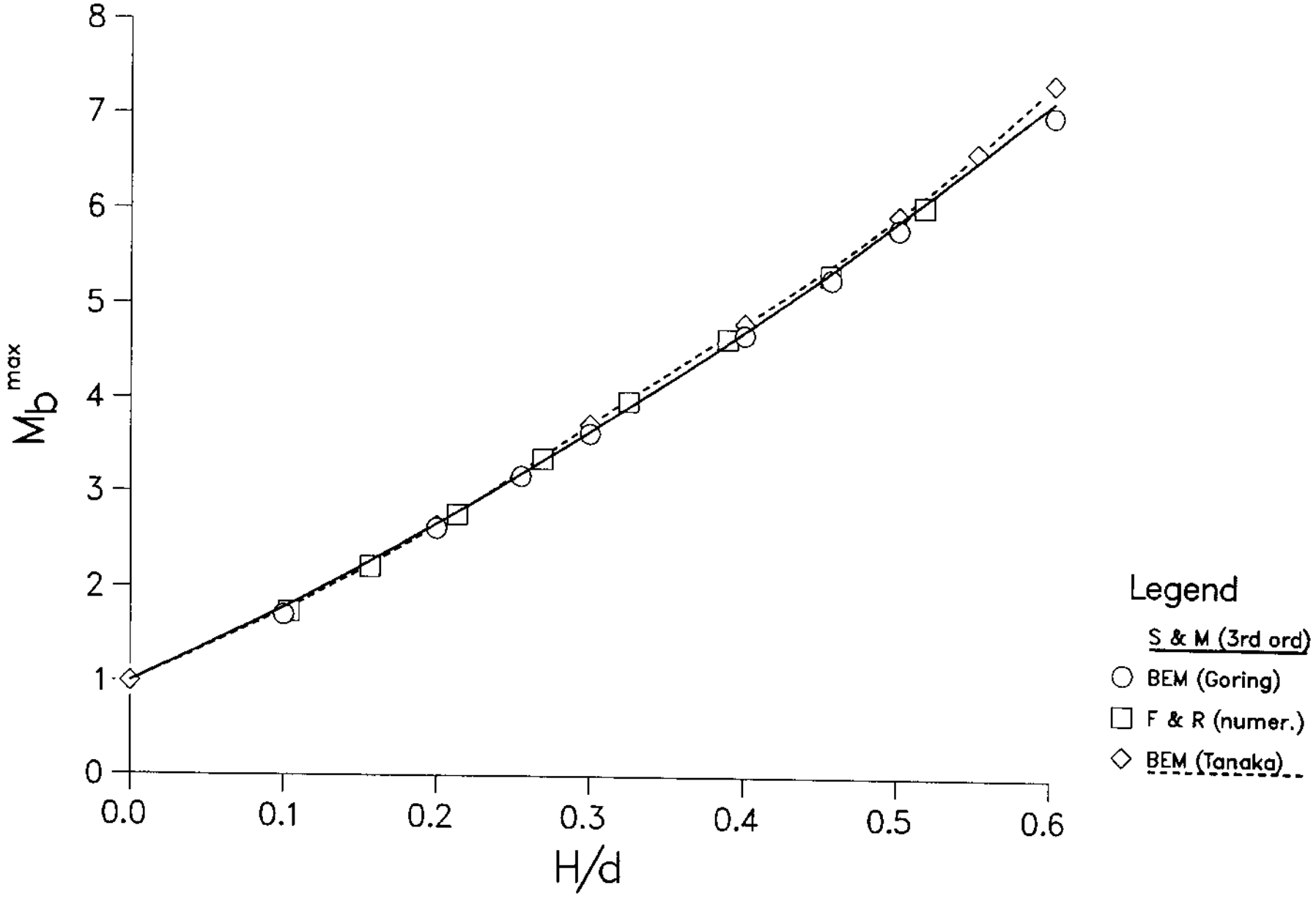

Fig. 13a: Reflection On A Vertical Wall

Horizontal Force In Time

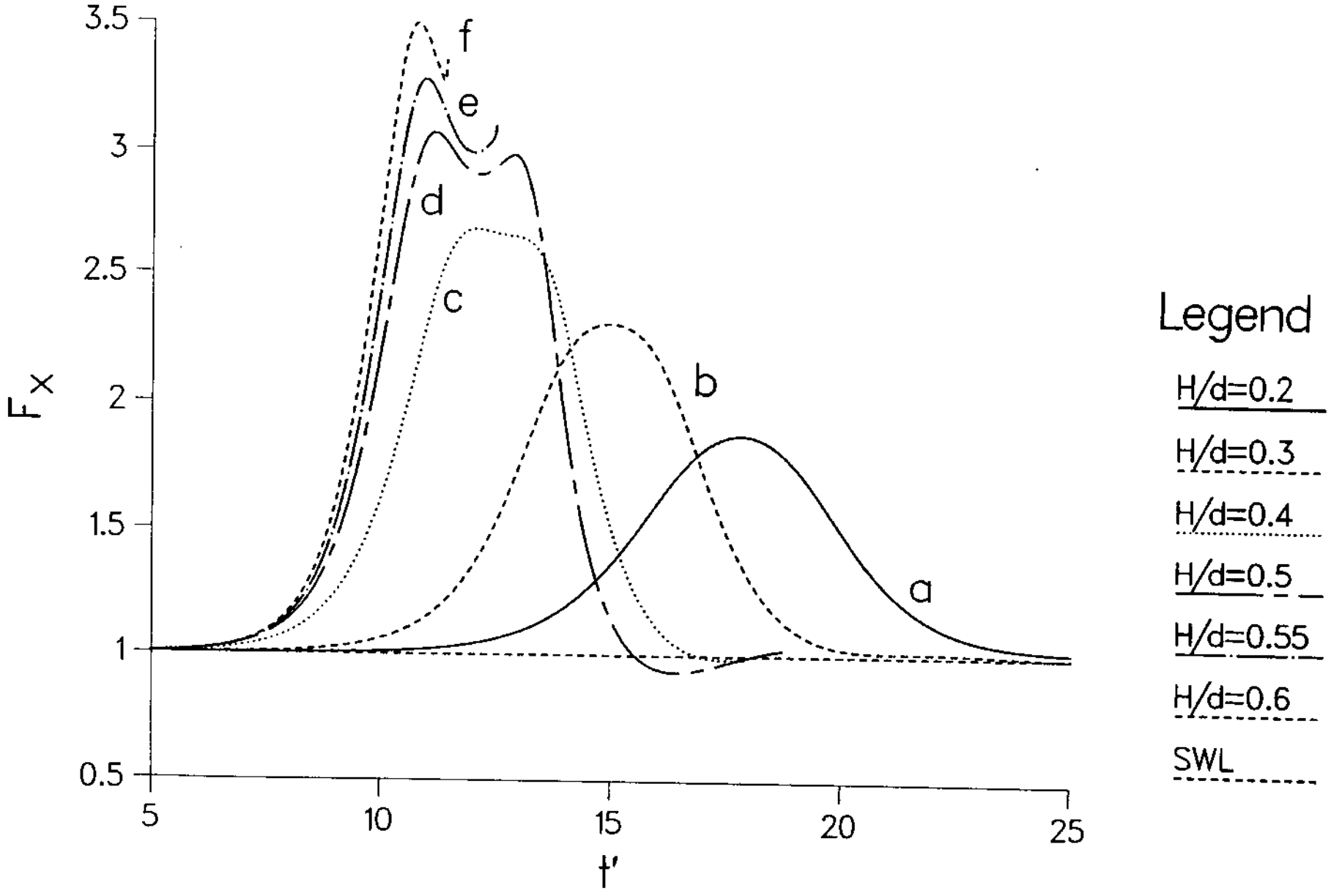

Fig. 13b: Reflection On A Vertical Wall

Mechanics, H/d=0.5, dt=0.05-0.025, dx/d=0.25

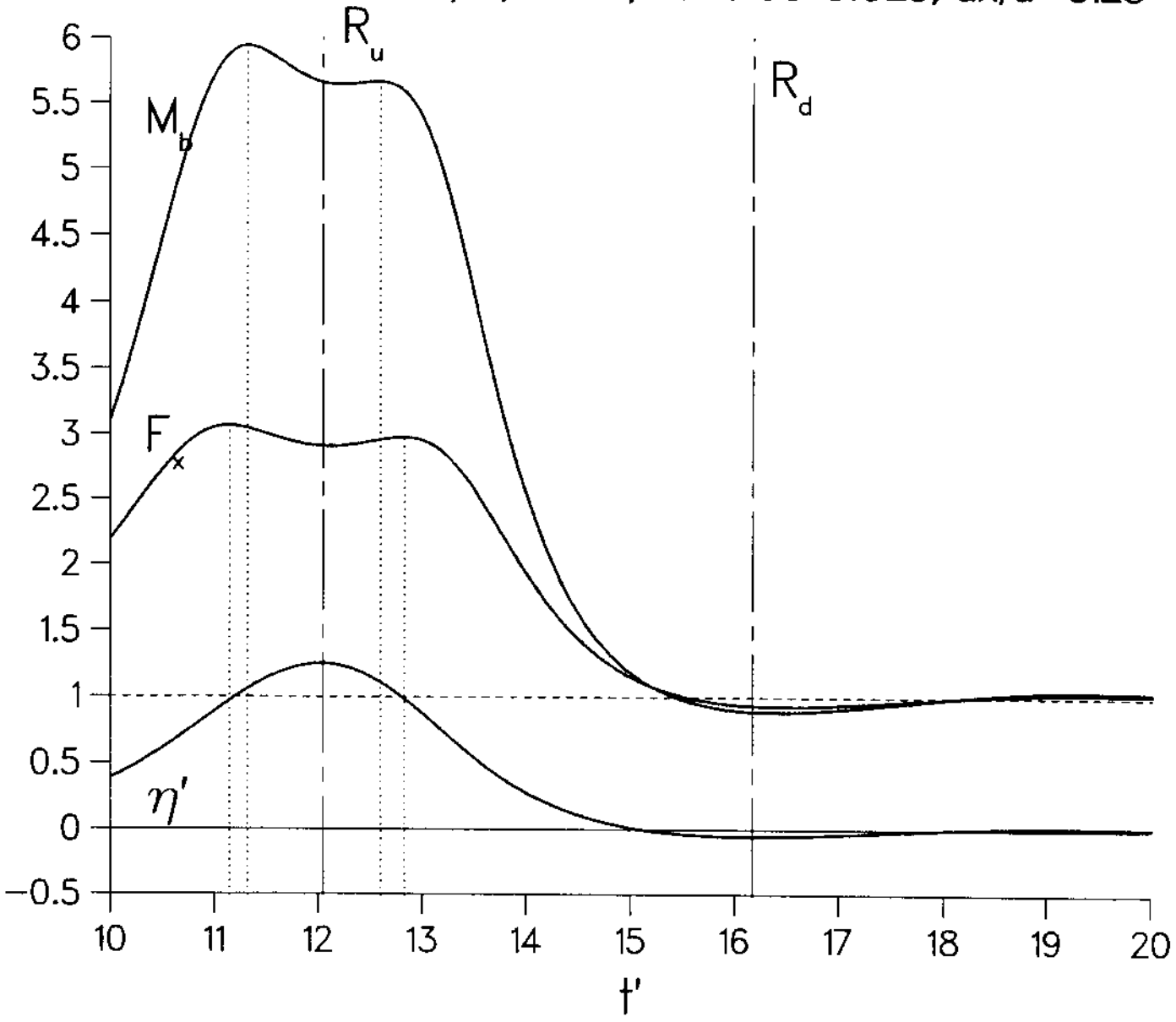

Fig. 14a: Reflection On a 45 Degree Slope

Solitary Wave, H/d = 0.269

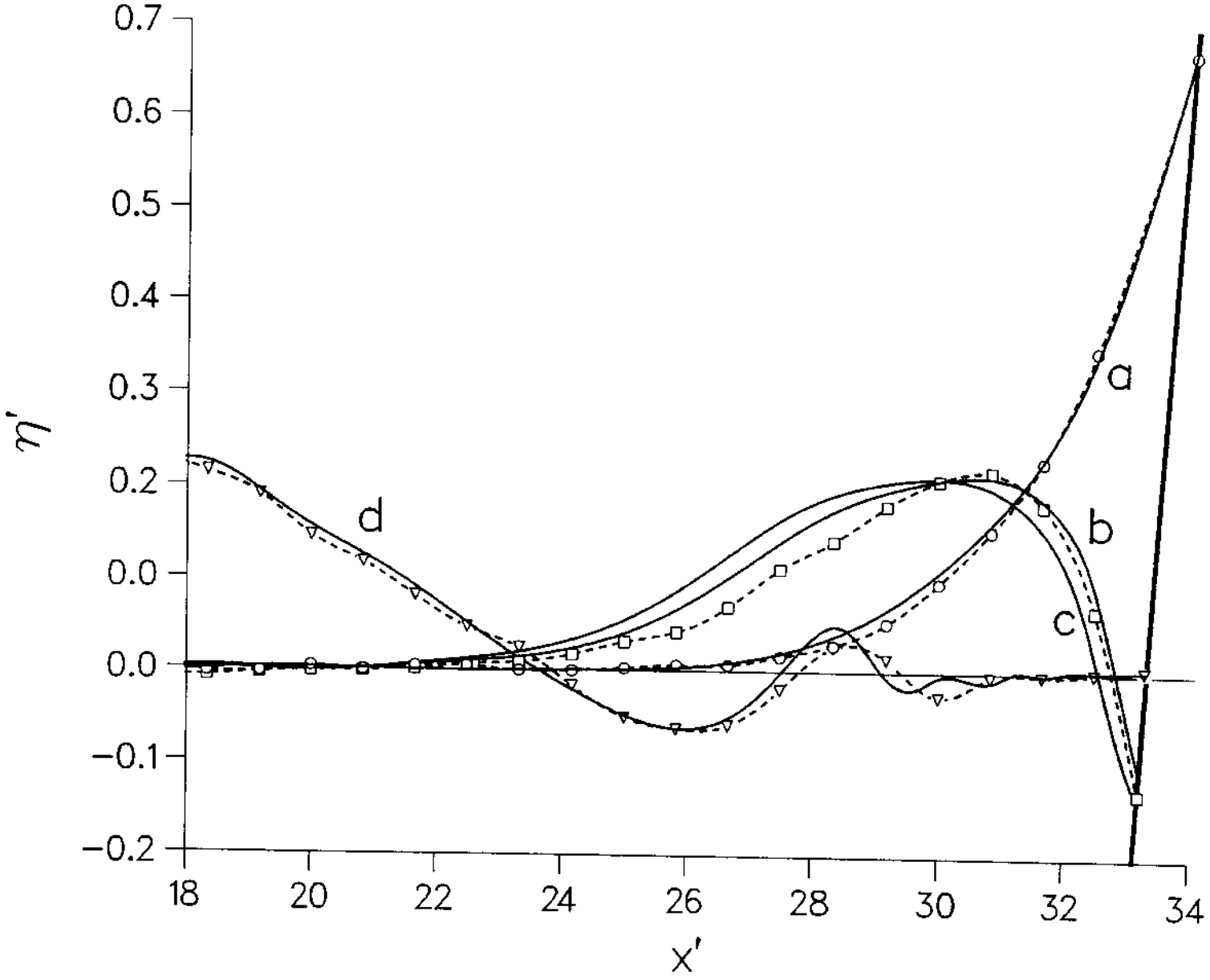

Fig. 14b: Reflection On a 45 Degree Slope

Solitary Wave, H/d = 0.457

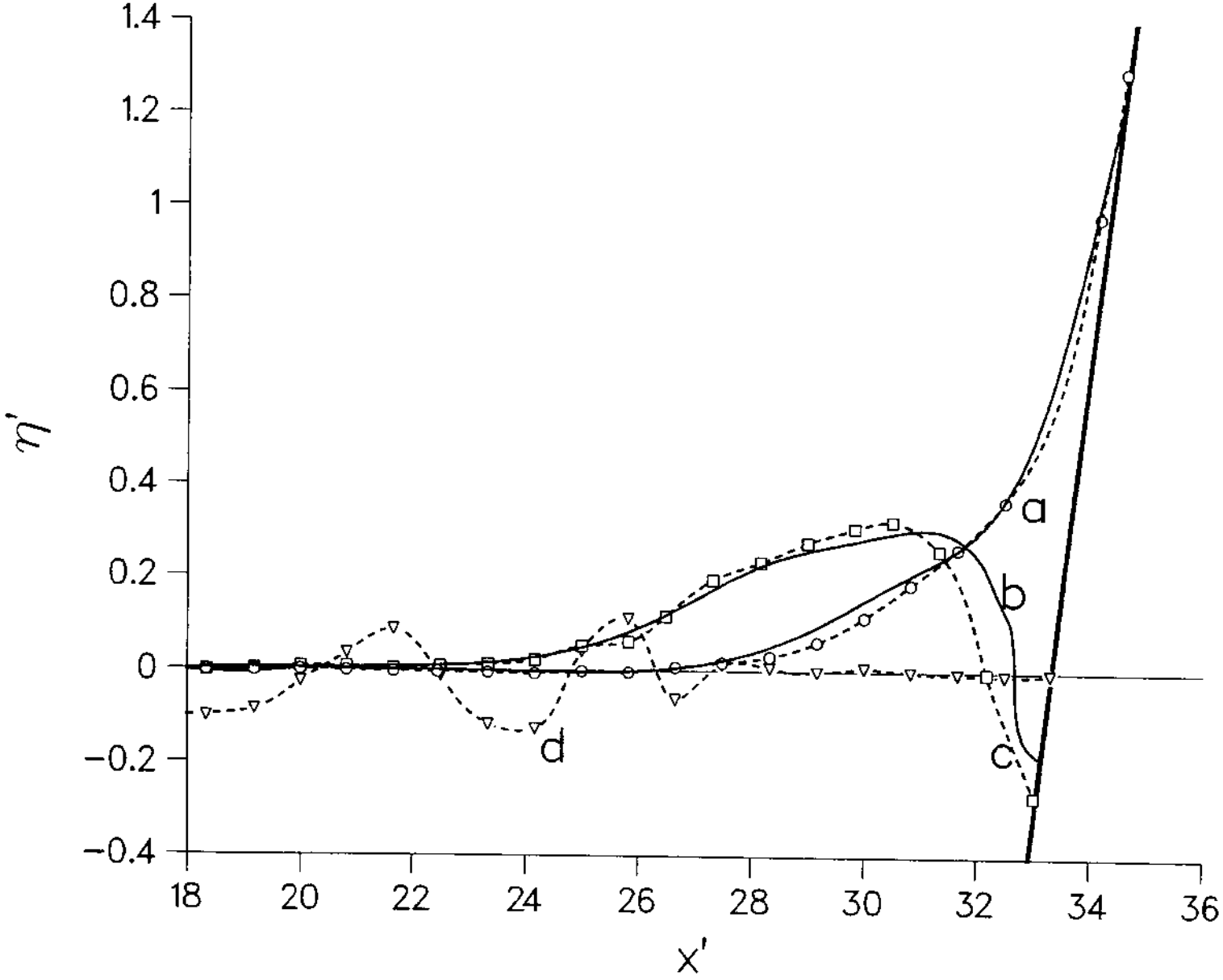

Fig. 15a: Reflection On a 70 Degree Slope

Solitary Wave, H/d = 0.259

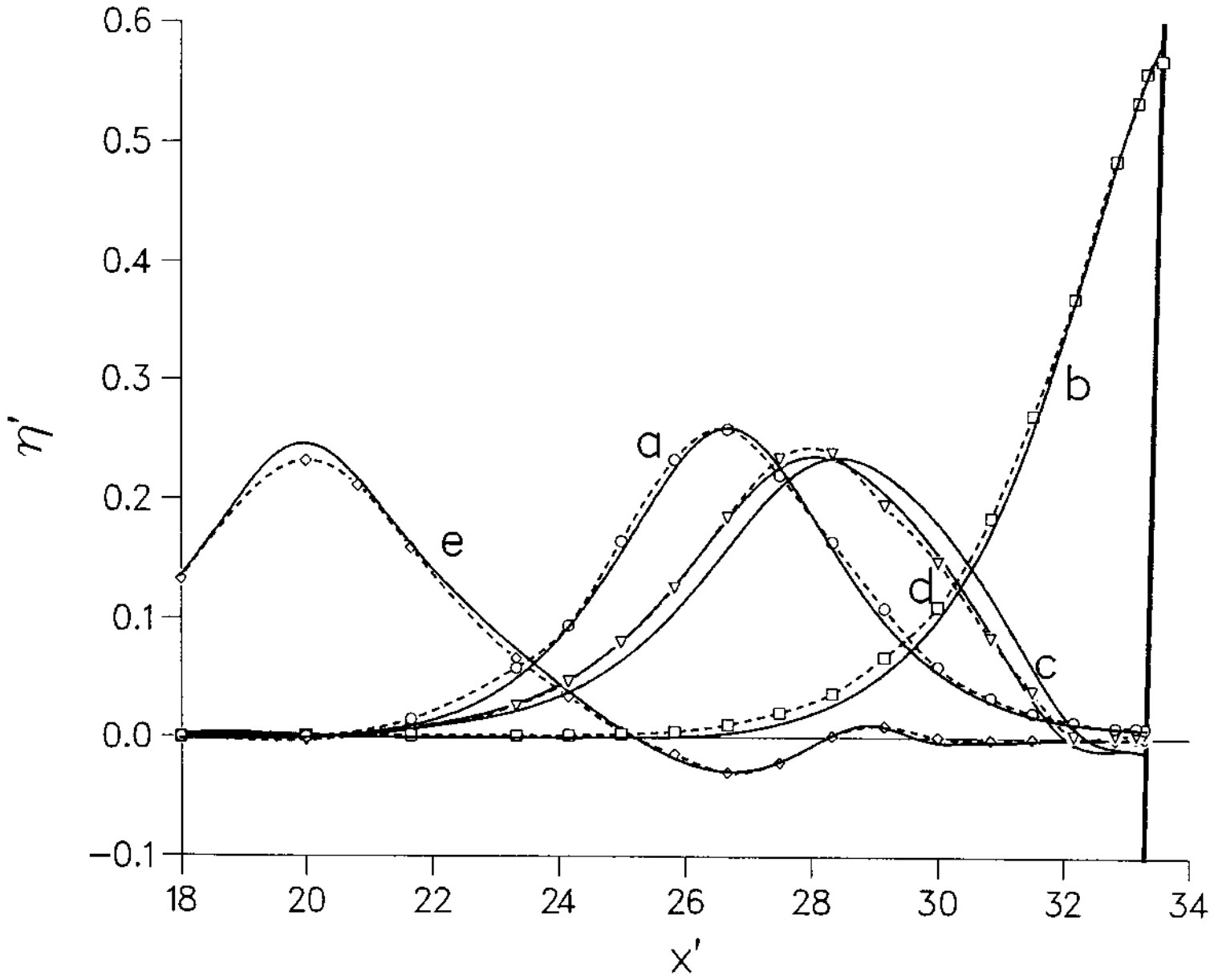

Fig. 15b: Reflection On a 70 Degree Slope

Solitary Wave, H/d = 0.437

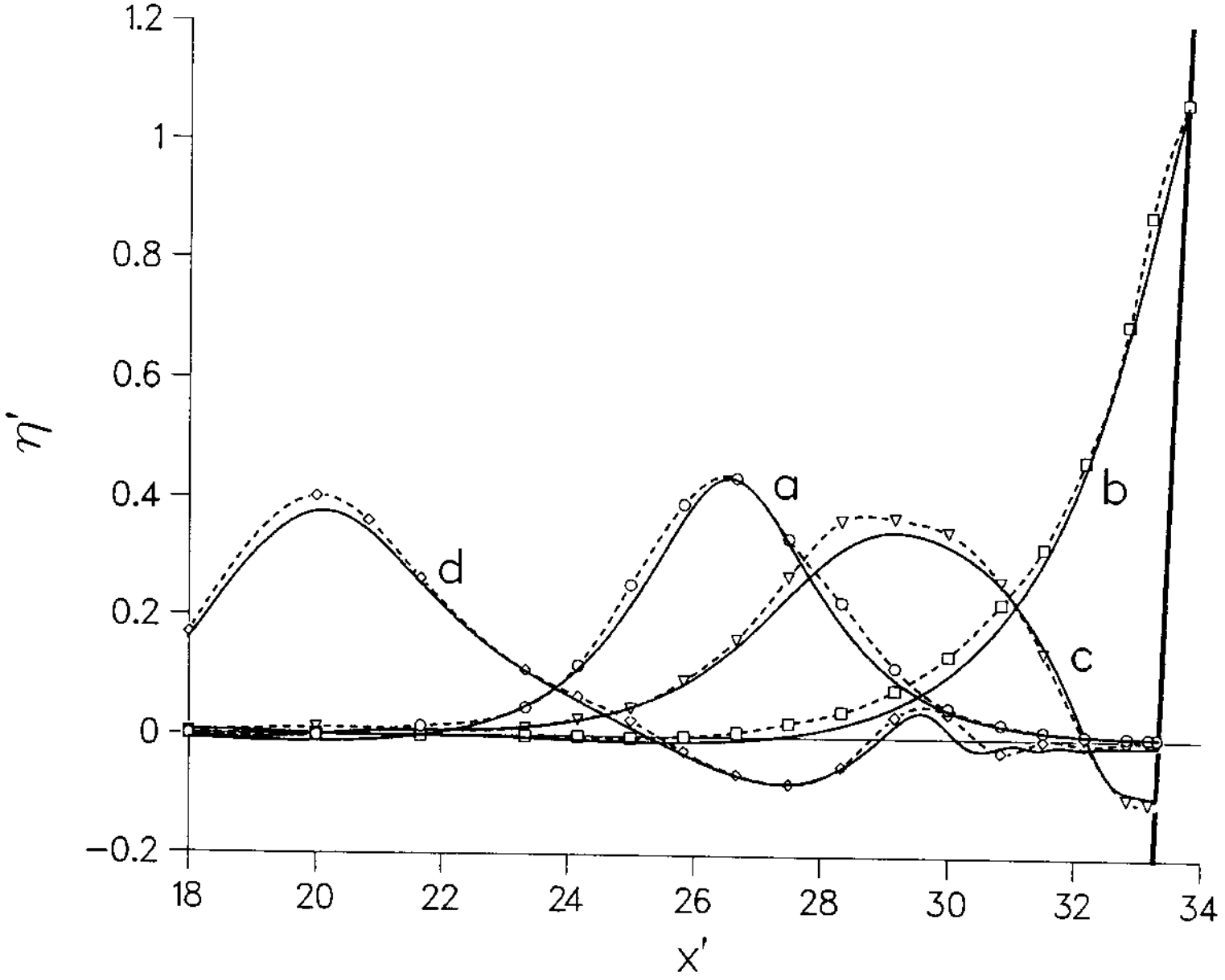

Fig. 16a: Velocity Field, t′ = 30.375

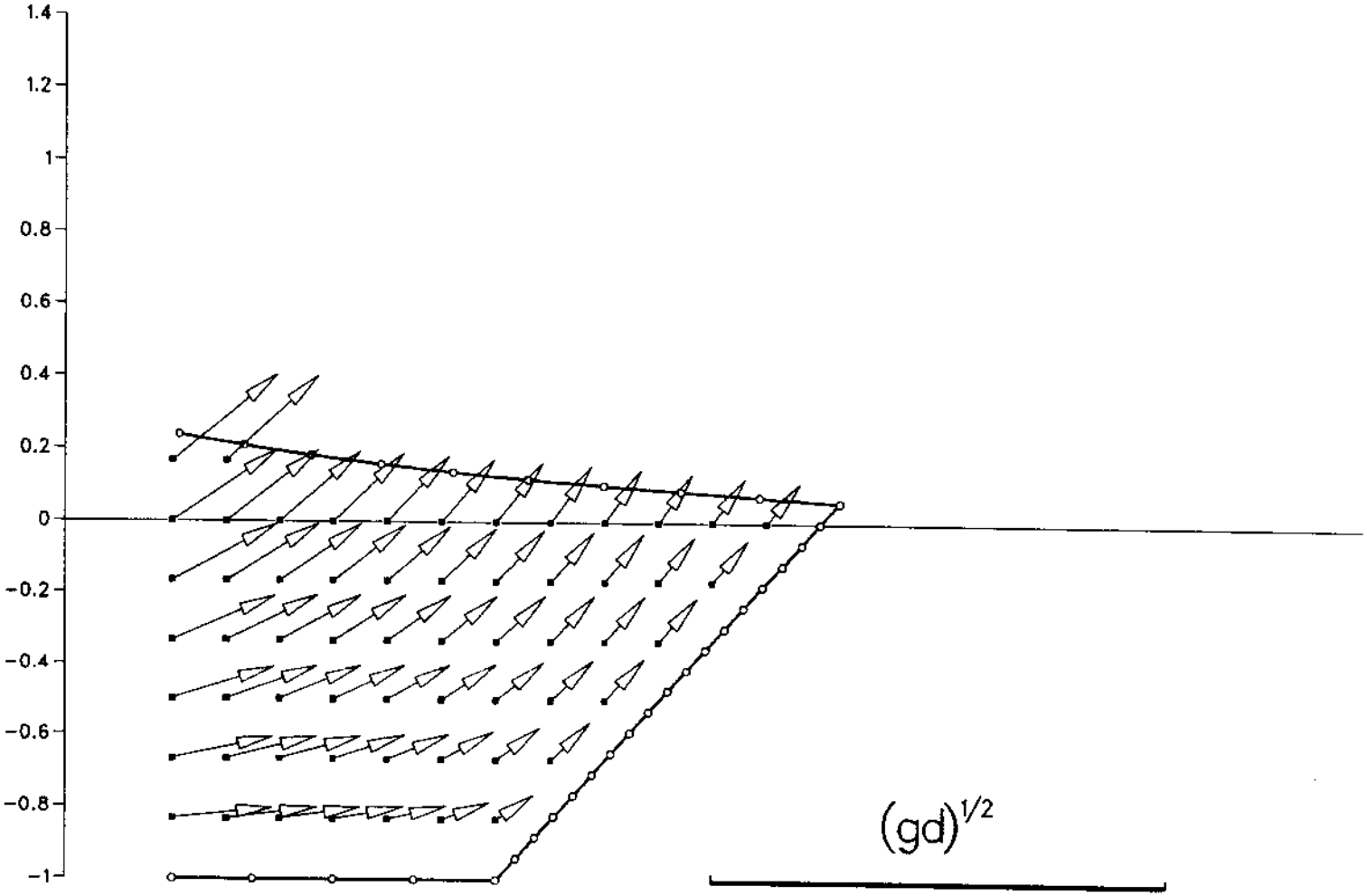

Fig. 16b: Velocity Field, $t' = 32.050$

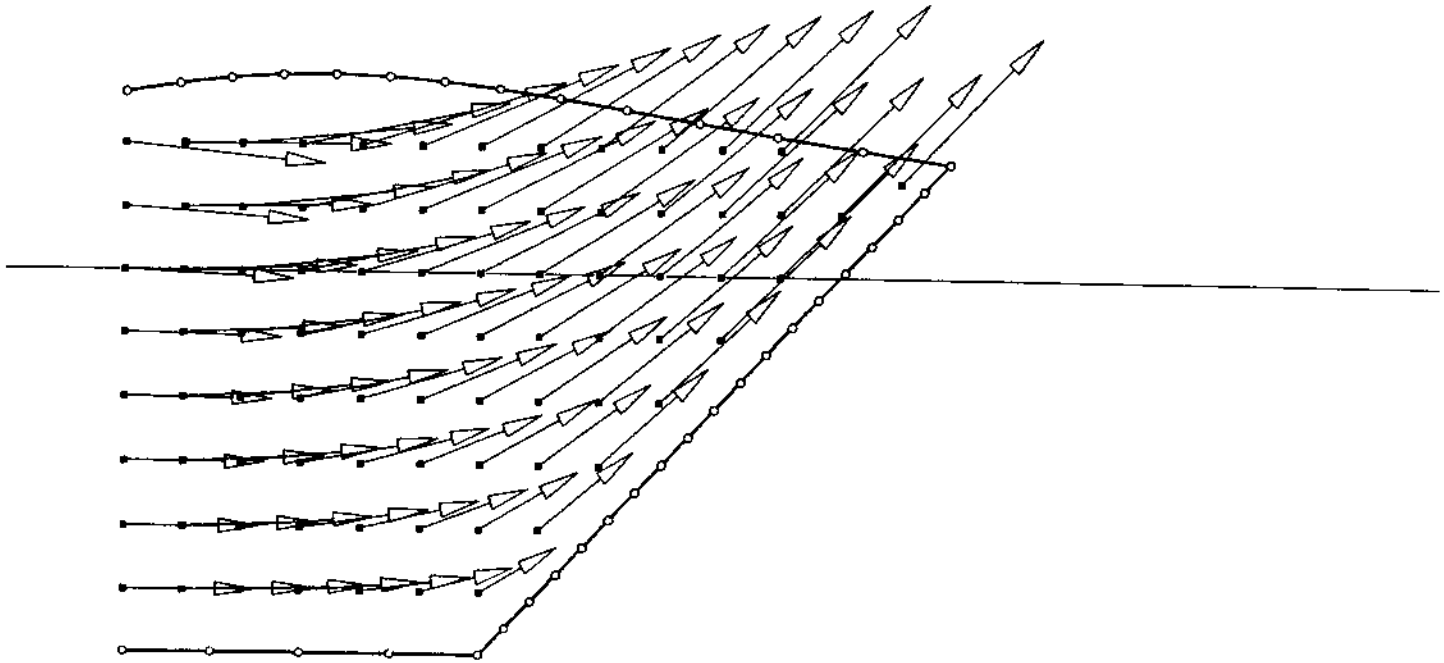

Fig. 16c: Velocity Field, $t' = 33.150$

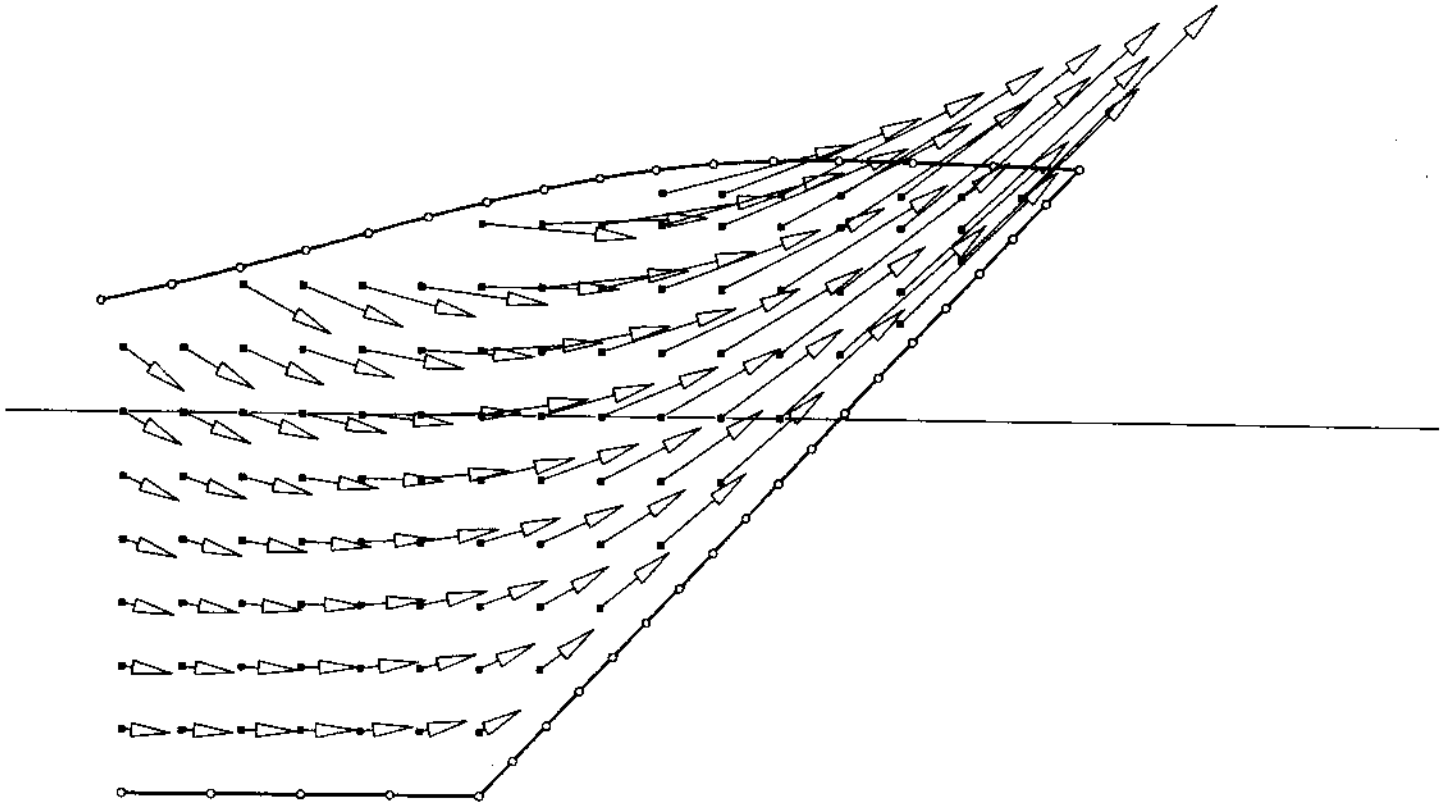

Fig.16d: Velocity Field, t′ = 33.975

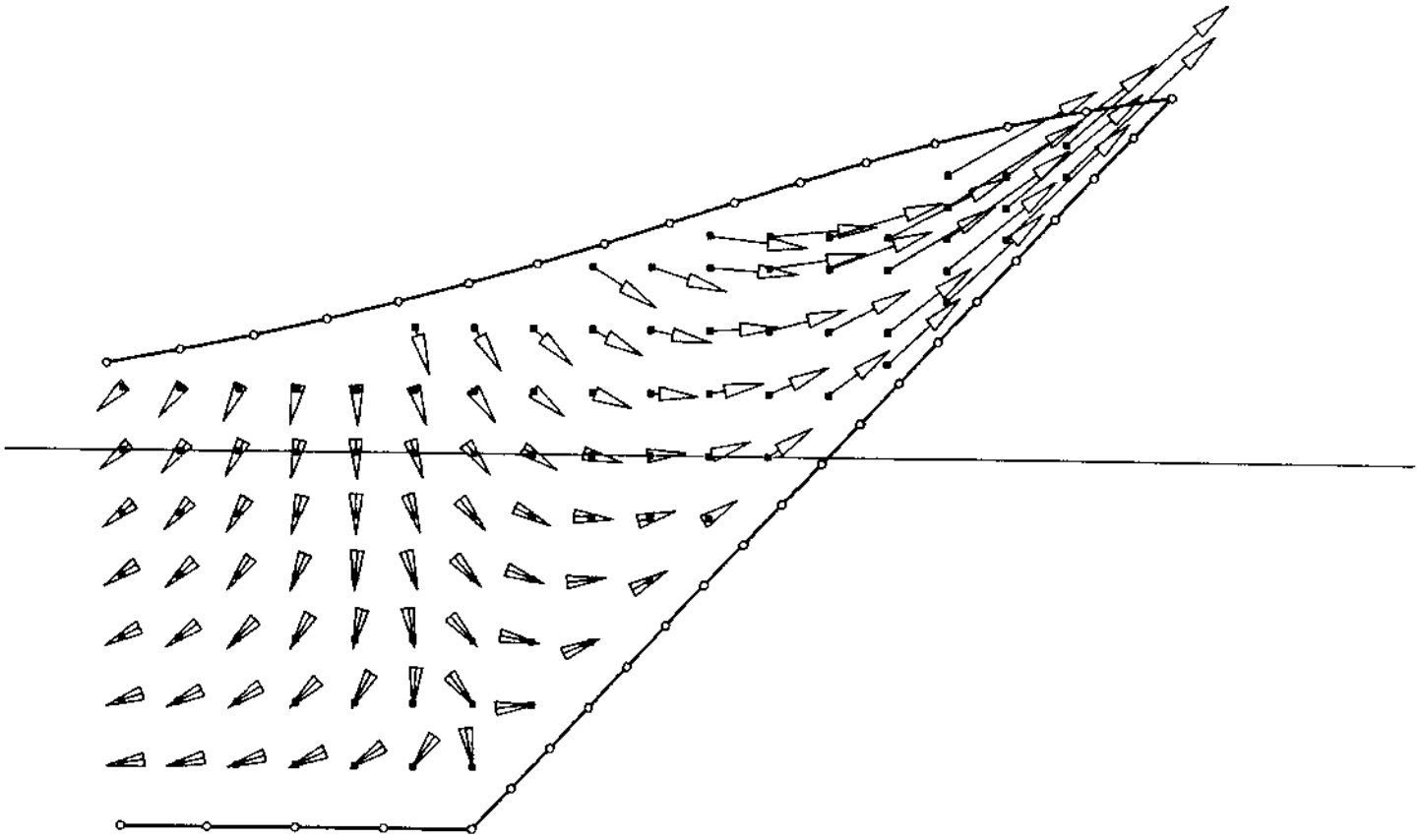

Fig. 16e: Velocity Field, $t' = 34.875$

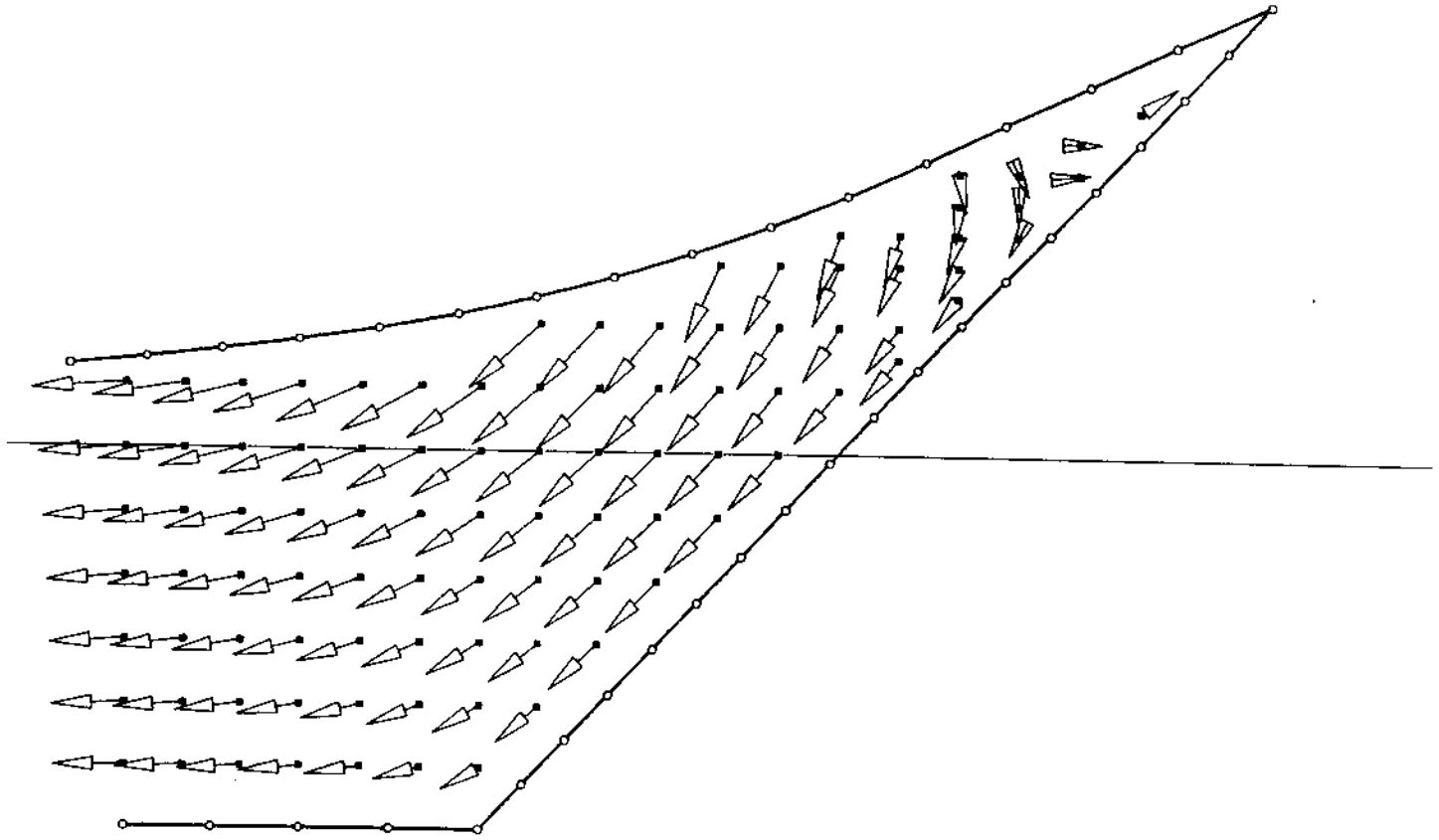

Fig. 16f: Velocity Field, $t' = 35.375$

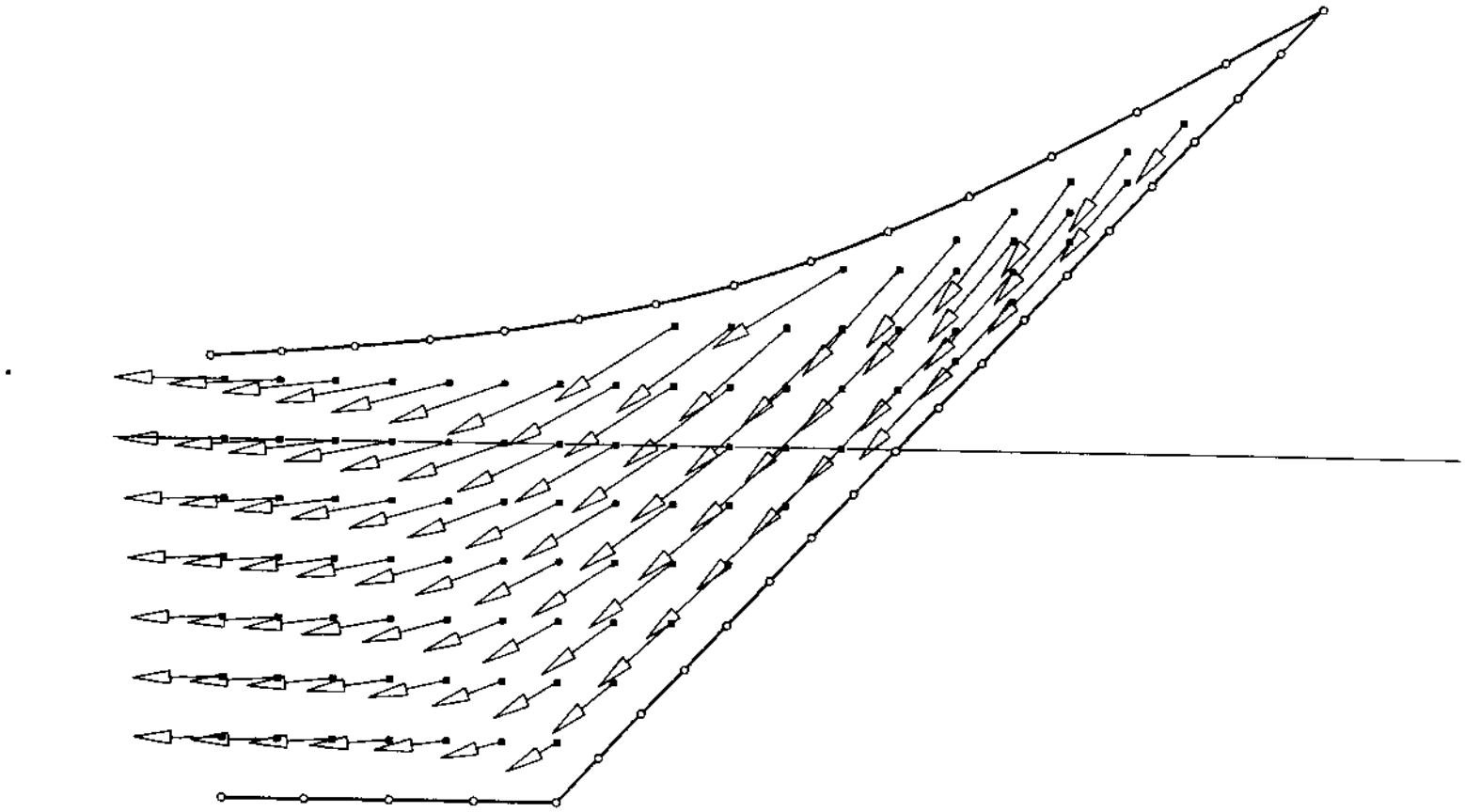

Fig. 17a: Velocity Field, $t' = 36.125$

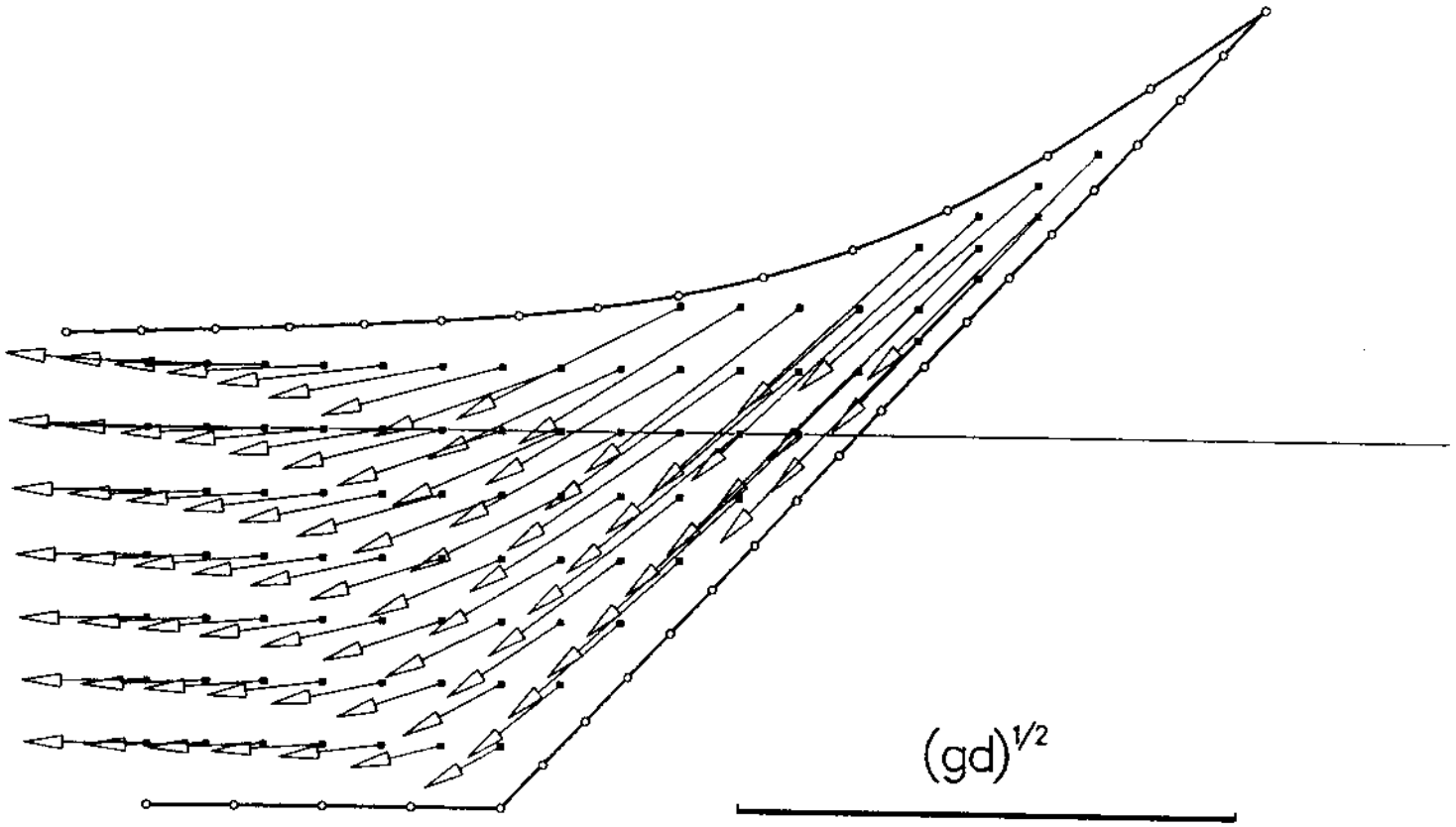

Fig. 17b: Velocity Field, $t' = 37.250$

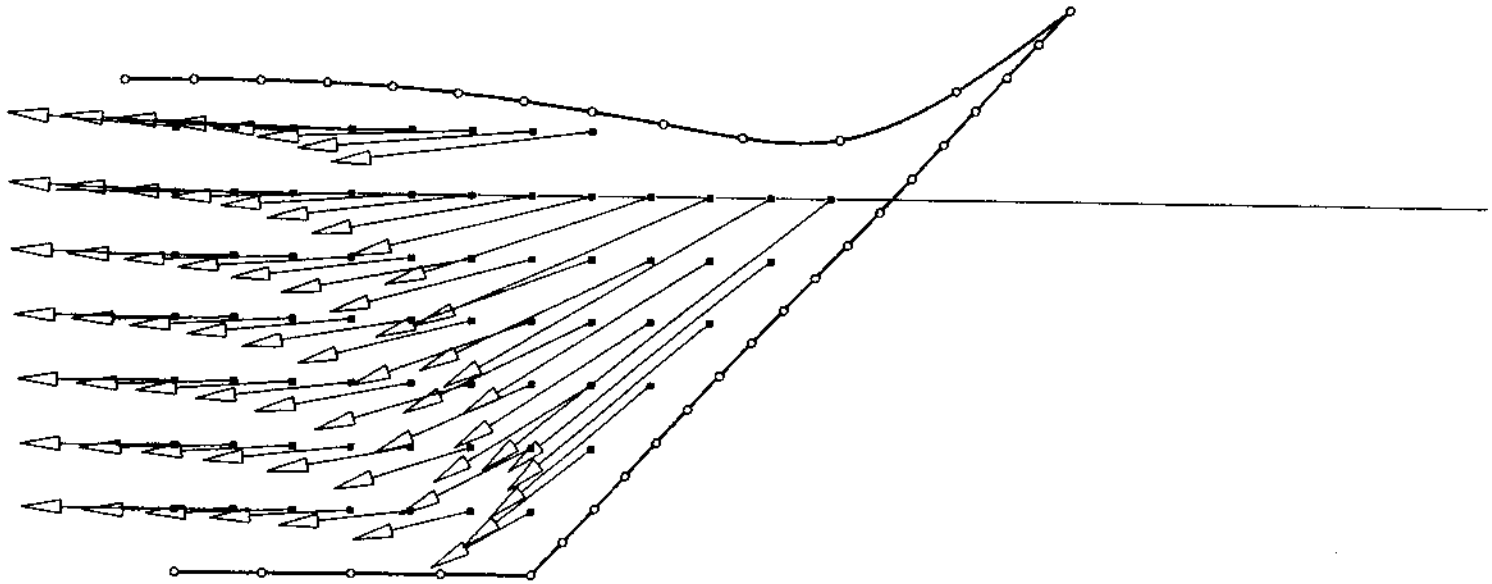

Fig. 17c: Velocity Field, $t' = 37.787$

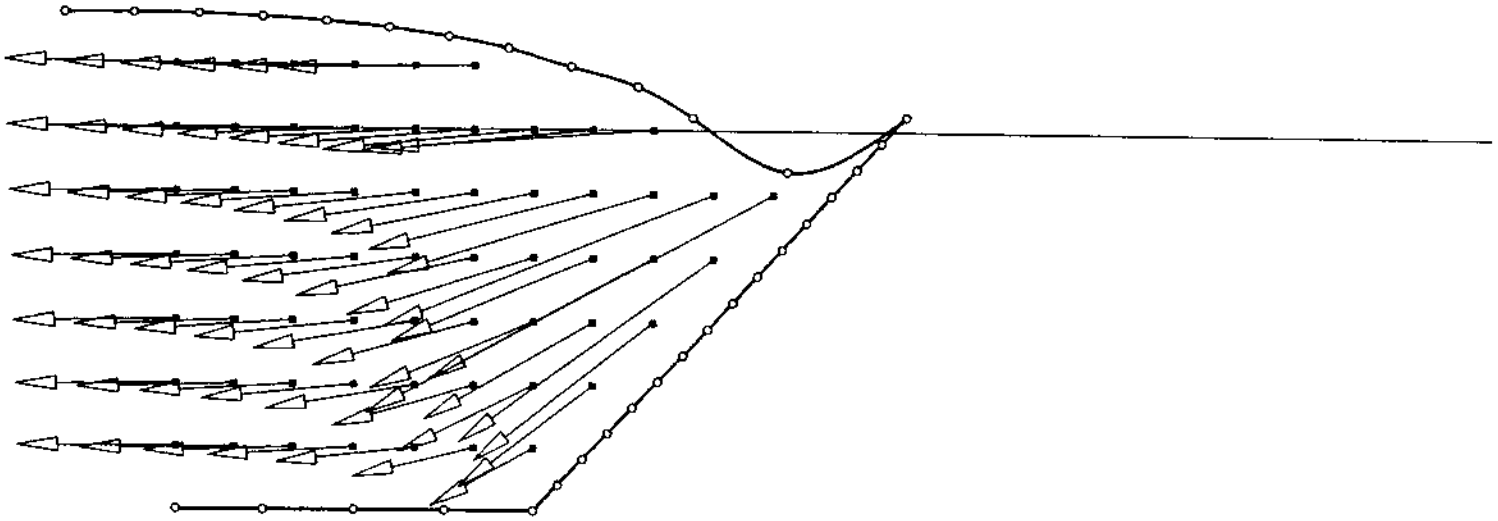

Fig. 17d: Velocity Field, $t' = 37.962$

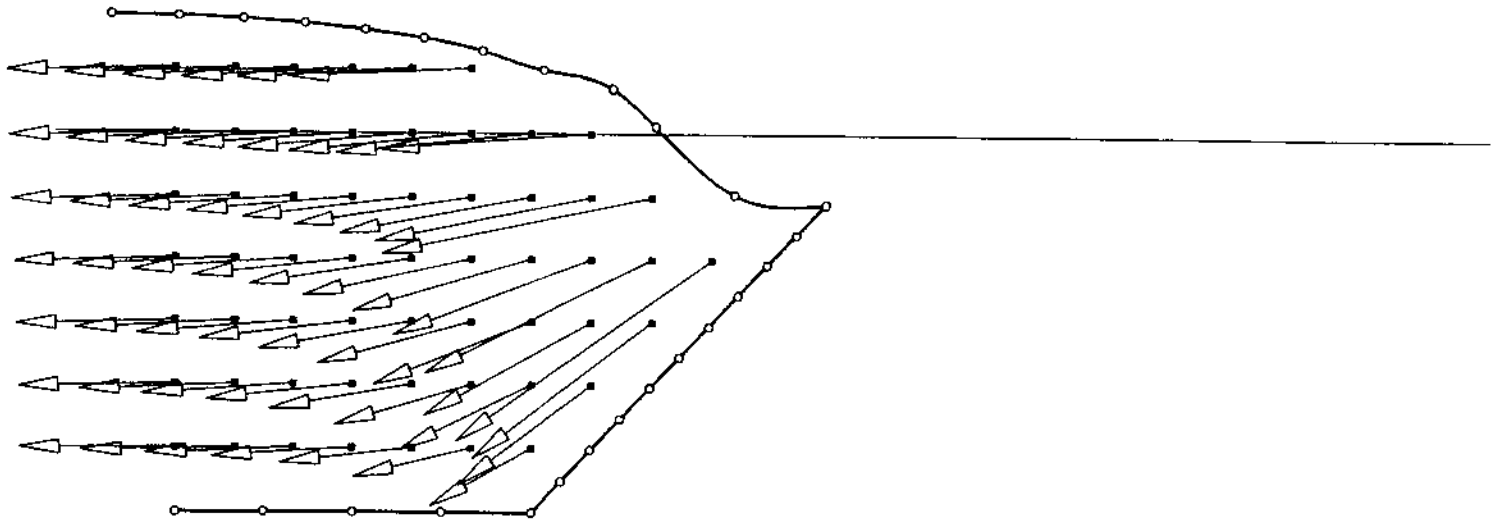

Fig. 18a: Pressure On a 45 Degree Slope

During The Runup, H/d = 0.457

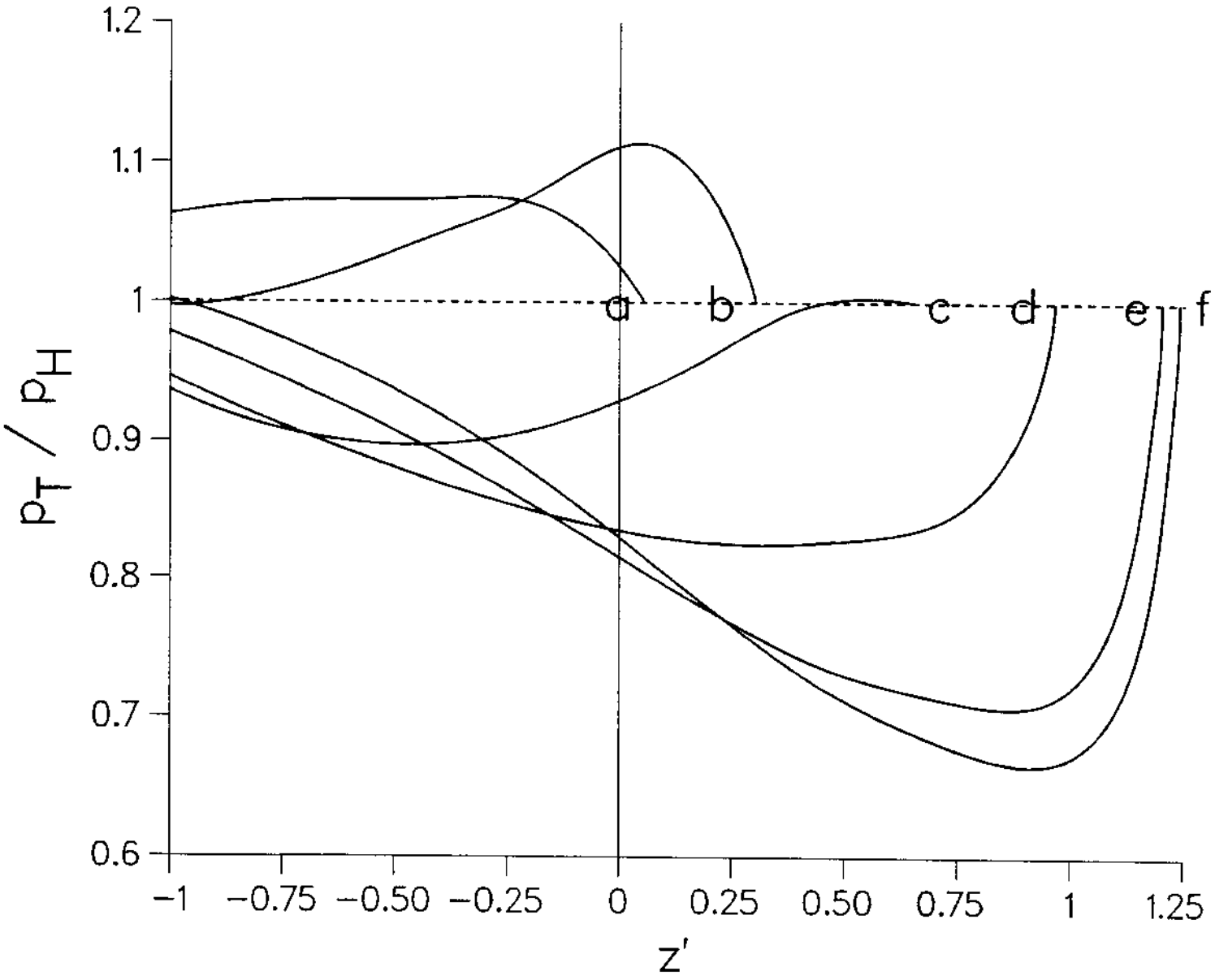

Fig. 18b: Pressure On a 45 Degree Slope

During The Rundown, H/d = 0.457